ON CRUSTAL AND LITHOSPHERIC STRUCTURES OF RIFT BASINS FORMED WITHIN THE TURKANA DEPRESSION IN THE EAST AFRICA AND THE TRANS-SOUTHERN AFRICAN OROGEN IN THE SOUTHWEST AFRICA

By

LUELSEGED M. EMISHAW

Bachelor of Science in Geology
Addis Ababa University
Addis Ababa, Ethiopia
2012

Master of Science in Geology
Oklahoma State University
Stillwater, Oklahoma
2015

Submitted to the Faculty of the
Graduate College of the
Oklahoma State University
in partial fulfillment of
the requirements for
the Degree of
DOCTOR OF PHILOSOPHY
December, 2020

ON CRUSTAL AND LITHOSPHERIC STRUCTURES OF RIFT BASINS FORMED WITHIN THE TURKANA DEPRESSION IN THE EAST AFRICA AND THE TRANS-SOUTHERN AFRICAN OROGEN IN THE SOUTHWEST AFRICA

Dissertation Approved:

Dr. Mohamed Abdelsalam
Dissertation Adviser

Dr. Daniel A. Laó Dávila

Dr. James Knapp

Dr. Hamed Gholizadeh

ACKNOWLEDGEMENTS

I would like to take this opportunity to express my heartfelt gratitude to my committee members. Their kind gesture and guidance made the successful completion of this dissertation possible. I would also like to extend special thanks to my advisor, Dr. Mohamed Abdelsalam. His high level of care and genuine support made my PhD study pleasant and memorable. My sincere appreciation also goes to my academic mentor, Dr. Kevin Mickus, whose invaluable inputs and constructive feedback improved the computational approaches of gravity data presented in the dissertation.

Many thanks to Oklahoma State University -- America's Brightest Orange -- for its best education and financial support. I will always cherish my family in Boone Pickens School of Geology. Special thanks to members of TGIF and Geospatial and Geodynamic Lab for the great intellectual discussions we have had over the years.

Finally, I would like to thank my lovely wife, Cabraile Emishaw, and the rest of my family. They have been a great source of inspiration and optimism. Thank you!

Name: LUELSEGED M. EMISHAW

Date of Degree: DECEMBER, 2020

Title of Study: ON CRUSTAL AND LITHOSPHERIC STRUCTURES OF RIFT BASINS FORMED WITHIN THE TRUKANA DEPRESSION (TD) IN THE EAST AFRICA AND THE TRANS-SOUTHERN AFRICAN OROGEN (TSAO) IN THE SOUTHWEST AFRICA

Major Field: GEOLOGY

Abstract:

This doctoral dissertation examines the crustal and lithospheric structures of rift basins formed within the Turkana Depression (TD) in east Africa and the Trans-Southern African Orogen (TSAO) in southwest Africa. Both regions have undergone complex structural and petrological evolution since the Archean eon and exhibit belts of deformations that resulted from the assembly and fragmentation of both Rodina and Pangaea. Since the Cenozoic, the crust and the sub-continental lithospheric mantle beneath the TD and the TSAO have been significantly weakened and stretched by plume related dynamics triggering the southward and the southwestward propagation of the East African Rift System. The Precambrian suture zones and the Mesozoic rift basins have also influenced these zones of extensional deformations. This doctoral dissertation is designed to explore the spatial extent of these structurally complex tectonic entities and investigate the role of these structures in the nucleation and development of various zones of extensional deformations, particularly rift basins related to the East African Rift System. To this end, geophysical, remote sensing, and numerical methods have been implemented to model the upper crustal-, crustal-, and lithospheric-scale structures beneath the TD and TSAO. For the first time, this doctoral work also introduces improved methods to estimate depth to the Moho and the Precambrian crystalline basement using potential field data. The details are presented in the following chapters summarized as three independent projects.

TABLE OF CONTENTS

Chapter Page

Chapter Page

Chapter Page

CHAPTER IV

Chapter Page

LIST OF FIGURES

Figure Page

Figure Page

CHAPTER I

INTRODUCTORY SUMMARY

Characterizing the nucleation and developmental processes of continental rifts is inseparable from adequately defining the tectonic evolution of the crust within which continental rifts form. This is because the incipient phase of a continental rift basin and its continuous development is largely dependent upon the rheology of the lithosphere upon which it rests. For instance, thermally weakened and thinned lithosphere tends to facilitate continental rifting if and when sufficient deviatoric stress is available to cause crustal deformation. The lithospheric memory – whether or not preexisting structures are preserved within the lithosphere – is also another important factor that controls the nucleation and development of continental rifts. Additionally, magmatism plays a crucial role in rift evolution (e.g. The Afar rift, the Main Ethiopian Rift (MER), and the Turkana rift), even though some rift basins appear to be magma poor (e.g. the Rukwa rift). Thus, investigating the evolution of continental rift basins require a full-scale investigation of the lithosphere upon which they rest. This endeavor is very complex and challenging as continental rifts develop within different geodynamic settings that sustained distinct episodes of deformation. In the case of the EARS, the Southwestern Branch of the EARS mostly developed within orogenic belts that are Paleoproterozoic-Mesoproterozoic in age, while the Eastern Branch of the EARS developed within orogenic belts that are Neoproterozoic in age.

There are also instances, as in the case of the Eyasi basin, where continental rift basins develop on remobilized cratons and/or cratonic margins. Thus, it is misleading to generalize the nucleation and developmental processes of continental rifts from a snapshot of a single rift that is at a certain developmental stage resting on a certain geodynamic setting. This warrants the importance of considering continental rifts of different styles and ages to explore the major factors that contribute to rifting continents.

To this end, the crustal and lithospheric structures of rift basins that formed within the Turkana Depression (TD) in east Africa and the Trans-Southern African Orogen (TSAO) in southwest Africa are examined by using geophysical methods. These geodynamic settings are ideal to study the nucleation and evolution of continental rifts as they have undergone complex structural and petrological evolution since the Archean eon and exhibit belts of deformations that resulted from the assembly and fragmentation of both Rodina and Pangea. Since the Cenozoic, the lithospheric mantle beneath the TD and the TSAO has undergone extension by plume related dynamics triggering the southward and the southwestward propagation of the EARS.

The TD is a NW trending topographic corridor within the East African Rift System between the Ethiopia-Yemen plateau in the northeast and the East African plateau to the southwest. The Anza rift within the TD is a NW-SE trending failed arm of a late Jurassic rift-rift-rift triple junction. This rift is correlated with the Sudan and South Sudan rifts. The Anza rift is intersected by the East African Rift System represented by the N-S trending Turkana rifted zone. The first article of this doctoral dissertation titled "*Development of Late Jurassic-Early Paleogene and Neogene-Quaternary Rifts within the Turkana Depression, East Africa from Satellite Gravity Data*" examines the lithospheric structure beneath the TD using satellite gravity data. Additionally, it examines the crustal density distribution beneath the Kino Sogo fault belt, part of the Turkana rifted zone, to better understand the state of strain accommodation

with increasing depths as the N-S trending structure of the Cenozoic EARS interacts with the NW trending structure associated with the Mesozoic Anza rift basin.

To better understand the tectonic evolution of the EARS as a whole, and continental rifts in general, this doctoral dissertation additionally examined the lithospheric structure beneath the SWB of the EARS. To summarize briefly, the SWB of the EARS consists of NE-SW trending rift basins that rest on the TSAO. The SWB of the EARS is a ~1000 km wide corridor of rift basins extending for ~1700 km from the west side of Tanganyika and the Malawi rifts. The TSAO constitutes from older to younger, the Paleoproterozoic Magondi orogenic belt, the Paleoproterozoic – Mesoproterozoic Kibaran orogenic belt, the Mesoproterozoic – Neoproterozoic Irumide metacraton, and Southern Irumide and Ghani – Chobe orogenic belts, and the Neoproterozoic Zambezi and Damara orogenic belts and the Lufillian arc. These orogenic belts are bounded by two major cratons: 1) the Congo craton, which in this case is defined to constitute the Congo-Tanania-Bangweulu craton, and 2) the Kalahari craton, which, in the same way, is defined to constitute the Zimbabwe-Kaapvaal-Niassa craton. The distribution of these tectonic entities and the prevalence of rift basins of the SWB of the EARS within them allow to investigate the role of preexisting structure in rift initiation and development. Additionally, it gives a proper framework to evaluate the role of composite tectonic terrains of different ages and origin in determining the extent of individual rift basins. The fourth chapter of the dissertation titled "*Lithospheric Structure of the Congo-Tanania-Bangweulu Craton, the Zimbabwe-Kaapvaal-Niassa Craton, and the Trans-Southern African Orogen*" gives a broad overview on the tectonic evolution of the SWB of the EARS and investigate their preferential zones of nucleation by modeling the lithospheric structure beneath them through geophysical modeling of potential field data.

Most of the results presented in this doctoral research is obtained by processing satellite gravity data, particularly, World Gravity Model (WGM-2012) and European Improved Gravity Model of the Earth by New Techniques (EIGEN-6C4). The attributes of these gravity datasets are explained in detail in the second and fourth chapters of this dissertation. However, the third chapter of this dissertation titled

“Spectral Analysis with Piecewise Regression Approach (SAPRA) of Gravity Data for Lithospheric Structure Imaging: The Lake Turkana Rift Basin of the East African Rift System.” examines the non-uniqueness of the potential field data, and introduces a new quantitative analysis to make the 2D-radially averaged spectral method objective with piecewise regression approach. This approach overcomes the subjectivity associated with data points breaks in slope of linear segments of spectrum curve in estimating depth to the Moho and the Precambrian crystalline basement. The development of SAPRA has also been useful in implementing the 2D radially-averaged spectral analysis to estimate depth to the lithosphere-asthenosphere boundary.

CHAPTER II

DEVELOPMENT OF LATE JURASSIC-EARLY PALEOGENE AND NEGOGENE-QUATERNARY RIFTS WITHIN THE TURKANA DEPRESSION, EAST AFRICA

Abstract I

The Turkana Depression (TD) is a NW trending topographic corridor within the East African Rift System between the Ethiopia-Yemen plateau in the northeast and the East African plateau to the southwest. The Anza rift within the TD is a NW-SE trending failed arm of a late Jurassic rift-rift-rift triple junction. This rift is correlated with the Sudan and South Sudan rifts. The Anza rift is intersected by the East African Rift System represented by the N-S trending Turkana rifted zone. We image the lithospheric structure beneath the TD using satellite gravity data. We also use these data to model crustal density distribution beneath the Kino Sogo fault belt, part of the Turkana rifted zone. The results show thinner crust (23–28 km) and lithosphere (140–150 km) beneath the TD. We interpret this as due to extension that resulted in the formation of the Kenya-Sudan and South Sudan rifts. The results also show that crustal depth between 0 and 4.8 km is dominated by N-S density contrast anomalies and between 4.8 and 14.5 km by E-W anomalies. We interpret the N-S anomalies as due to the presence of Precambrian structure that might have facilitated strain localization during the initiation of the Kino Sogo fault belt. Differently, we interpret the E-W anomalies as due to the presence E-W trending faults that were formed in association with the development of the Anza rift and/or Turkana rifted zone and were later filled with Mesozoic and Cenozoic mafic dikes.

2.1 Introduction

Determining the main factors that control strain localization during the onset of continental rifts is challenging because there are many variables that are involved in such localization. However, one handy explanation that has been advanced by the scientific community is that continental rifts follow zones of thin lithosphere largely presented by orogenic belts of different ages extending at the margins of Archean-Paleoproterozoic cratons (e.g., Corti et al., 2013; Daly et al., 1989; Delvaux, 2001; Leseane et al., 2015; Rosendahl et al., 1992; Sarafian et al., 2018). This explanation is based on the observed along-strike coincidence between continental rifts and orogenic belts. In Africa, examples of such along-strike coincidence include the ~20-Ma magma-poor Rukwa rift that occupies the central part of the Western Branch of the Eastern African Rift System (EARS; Figure 1a). This segment of the Eastern Branch follows the trace of the Paleoproterozoic Ubendian orogenic belt, which is bounded in the northeast by the Tanzania craton and to the southwest by the Bangweulu cratonic block (e.g., Delvaux, 2001; Heilman et al., 2019; Lemna et al., 2019; Rosendahl et al., 1992).

Despite the assertion that continental rifts develop within the weaker lithospheric zones of orogenic belts, little is known about how extension is accommodated at depth during different geological times when different episodes of younger continental rifting are superimposed on the older orogenic belts. For example, it is suggested that the 45 Ma–Present Eastern Branch of the EARS (Figure 1a; e.g., Zanettin et al., 1983) follows the Neoproterozoic East African orogen (e.g., Chorowicz, 2005), which developed due to collision between East and West Gondwana (e.g., Abdelsalam & Stern, 1996; Fritz et al., 2013; Stern, 1994). This suggestion assumes that the weaker lithosphere of the East African orogen facilitated the localization of strain that is exerted by the eastward movement of the Somalia plate away from the stationary Nubia plate (Figure 1a; e.g., Stamps et al., 2008; Saria et al., 2014).

Hence, this suggestion predicts the presence of a thinner lithosphere (both the crust and the subcontinental lithospheric mantle (SCLM)) beneath both the East African orogen and the Eastern Branch of the EARS. However, this is not the case since segments of the Eastern Branch such as the southern Main Ethiopian Rift (Figure 1a) are underlain by relatively thick crust (Dugda et al., 2005; Emishaw et al., 2017; Keranen et al., 2009).

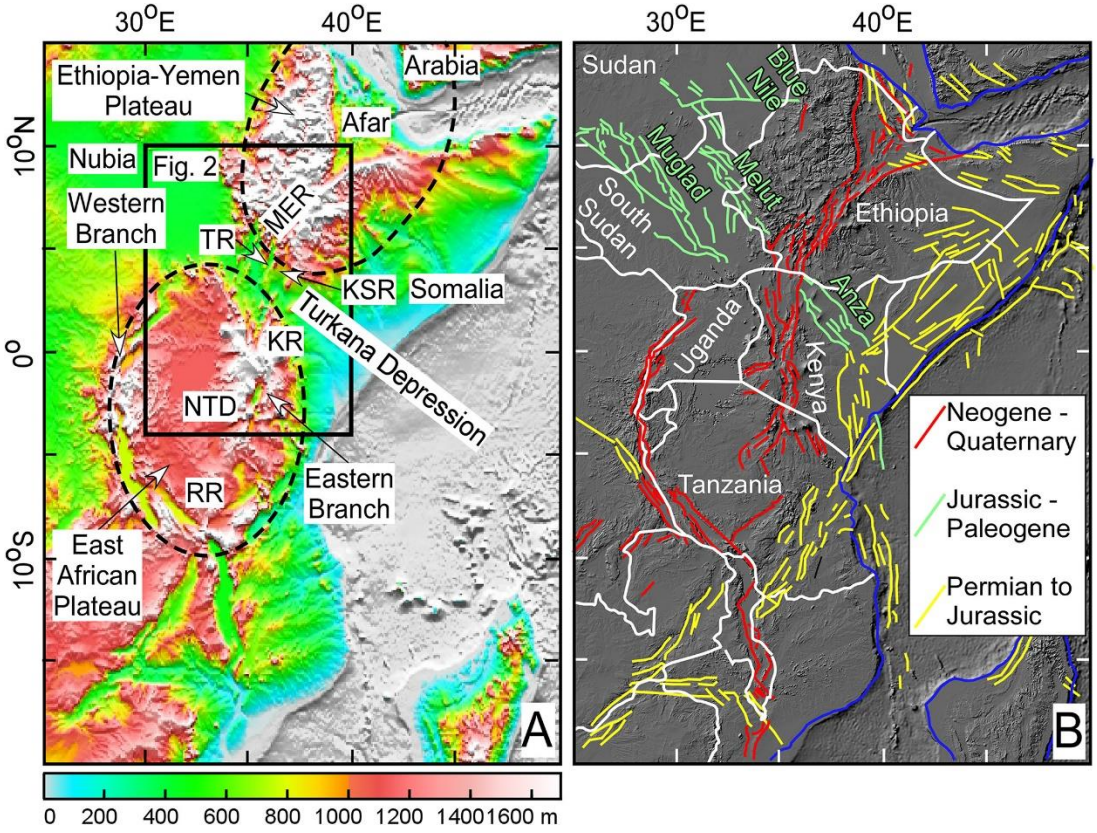

Figure 2.1:(a) Earth topography 1 arc min (ETOPO1) digital elevation model (DEM) showing the East African Rift System (EARS). The DEM shows the low topographic corridor of the Turkana Depression (TD), which separates the Ethiopia-Yemen plateau from the East African plateau. MER = Main Ethiopian Rift, TR = Turkana rifted zone, KSR = Kino Sogo fault belt, KR = Kenya rift, NTD = North Tanzania Divergence, RR = Rukwa rift. (b) Faults in East Africa classified based on the age of their peak activities. The background is an ETOPO1 DEM. The map shows that the faults of the Jurassic-Paleogene Kenya-Sudan Rifts (KSR) are intersected at high angle by the faults of the Neogene-Quaternary EARS within the TD. Modified after Macgregor (2018).

In East Africa, most of the late Jurassic-early Paleogene continental rifts are NW-SE trending while the Neogene-Quaternary continental rifts are dominantly N-S to NE-SW trending (Figure 1b).

The NW SE trending late Jurassic-early Paleogene rifts are represented by those in northern Kenya (Figures 2a and 2b; Bosworth & Morley, 1994; Dindi, 1994; Reeves, et al., 1987) and in Sudan and South Sudan (Figures 2a, 2c, and 2d; Bosworth, 1992; Dou et al., 2007; Fairhead, 1988; Mann, 1989; McHargue et al., 1992; Schull, 1988). These rifts will be referred to here as the Kenya-Sudan Rifts (KSR). The N-S to NE-SW trending Neogene-Quaternary rifts are represented by segments of the Eastern Branch of the EARS including the Turkana rifted zone (Figure 1a; e.g., Bonini et al., 2005; Brune et al., 2017; Corti et al., 2019; Dunkelman et al., 1989; Ebinger et al., 2000; Emishaw et al., 2017; Morley, Wescott, et al., 1999; Rosendahl et al., 1992; Vetel et al., 2005; Vetel & Le Gall, 2006).

The Eastern Branch of the EARS intersects the KSR at highly oblique angle within the Turkana Depression (TD; Figures 1a and 1b). This anomalously low NW-SE elongated, ~500-km-wide topographic corridor occurs between the elevated Ethiopia-Yemen plateau in the northeast and the East Africa plateau to the southwest (Figure 2a). These plateaus represent part of the African Superswell, which was caused by the African Superplume (Nyblade & Robinson, 1994). One explanation given to the development of the TD is that the superimposition of the rifting events associated with the KSR and the EARS resulted in significant thinning of the crust leading to lowering of the elevation through isostatic adjustment (Benoit et al., 2006). Crustal thinning beneath the TD is documented from controlled source seismic imaging (Keller et al., 1994; Mechie et al., 1994; Prodehl et al., 1994) and Rayleigh wave dispersion modeling (Benoit et al., 2006).

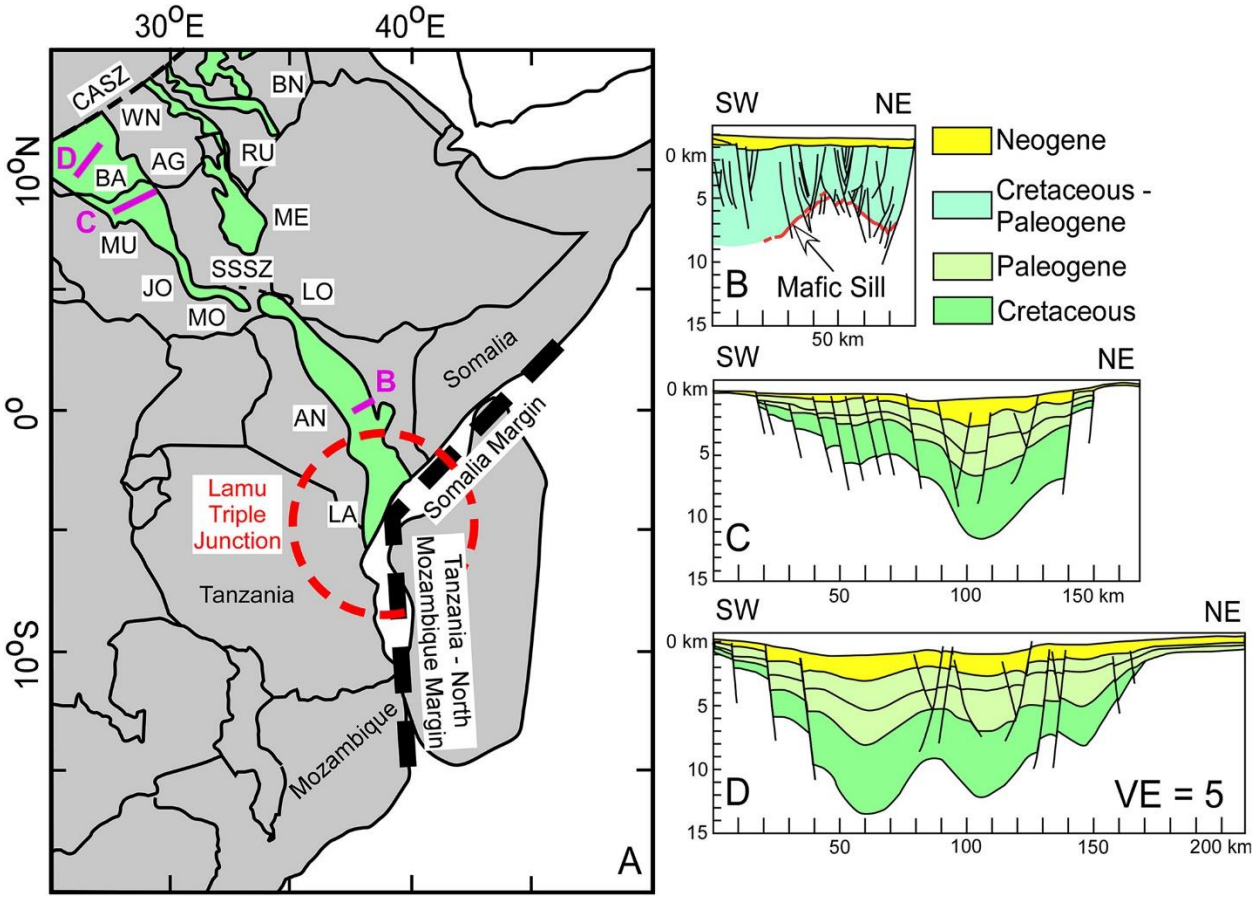

Figure 2.2: (a) Simplified map showing the rift basins of the Kenya-Sudan-Rifts (KSR) and their possible evolution as a failed rift arm of the Lamu rift-rift-rift triple junction. The extent of the KSR sedimentary basins is modified from Bosworth (1992) and Dou et al. (2007). CASZ = Central Africa shear zone, BA = Bahr el Arab rift, AG = Abu Gabra rift, MU = Muglad rift, JO = Jonglei rift, MO = Mongala rift, WN = White Nile rift, RU = Ruat rift, ME = Melut rift, BN = Blue Nile rift, SSSZ = South Sudan shear zone, LO = Loelli rift, AN = Anza rift, LA = Lamu rift. The pink lines labeled B, C, and D show the location of the cross sections in Figures 2b–2d. (b) Geological section across portion of the central part of the Anza rift. Modified from Bosworth and Morley (1994). The depth of the section is estimated from the relationship between the two-way travel time and depth reported by Bosworth and Morley (1994) to be 4.5 s = 7 km. (c and d) Geological sections across portions of the Bahr el Arab and Muglad rifts. Modified from Schull (1988).

The intersection of the KSR and the EARS within the TD provides a unique site for examining the controls of the mechanical and thermal lithospheric heterogeneities in the development of continental rifts. This is because the TD stretches at the interface between the Arabian-Nubian Shield with prominent N-S trending Precambrian structure in northeast and the Saharan Metacraton to

the southwest (Figures 3a and 3b). It is also because where it has been suggested that the inherited crustal structure from the KSR resulted in the development of the Turkana rifted zone as an anomalously wide (~300 km) segment within the Eastern Branch of the EARS and that this inherited crustal structure have contributed to shaping the final geometry of the Turkana rifted zone (Bonini et al., 2005; Brune et al., 2017; Corti et al., 2019; Ebinger et al., 2000; Vetel et al., 2005; Vetel & Le Gall, 2006). Further, it is because it has been suggested that the thermal effect of an impinging mantle plume head beneath the lithosphere of the Kenya rift resulted in its formation as a narrow rift, whereas the presence of a colder lithosphere beneath the Turkana rifted zone resulted in its development as a wide rift (Koptev et al., 2018).

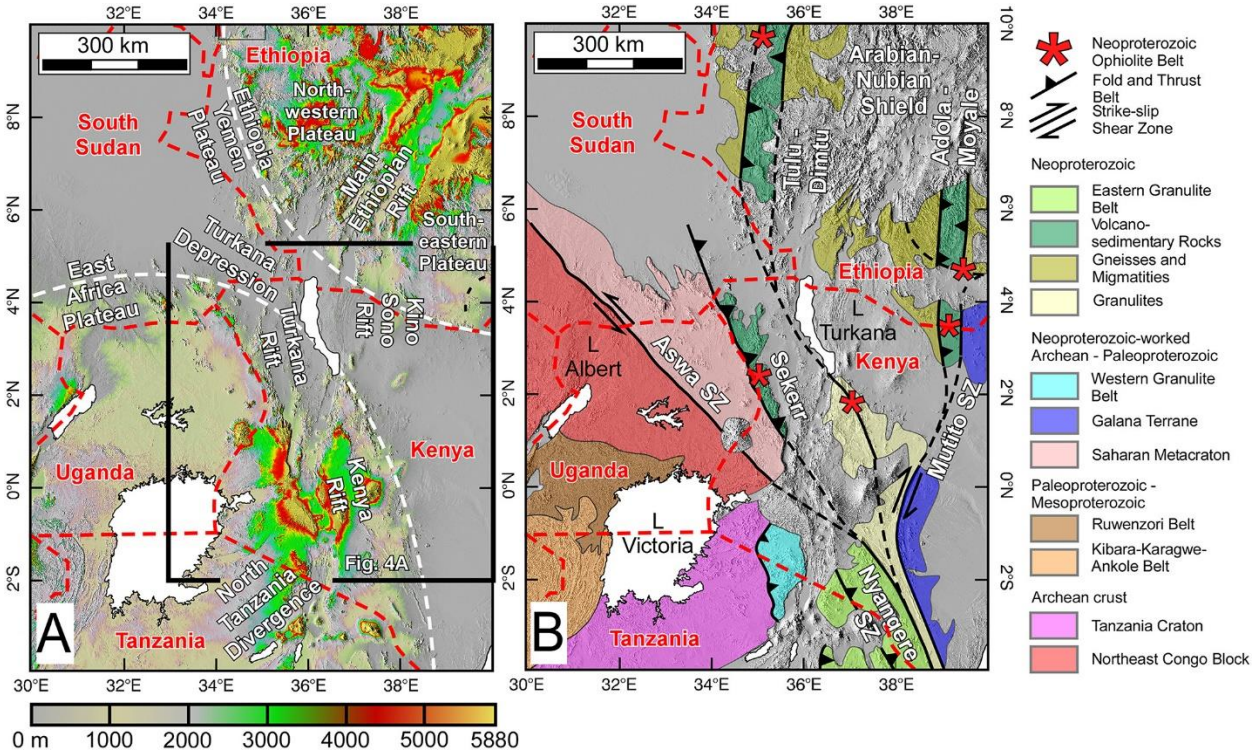

Figure 2.3: (a) Shuttle Radar Topography Mission (SRTM) digital elevation model (DEM) showing the Turkana Depression (TD) between the Ethiopia-Yemen plateau and the East Africa plateau. (b) Exposures of major Precambrian blocks and structure within the TD and the surrounding Ethiopia-Yemen plateau and the East Africa plateau draped onto SRTM DEM. Modified from Fritz et al. (2013).

In this work, I aim to contribute to the understanding of the pattern of strain accommodation as a function of depth and geological time between the KSR and the EARS within the TD (Figures 1a and 2a). I also aim at examining possible controls of the preexisting lithospheric structure on the evolution of the two rift systems. I first image crustal thickness variation beneath the depression and its surroundings by using two-dimensional (2-D) inversion of the European Improved Gravity Model of the Earth by New Techniques (EIGEN-6C4) satellite gravity data. I also image crustal and lithospheric thickness variation beneath the TD and its surroundings using 2-D forward gravity modeling of the satellite gravity data. Subsequently, I apply three-dimensional (3-D) upper crustal inversion for the residual gravity data of the EIGEN-6C4 to a segment of the Turkana rifted zone to better understand how strain was accommodated as a function of depth within the upper crust. Considering the fact that the late Jurassic-early Paleogene rifts in Sudan and South Sudan are petroliferous basins, I believe that the findings will contribute to the hydrocarbon exploration in Kenya.

2.2 Geologic Setting

2.3 The Precambrian Crystalline Basement

The Precambrian crystalline basement rocks within and around the TD belong to Archean-Paleoproterozoic crust, Paleoproterozoic-Mesoproterozoic crust, Archean-Paleoproterozoic crust that was reworked during the Neoproterozoic, and Neoproterozoic crust (Figures 3a and 3b; e.g., Fritz et al., 2013).

The majority of the East Africa plateau is dominated by Archean-Paleoproterozoic and Paleoproterozoic-Mesoproterozoic crust. This is represented by the North Congo block (representing the northeastern part of the Congo craton) and the Tanzania craton, as well as the Kibara-Karagwe-

Ankole and the Ruwenzori orogenic belts (Figure 3b). However, the northeastern side of the East Africa plateau is dominated by the Saharan Metacraton, which is suggested to be an Archean-Paleoproterozoic craton that was reworked during the Neoproterozoic (Figure 3b; Abdelsalam et al., 2002, 2011). In addition, the Western Granulite belt, which is interpreted by Fritz et al. (2013) as an Archean-Paleoproterozoic crust that was reworked during the Neoproterozoic, is exposed on the eastern edge of the Tanzania craton, close to the eastern margin of the East African plateau (Figures 3a and 3b).

The northeastern edge of the East African plateau and the southwestern part of the TD are dominated by outcrops of the Neoproterozoic East African orogen. This orogen comprises the Arabian-Nubian Shield in the north, and the Mozambique orogenic belt to the south (Figure 3b; e.g., Abdelsalam & Stern, 1996; Fritz et al., 2013; Stern, 1994). For example, the Sekerr fold and thrust belt in northwestern Kenya is exposed in the northeastern edge of the East Africa plateau. Abdelsalam and Dawoud (1991) suggested that the Sekerr fold and thrust belt represents the Neoproterozoic suture zone between the Arabian-Nubian Shield in the northeast and the Nile craton to the southwest (now the Saharan Metacraton).

The exposures of the Arabian-Nubian Shield within the southwestern part of the Ethiopia-Yemen plateau are represented by the Adola-Moyale belt in the east and the Tulu Dimtu belt to the west (Figure 3b; e.g., Abdelsalam & Stern, 1996; Fritz et al., 2013). Both belts are characterized by interleaving of zones of late Neoproterozoic-early Cambrian low-grade volcano-sedimentary rocks (sometimes with ophiolite fragments) and gneissic and migmatitic rocks (Figure 3b; e.g., Abdelsalam & Stern, 1996; Fritz et al., 2013). These belts are separated by north trending deformation zones, the kinematics of which received different interpretation (Abdelsalam et al., 2008; Tolessa et al., 1991; Tsige & Abdelsalam, 2005; Worku & Schandelmeier, 1996; Worku & Yifa, 1992).

2.4 The Late Jurassic-Early Paleogene Rift System of East Africa

2.4.1 General Description

Africa had witnessed major rifting events during the late Jurassic-early Paleogene and this resulted in the development of a number of rift systems in the continent (e.g., Binks & Fairhead, 1992; Bosworth, 1992; Genik, 1992, 1993; Guiraud et al., 2005; Maurin & Guiraud, 1993). These include (1) the West African Rift System, (2) the Central African Rift System, and (3) the late Jurassic-early Paleogene rift basins of East Africa found in Kenya, Sudan, and South Sudan. These basins have been considered as parts of the Central African Rift System (e.g., Browne et al., 1985; Browne & Fairhead, 1983; Fairhead, 1988). Here I prefer to separate these basins from those of the Central African Rift System because they are located in East Africa and because, for the large part, they did not develop as transtensional basins as those of the Central African Rift System. In addition, so as not to confuse this rift system with the EARS, as stated earlier, I will refer to this late Jurassic-early Paleogene rift system as KSR in reference to Kenya-Sudan Rifts.

In Kenya, and southeastern South Sudan, the major basin of KSR is the Lamu-Anza-Loelli (Henceforth Anza; Figure 2a; Bosworth, 1992; Bosworth & Morley, 1994; Dindi, 1994; Greene et al., 1991; Morley, Wescott, et al., 1999; Reeves et al., 1987; Winn et al., 1993). In Sudan and South Sudan, the KSR basins include the Abu Gabra-Bahr el Arab-Muglad-Jonglei-Mongala (henceforth Muglad), the White Nile-Ruat-Melut (henceforth Melut) and the Blue Nile (Figure 2a; Bosworth, 1992; Fairhead, 1988; Mann, 1989; McHargue et al., 1992; Schull, 1988). These basins terminate against the Central Africa shear zone (Figure 2a) because of difference in lithospheric

structure of the Precambrian blocks to the north and south of the shear zone (Binks & Fairhead, 1992). Here I focus on the Anza and Muglad rifts because of their likely connection within the TD.

2.4.2 The Anza Rift

Using gravity data, Reeves et al. (1987) were first to identify the Anza rift in the central part of Kenya, which remained unrecognized before because it lacks significant surface expression. Morley, Day, et al. (1999) described the Anza rift as an ~500-km-long, 130-km-wide NW-SE trending Cretaceous-Paleogene graben. Bosworth (1992) and Greene et al. (1991) suggested dividing the Anza rift into a northwestern and a southeastern segment with the northwestern segment extending from the northern tip of Lake Turkana in the northwest (Figure 3a) to the central part of the rift. Using the interpretation of gravity data, Morley, Day, et al. (1999) suggested that the width of the Anza rift decreases toward the northwest until the rift disappears completely just east of the northern tip of Lake Turkana (Figure 3a). Previously, from 2-D forward gravity modeling, Dindi (1994) suggested that the crust beneath the southeastern segment of the Anza rift thins from ~40 km away from the rift to ~35 km beneath the rift axis. In addition, Dindi (1994) proposed from the 2-D forward gravity modeling that the southeastern segment of the rift is filled with ~8 km of sediments. However, the same author used 2-D forward modeling of aeromagnetic data to propose that the Anza rift is filled with ~10 km of sediments.

It has been proposed that the Anza rift is a failed arm of the Jurassic rift-rift-rift triple junction that was formed in association with the breakup of Gondwana (e.g., Bosworth, 1992; Bosworth & Morley, 1994; Greene et al., 1991; Winn et al., 1993). The two successful rifts along the Somali and Tanzania-North Mozambique margins resulted in the separation of Madagascar from Africa (Figure 2a; e.g., Greene et al., 1991; Reeves et al., 1987). The first arm of the paleo-triple

junction was initiated along the Tanzania-North Mozambique margin within which late Carboniferous Karoo sediments were deposited (e.g., Greene et al., 1991). This was followed by the development of the second arm along the Somalia margin during the early to middle Jurassic to initiate seafloor spreading. It has also been suggested that the NW-SE trending structure of the Anza rift was caused by NE-SW regional extension that might have commenced in the late Jurassic (e.g., Bosworth & Morley, 1994).

Bosworth and Morley (1994) suggested that the Anza rift was a site of widespread rifting during the middle to late Cretaceous and that rifting might have continued until early Paleogene. From active source seismic and borehole data, Bosworth and Morley (1994) showed that the Anza rift was receiving clastic sediments during the Cretaceous (Figure 2b) and that this classic sedimentary environment was interrupted by a marine incursion that occurred during the middle Cretaceous. Further, these authors showed that rifting in the Anza rift continued during the Paleogene and this resulted in the deposition of up to 3,000-m-thick fluvial and lacustrine sediments (Figure 3b). Finally, they showed from the same controlled source seismic and borehole data that the top stratigraphic part of the Anza rift is dominated by Neogene sediments (Figure 2b). Morley, Day, et al. (1999) added that different rift-forming episodes might have resulted in significant change in the geometry of the Anza rift and that there seems to be migration of rift activities with time from northwest to southeast. They further suggested adding a phase of Paleogene sag subsidence that followed the development of extensional faults in the Anza rift.

2.4.3 The Muglad Rift

Using aeromagnetic, gravity, and controlled source seismic data, Schull (1988) described the Muglad rift as extending for ~1,000 km in a NW-SE direction in southern Sudan and northern South Sudan (Figure 2a). The basin reaches a width of ~200 km in the northwest, but it becomes narrower

toward the southeast (Figure 2a). Borehole data together with controlled source seismic data allowed Schull (1988) to estimate that the basin is filled with nonmarine clastic sediments that reaches a maximum thickness of ~13.5 km (Figures 2c and 2d).

From palynomorphic analysis, this author documented the lower part of the rift to be dominated by Cretaceous sediments (Aptian, Albian, Cenomanian, Turonian, and Santonian), its central part to be dominated by Paleogene sediments (Paleocene, Eocene, and Oligocene), and its upper part to be dominated by Neogene sediments (Miocene; Figures 2c and 2d). Further, Schull (1988) proposed that the Muglad basin developed through three distinct phases of rifting followed by an intracratonic sag phase. The early phase of rifting spanned the time between early Cretaceous and Albian, the second phase occurred during the Turonian and Senonian, whereas the third phase of rifting occurred during the late Eocene and Oligocene. This author concluded that the intracratonic sag phase of the Muglad basin occurred during the middle Miocene and this phase is characterized by slow rate of subsidence that was not controlled by the development of normal faults.

2.4.4 Connection of the Anza and Muglad Rifts

The existence of pre-Neogene sediments and tectonic activities within the TD around the Turkana rifted zone was first considered on the basis of the presence of immature arkosic sediments found primarily west of Lake Turkana and these sediments are commonly referred to as the Turkana Grits (e.g., Morley et al., 1992; Murray-Hughes, 1933; Williamson & Savage, 1986). Williamson and Savage (1986) summarized that Murray-Hughes (1933) considered the Turkana Grits to be derived from the underlying Precambrian crystalline basement rocks and described them as Jurassic age "pebbly conglomerates, feldspathic grits, and shales." In addition, they reported that Baker et al. (1972) considered the Turkana Grits to be of Neogene age based on the possibility that they were derived from Precambrian crystalline basement rocks that were uplifted during the onset of the

Turkana rifted zone. Further, they mentioned that earlier Arambourg (1943) raised the possibility that the Turkana Grits contain both Mesozoic sediments at their base and Cenozoic sediments at the top. From their own study, Williamson and Savage (1986) concluded that the Turkana Grits are made up of early Cretaceous (Cenomanian)-Paleogene sediments and late Neogene (middle Miocene) sediments. In addition, they proposed that the Cretaceous-Paleogene sediments of the Turkana Grits were deposited within a late Mesozoic rift that was subsequently deformed by major E-W trending dextral strike-slip faults. However, Vetel and Le Gall (2006) carried out fault plane analysis on an outcrop of the Turkana Grits west of Lake Turkana and established a NE-SW exerted extension suggestive of a Cretaceous paleostress similar to that resulted in the opening of the Anza rift farther east as has been reported by Morley, Day, et al. (1999).

A number of regional tectonic maps have shown the Anza rift extending to the west of Lake Turkana rift basin with possible connection to the Muglad rift (e.g., Bosworth, 1992; Dou et al., 2007; Fairhead, 1988). For example, Bosworth (1992) suggested that the northwestern tip of the Anza rift (represented by the Loelli basin) and the southeastern tip of the Muglad rift (represented by the Mangala basin) are connected by the E-W trending South Sudan dextral strike-slip shear zone (Figure 2a). Further, this author suggested that the Mangala segment represents an E-W trending transtensional basin.

Hendrie et al. (1994) calculated the total amount of extension for the southern part of the Turkana rifted zone to be between 35 and 40 km. Subsequently, they pointed to that this amount of extension is much higher than the ~25-km crustal extension estimated for the southern Main Ethiopian Rift and the ~10-km crustal extension estimated for the central Kenya rift. Hence, they concluded that the region currently occupied by the Turkana rifted zone within the TD must have experienced significant amount of crustal extension before the Neogene. They used this to advance

the possibility of the presence of significant amount of pre-Neogene sediments beneath the volcanics associated with the Turkana rifted zone.

Regardless, Vetel and Le Gall (2006) questioned the validity of proposing a connection between what they referred to as the "Turkana Cretaceous basins" and the Muglad rift and concluded that the Anza rift does not extend further northwest to reach the northern part of Lake Turkana. They based their argument on that the isobath lines drawn for the contact between the Precambrian crystalline basement rocks and the overlying Cretaceous sediments for the Anza rift show steep gradient at the northwestern side of the rift. Vetel and Le Gall (2006) used this to suggest the presence of a N-S syn-rift fault that limits the Anza rift in the northwest. Additionally, based on the absence of Cretaceous-Paleogene sediments between the Precambrian crystalline basement rocks and the Paleogene (Oligocene)-Neogene (Pliocene) volcanics, they proposed that the Anza rift does not extend northwest further than the eastern side of the Kino Sogo fault belt (Figure 5a).

2.5 The Neogene-Quaternary EARS

Only the Eastern Branch of the EARS is relevant to this study. This branch extends from the Afar Depression in Eritrea, Djibouti and Ethiopia through the Main Ethiopian Rift, the Turkana rifted zone within the TD in southern Ethiopia, and northern Kenya, the Kenya rift, to the North Tanzania Divergence (Figure 1a). The Afar Depression and the Main Ethiopian Rift dissect the Ethiopia-Yemen plateau, whereas the Kenya rift and the North Tanzania Divergence stretch along the eastern edge of the East Africa plateau (Figure 1a).

The Ethiopia-Yemen and the East African plateaus bound the TD in the northeast and southwest, respectively (Figures 1a and 2a). Within the TD, the ~300-km-wide Turkana rifted zone include, from west to east, the North Lockichar rift basin, the Turkwell rift basin, the Kerio rift basin, the Lake Turkana rift basin, and the Kino Sogo fault belt (Figures 4a, 4b, 5a, and 5b; Dunkelman et

al., 1989; Rosendahl et al., 1992; Morley, Day, et al., 1999; Ebinger et al., 2000; Bonini et al., 2005; Vetel et al., 2005; Vetel & Le Gall, 2006; Brune et al., 2017; Corti et al., 2019).

Ebinger et al. (2000), Bonini et al. (2005), and Vetel and Le Gall (2006) considered the Lake Turkana rift basin to be the northward propagation of the Kenya rift and the poorly known Ririba rift east of the Kino Sogo fault belt (Figure 4a) to be the southward propagation of the Main Ethiopian Rift within the TD.

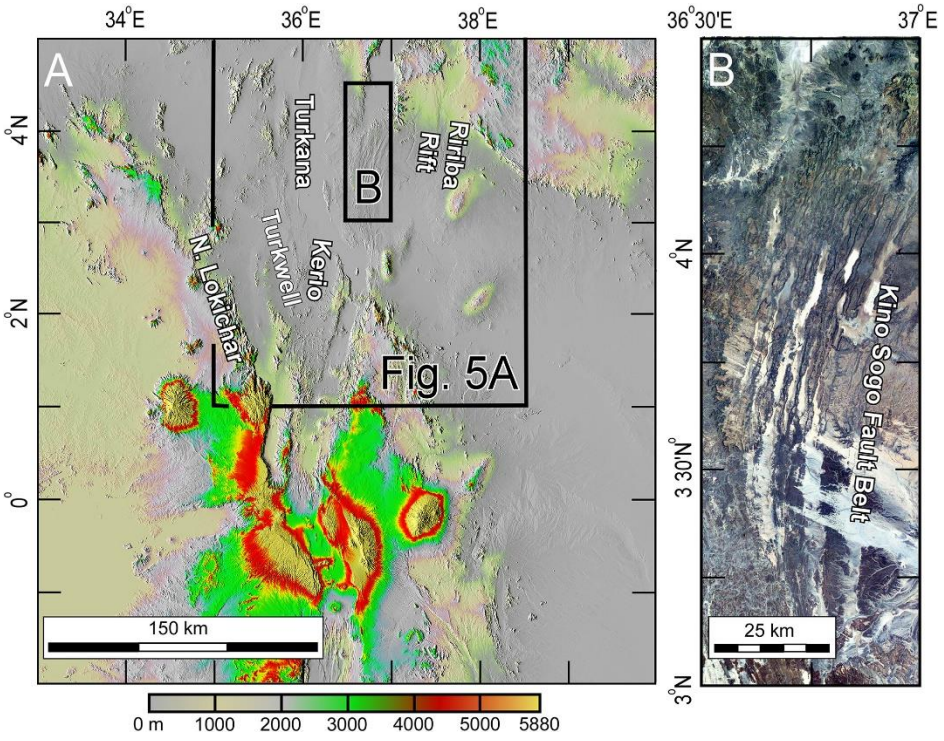

Figure 2.4: (a) Shuttle Radar Topography Mission (SRTM) digital elevation model (DEM) showing the Turkana Depression (TD) and individual segments of the Turkana rifted zone. (b) The 3-2-1 Landsat Thematic Mapper (TM) image of the Kino Sogo fault belt. The image is obtained from Google Earth Pro.

The TD around the Turkana rifted zone is floored with outcrops of Precambrian crystalline basement rocks, Mesozoic and Cenozoic sediments, and Cenozoic volcanics (Figure 5a; e.g., Morley, Wescott, et al., 1999; Vetel & Le Gall, 2006). Controlled source seismic and borehole data showed

that different segments of the Turkana rifted zone are filled with Paleogene-Neogene, Neogene, and Neogene-Quaternary sediments (Figure 5b; e.g., Morley, Wescott, et al., 1999; Vetel & Le Gall, 2006). Further, Vetel and Le Gall (2006) suggested that the Turkana rifted zone evolved through five volcanic-tectonic events that occurred during the periods 45–23, 23–15, 15–6, 6–2.6, and 2.6 Ma–Present.

Morley, Wescott, et al. (1999) described the North Lokichar rift basin as a half graben, which is bounded by a border fault on its western side (Figures 4a, 5a, and 5b). This fault has well-defined morphological expression (Figure 4a) as well as it can be traced to a depth of ~10 km as observed from controlled source seismic imaging (Figure 5b; Morley, Wescott, et al., 1999). However, unlike the Lokichar rift basin, the border faults of the Turkwell and Kerio rift basins do not have well-defined morphological expression (Figure 4a). However, results from controlled source seismic data suggested the presence of border faults on the western side of these rift basins (Figure 5b; Morley, Wescott, et al., 1999; Vetel & Le Gall, 2006).

From controlled source seismic data, Dunkelman et al. (1989) described the Lake Turkana rift basin to be formed from a series of north trending half grabens with alternating border faults on their eastern and western sides. Further, they suggested that these half grabens become progressively deeper toward the northern part of the Lake Turkana rift basin reaching a depth of up to ~4 km. Further, from controlled source seismic data collected along N-S profile (Figure 6a) by the Kenya Rift International Seismic Project (KRISP) Working Group (1991) (Figure 6a), Keller et al. (1994), Mechie et al. (1994), and Prodehl et al. (1994) have shown that the crust beneath the central part of the Lake Turkana rift basin thins to ~20 km.

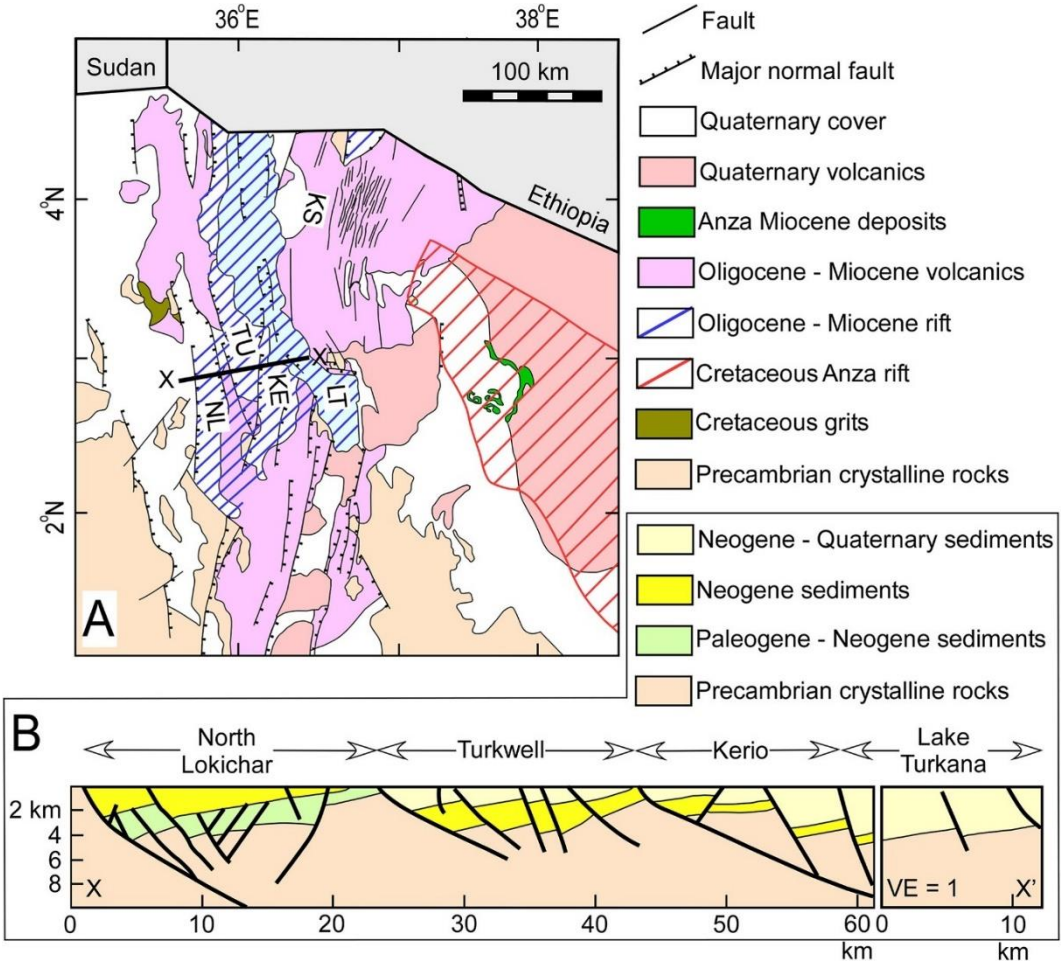

Figure 2.5: (a) Geological map of portion of the Turkana Depression (TD) showing the exposed rock formations, segments of the Turkana rifted zone, and proposed subsurface extension of the Anza rift. NL = North Lokichar rift basin, TU = Turkwell rift basin, KE = Kerio rift basin, LT = Lake Turkana rift basin, KS = Kino Sogo fault belt. (b) E-W geological section across segments of the Turkana rifted zone based on controlled source seismic and borehole data. See Figure 5a for the location of the cross section. Modified from Morley, Wescott, et al. (1999) and Vetel and Le Gall (2006).

This thin crust becomes progressively thicker toward the south until reaching ~35-km thickness in the northern part of the East Africa plateau. From restoration of a controlled source seismic section across the southern part of the Turkana rifted zone including the southern part of the Lake Turkana rift basin, Hendrie et al. (1994) estimated the total extension to be between 35 and 40 km. In addition, they used this extension to estimate a stretching factor ranging between 1.55 and 1.65. Further, they pointed that their estimated total extension and stretching factor across the Turkana rifted zone are in good

agreement with the crustal thinning reported by Keller et al. (1994), Mechie et al. (1994), and Prodehl et al. (1994).

The Kino Sogo fault belt has an unusual geometry compared to other segments of the Turkana rifted zone. It is an ~40-km-wide zone of extension dominated by alternation of 1- to 2-km-wide horsts and grabens, which dissect Cenozoic lava flows (Figures 4a, 4b, and 5a; e.g., Vetel et al., 2005). These authors explained the presence of the anomalously narrow grabens constituting the Kino Sogo fault belt as due to the reactivation of penetrative preexisting Precambrian fabric or strain localization within intense fracture system that was formed as the result of the extrusion and crystallization of the Cenozoic lava flows.

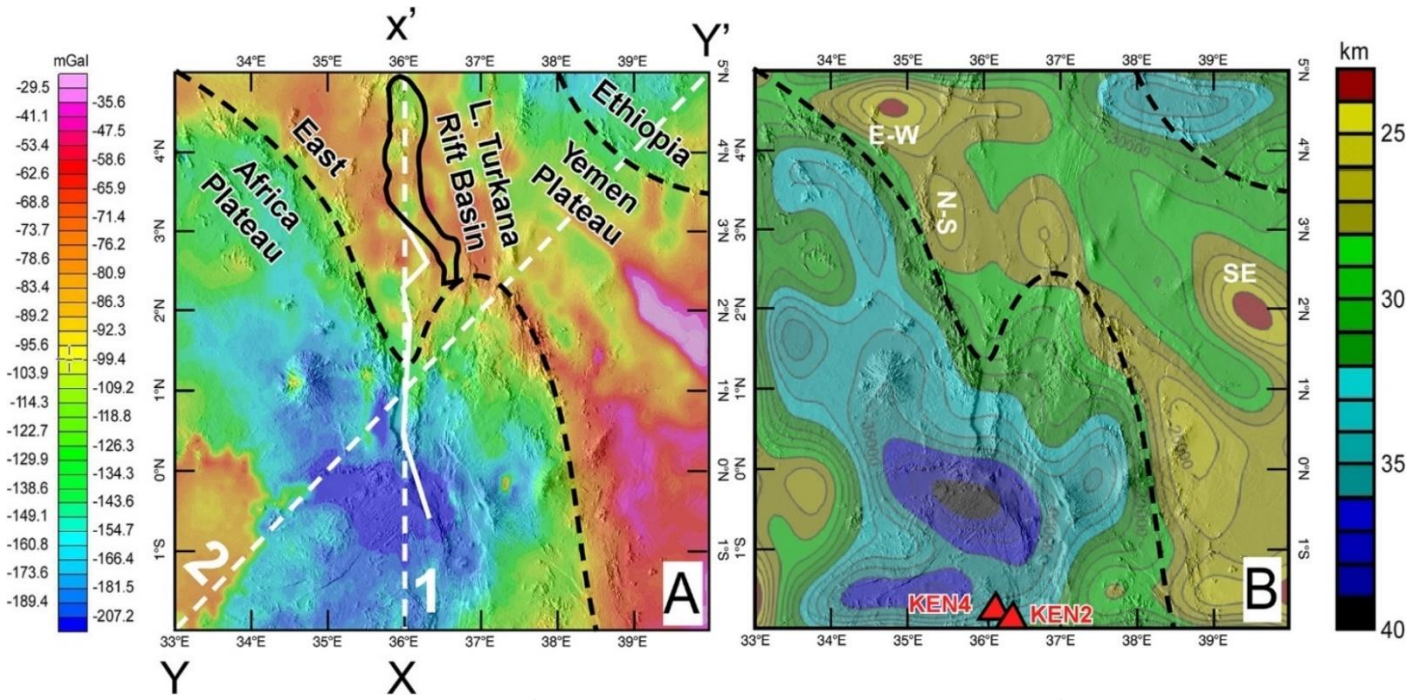

Figure 2.6: (a) Bouguer gravity anomaly map of the Turkana Depression (TD) and its surroundings obtained from the European Improved Gravity Model of the Earth by New Techniques (EIGEN-6C4). The solid white line shows that trace of the controlled source seismic data of Keller et al. (1994). The dashed white lines labeled "1" and "2" show the location of the two-dimensional (2-D) forward gravity models shown in Figures 7 and 8, respectively. (b) The Moho depth beneath the TD and its surroundings obtained from the 2-D Lithoflex inversion of the Bouguer gravity anomalies of the EIGEN-6C4.

Recently, Corti et al. (2019) described the Ririba rift (Figure 4a) as a 10–25-km-wide zone of N-S trending normal faults. Using field observations, $^{40}Ar/^{39}Ar$ geochronological study, and numerical modeling, they suggested that the Ririba rift started propagating southward during the Pliocene, but this propagation seized during the Pliocene-Pleistocene due to the development of a direct link between the Main Ethiopian Rift and the Kenya rift within the TD. Further, they suggested that the rift development was strongly influenced by the presence of the penetrative preexisting Precambrian fabric.

2.6 Data and Methods

2.6.1 Data

The satellite gravity data I used in this study is EIGEN-6C4 (Figure 6a). The EIGEN-6C4 is a reconstruction of the Earth Gravity Model 2008 (EGM 2008) and contains the complete Satellite Gravity Gradiometry (SGG) data (Txx, Tyy, Tzz, Txz) of the Gravity Field and Steady-state Ocean Circulation (GOCE) mission (Bruinsma et al., 2014). This globally combined gravity field model is inferred from the Laser Geodynamics Satellite (LAGEOS), Gravity Recovery and Climate Experiment (GRACE), GOCE, and Danmarks Tekniske Universitet (DTU) ground data, and has spherical harmonic degrees of 2190. The spatial resolution of the EIGEN-6C4 data is ~9 km. Alongside with EIGEN-6C4 (Figure 6a), I use the Earth Topography 1 arc min (ETOPO1) Digital Elevation Model for an integrated 2-D and 3-D gravity inversion.

2.6.2 Methods

2.6.2.1 Moho Depth Imaging with Lithoflex

I used Lithoflex inversion to image the Moho depth beneath the TD and its surroundings (Figure 6b). In this inversion, I consider the Moho to be represented by the density interface between the crust and the SCLM. Lithoflex has been successfully used elsewhere to determine the depth to Moho, flexural rigidity, basement, and spatial variations of flexure parameters (e.g., Alemu et al., 2018; Braitenberg et al., 2002, 2003, 2006; Ebbing et al., 2007; Wienecke et al., 2007). Lithoflex uses the algorithm developed by Braitenberg et al. (2002), which, among other functionalities, it performs Moho depth gravity inversion modeling as a function of reference depth to Moho, density contrast between the crust and SCLM, and filtering cutoff wavelength. The Lithoflex inversion iterates the Fourier analysis of the topography, and inverts it based on the Moho reference depth through the inverse Fourier transform. For this model, I use topographic data obtained from the GTOPO1. I assigned a value of 24 km for the reference depth to Moho based on the depth obtained from the controlled source seismic data for the central part of the Lake Turkana rift basin (Keller et al., 1994). I also assign a value of 0.5 gm/cm^3 for the density contrast between the crust and SCLM and a value of 150,000 m for the filtering cutoff wavelength. I use this filtering cutoff wavelength to enable the inversion model to suppress wavelengths that are smaller than 150 km. This helps in limiting the potential projection of the superficial masses to the Moho level. Moreover, I chose to use a relatively high density contrast (0.5 gm/cm^3) between the crust and SCLM. This is to ensure defining the Moho interface within the zone of high-density difference between the crust (2.6 gm/cm^3) and SCLM (3.1 gm/cm^3). I use the initial Moho reference depth of 24 km to complete the first test of delineating the assigned density contrast between the crust and SCLM. Subsequently, through multiple iterations, I approximate the boundary between the crust and SCLM through different depth solutions that satisfy the assigned density contrast.

2.6.2.2 Lithospheric Imaging with 2-D Forward Gravity Modeling

I used 2-D forward gravity modeling to produce lithospheric scale cross sections for the TD and its surroundings including the depth to the upper and middle crust boundaries, the depth to Moho, and the depth to lithosphere-asthenosphere boundary (LAB). For this, I use the GYMSYS Oasis Montaj software to model the Bouguer gravity anomalies of the EIGEN-6C4. This software uses an algorithm first published by Talwani et al. (1959) and was later updated by Won and Bevis (1987).

I produce two 2-D forward gravity models to the depth of 50 and 300 km. The first models follow a N-S direction along longitude 36°E and extend from 5°N to 2°S. These models cover the eastern side of the East Africa plateau in the south and the TD along the trace of the Lake Turkana rift basin to the north (shown with dashed white line labeled "1" in Figure 6a). This baseline is selected to use results obtained for the depth to the upper and middle crust boundaries and the Moho from the controlled source seismic imaging of Keller et al. (1994) as constraints (shown with solid white line in Figure 6a). I also aim at characterizing the lithospheric structure beneath the TD bounded by the Ethiopia-Yemen plateau in the northeast and the East Africa plateau to the southwest. Hence, I develop another set of models extending in a NE-SW direction from 5°N and 40°E to 2°S and 33°E (shown with dashed white line labeled "2" in Figure 6a). For all models, I use density values of 3.3 gm/cm^3 for the asthenosphere, 3.1 gm/cm^3 for the SCLM, 2.95 gm/cm^3 for the lower crust, 2.85 gm/cm^3 for the middle crust, and 2.67 gm/cm^3 for the upper crust. Mafic magmatic underplating was reported by Thybo et al. (2000) beneath the Kenya rift from controlled source seismic imaging. This mafic magmatic underplating is centered around 2°S and 36°30′E to the southeast of the 2-D forward gravity models. Hence, I did not account for mafic magmatic underplating through the introduction of an additional density value in the models.

2.6.2.3 Mapping Upper Crust Density Distribution With Inversion of Gravity Data Over 3-D Structure

In order to characterize the dominant upper crustal structural expressions within the TD, I develop a 3-D density distribution model for the Kino Sogo fault zone (Figures 4a and 4b) to a depth of 14.5 km. I select the Kino Sogo fault belt because it has well-exposed and distinct N-S trending pattern of horst and graben structure (Figure 4b) that are expected to overprint possibly underlying NW trending structure associated with the Anza rift. The region covered by the model coincides with that shown in Figure 4b. I use the Inversion of Gravity Data over 3D Structure (GRAV3D) software. The GRAV3D software was developed by the University of British Colombia Geophysical Inversion Facility based on an algorithm developed by Li and Oldenburg (1998). This 3-D inversion integrates the residual Bouguer gravity anomalies of EIGEN-6C4 with topography obtained from GTOPO1 data. The algorithm conducts the inversion as an optimization problem of finding the best fit by using the density model identifier such that the result is produced within the error tolerance limit. The densities I use for the 3-D inversion are 2.4 and 2.8 gm/cm^3 for the upper and lower bounds, respectively. I set the model with an initial density value of 2.43 gm/cm^3 in order to isolate trends of low-density responses from the residual gravity anomalies and topography data. Subsequently, I test the initial model against the lower (2.4 gm/cm^3) and upper (2.8 gm/cm^3) density bounds to satisfy the observed residual gravity anomalies with solutions that are within 95% confidence interval.

The original EIGEN-6C4 has a spatial resolution of 9 km. Hence, to overcome the shortcoming of the poor spatial resolution, I use a residual grid containing the high-frequency information extracted from the Bouguer gravity anomalies of the EIGEN-6C4 in the GRAV3D inversion. To produce the residual grid, I subtract the grid containing the original Bouguer gravity anomalies from a gird that is smoothed by the Hanning filter. This residual grid is expected to represent the upper crustal geological features that are resolvable because the regional Bouguer

gravity anomalies are removed. Further, to account for any error in finding the optimal inversion solution, I use the generalized cross-validation approach. This approach assumes that a good solution to the inverse problem is one that is not overly sensitive to any particular datum (Oldenburg & Li, 2005).

2.7 Results

2.7.1 Bouguer Gravity Anomalies

The TD is characterized by the presence of high Bouguer gravity anomalies reaching ~ −30 mGal in the southeastern part of the depression (Figure 6a). This is different from the southwestern part of the Ethiopia-Yemen plateau, which is characterized by a relatively low Bouguer gravity anomalies reaching ~ −160 mGal (Figure 6a). The high Bouguer gravity anomalies dominating the TD are sharply different from the low Bouguer gravity anomalies dominating the East Africa plateau to the southwest that reach ~ −210 mGal (Figure 6a). I attribute the presence of high Bouguer gravity anomalies within the TD to a combined effect of denser lithological units such as basalt and an underlying thinner crust (see section 4.2). I also attribute the presence of significantly low Bouguer gravity anomalies within the East Africa plateau to two effects. These include the presence of less dense material of the Precambrian cratons, metacraton and orogenic belts such as gneisses and granites (Figure 3b), and the presence of an underlying thicker crust (see section 4.2). I further attribute the presence of relatively low Bouguer gravity anomalies within the Ethiopia-Yemen plateau to the presence of less dense Precambrian gneisses and migmatities that dominate the southwestern part of the plateau (Figure 3b).

2.7.2 The Depth to Moho

The results from the Moho depth map of the TD and its surrounding show clear thinning of the crust beneath the depression, especially close to the northeastern margin of the East Africa plateau where the thickness of the crust ranges between 23 and 28 km (Figure 6b). The thinner crust beneath the TD is surrounded in the northeast and southwest by a relatively thicker crust beneath the Ethiopia-Yemen plateau and the East Africa plateau (Figure 6b). The crust in the northeastern part of the East Africa plateau becomes as thick as ~40 km (Figure 6b). This is in good agreement with the seismic reflection results of KRISP Working Group (1991), Keller et al. (1994), Mechie et al. (1994), and Prodehl et al. (1994), which show that the crust in this part of the East Africa plateau is ~35 km thick.

The thinner crust within the TD shows an overall NW-SE trend parallel to the assumed strike of the KSR. However, I observe finer crustal thinning patterns within the overall NW-SE trend of thinner crust. First, the trend of the thinner crust is not centered beneath the central part of the depression. Rather, this thinning of the crust follows the region to the northeast of the East Africa plateau (Figure 6b). However, I found the thinnest crust (~23 km) to be in the southeastern side of the TD (labeled "SE" in Figure 6b). Second, I observe an E-W trending zone of thinner crust in the northwestern part of the TD west of the northern tip of the Lake Turkana rift basin (labeled E-W in Figure 6b). The thickness of the crust in the central part of this E-W trending zone reaches ~23 km (Figure 6b). This zone of E-W crustal thinning is confined to latitudes 4°N and 5°N and stretches between longitudes 34°E and 37°E (Figure 6b). Third, I observed a N-S trending zone of thinner crust (26–27 km) immediately to the west of the southern half of the Lake Turkana rift basin (labeled N-S in Figure 6b). This zone of N-S crustal thinning is confined between longitude 35°E and 36°E and stretches between latitudes 3°30′N and 4°N (Figure 6b). I note that the zone of E-W crustal thinning coincides and immediately to the east of the proposed northwestern continuation of the Anza rift represented by the Loelli basin (Figure 2a). This is where the Anza rift rotates slightly to the west to

connect with the Mongala basin through the South Sudan shear zone (Figure 2a; Bosworth, 1992). In addition, it is possible that the zone of N-S crustal thinning is associated with the tectonic extension that resulted in the formation of the Lake Turkana rift basin and that this crustal thinning was superimposed on the overall NW-SE crustal thinning beneath the KSR.

The thinning of the crust beneath the TD is also evident from the 2-D forward gravity model that is constrained by results of the controlled source seismic imaging of Keller et al. (1994). The first 2-D forward gravity model follows longitude 36°E and stretches between latitudes 2°S and 5°N (Figure 6a). The northern half of the model extends within the TD following the trace of the Lake Turkana rift basin, whereas the southern half of the model extends within the eastern side of the East Africa plateau (Figure 7a). The 2-D forward gravity model shows gradual thinning of the middle and lower crust from south to north (Figure 7a). I find the thickest crust to be beneath the East Africa plateau reaching a maximum thickness of ~35 km (Figure 7a). I also find the thinnest crust to be beneath the Lake Turkana rift basin reaching ~20 km. This is in good agreement with results from the controlled source seismic imaging of KRISP Working Group (1991), Keller et al. (1994), Mechie et al. (1994), and Prodehl et al. (1994), which show progressive thinning of the middle and lower crust from the East Africa plateau to the Lake Turkana rift basin within the TD. The lower boundaries of the upper, middle, and lower crust as defined by the controlled source seismic imaging of Keller et al. (1994) are shown with thick white line in Figure 7a. The controlled source seismic imaging of Keller et al. (1994) shows the depth to Moho in the southwestern side of the Lake Turkana rift basin to be as shallow as ~21 km.

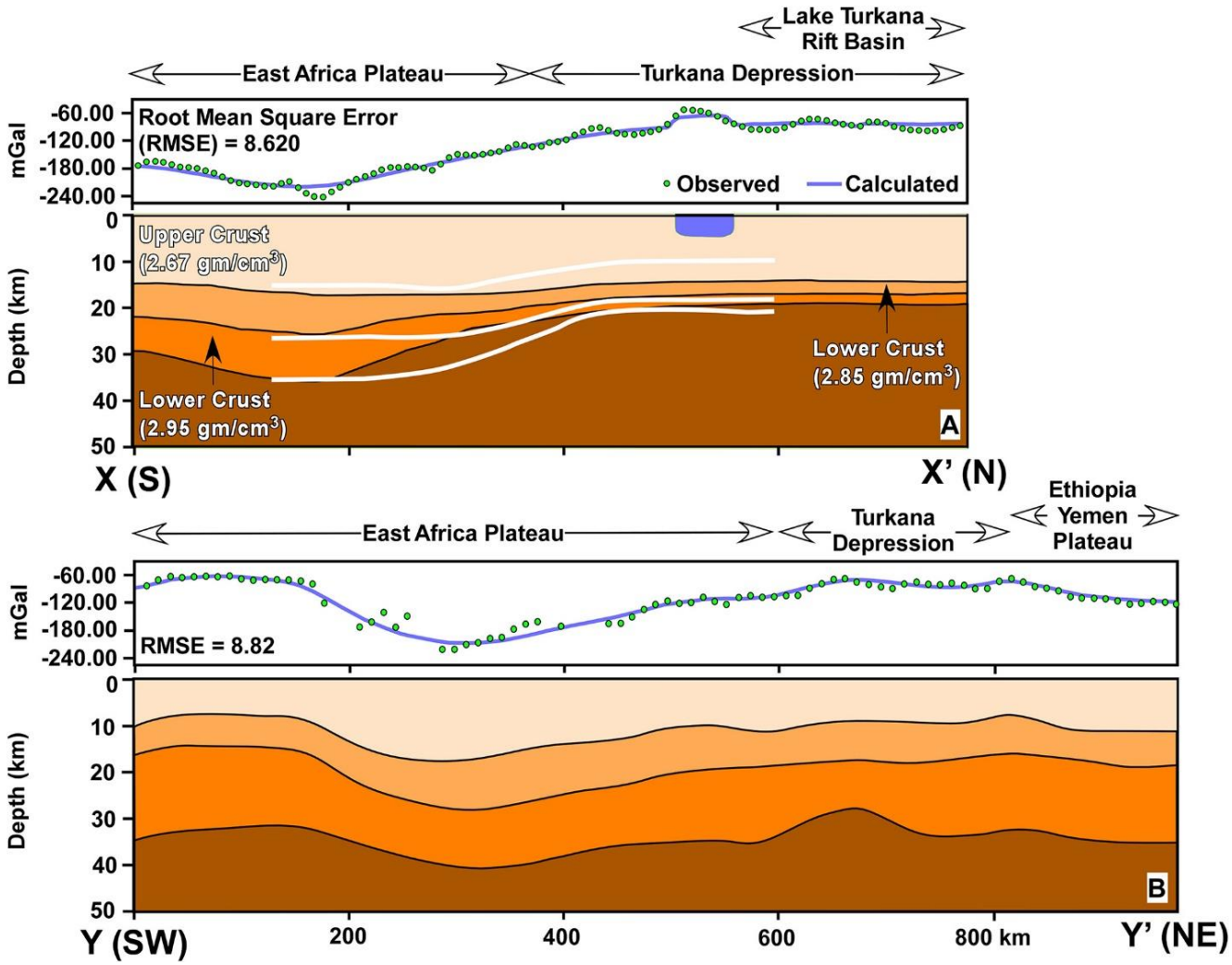

Figure 2.7: (a) N-S and (b) NE-SW two-dimensional (2-D) forward gravity models showing the crustal structure beneath the Turkana Depression (TD) and its surroundings. See Figure 6 for the location of the models. The thick white lines in the N-S model in (a) represent the boundaries of the upper, middle, and lower crust as defined by the controlled source seismic data of Keller et al. (1994). The N-S model in (a) shows thinner crust beneath the TD and the Lake Turkana rift basin. The NE-SW model in (b) shows relatively thin crust beneath the TD.

The results showing thinner crust beneath the TD are also in good agreement with those obtained from Rayleigh wave dispersion measurements by Benoit et al. (2006). Benoit et al. (2006) obtained crustal thickness ranging between ~26 and ~30 km and an average crustal thickness of ~25 km for the TD. This is almost identical to the crustal thickness of 23–28 km I obtained for the TD.

The Moho depth results are also in general agreement with Moho depth estimates obtained from broadband passive seismic receiver function analysis by Plasman et al. (2017). Two of the passive seismic stations used by these authors to image the Moho beneath the North Tanzania Divergence are located in the southernmost part of the study area. These stations are shown with red triangles labeled KEN2 and KEN4 in Figure 6b. Plasman et al. (2017) obtained a Moho depth of 28.0 km for station KEN2 and a Moho depth of 37.1 km for station KEN4. I find the 28.0-km Moho depth obtained by Plasman et al. (2017) for station KEN2 to be slightly shallower than the Moho depth of 32 km I obtained for this site (Figure 6b). I note here that these authors reported an error of 6.8 km for the Moho depth estimated for station KEN2. For this site, I calculate an error of 1.42 km for the 32-km Moho depth I obtained from the inversion of the Bouguer gravity anomalies of the EIGEN-6C4. I find the Moho depth of 37.1 km obtained by Plasman et al. (2017) for station KEN4 to be almost identical to the Moho depth of 35 km I obtain for this site given that the error reported by these authors for this station is 1.7 km. For this site (KEN4), I calculate an error of 1.56 km for the 35-km Moho depth I obtain from the inversion of the Bouguer gravity anomalies of the EIGEN-6C4.

The second 2-D forward gravity model runs in a NE-SW direction from the central part of the East Africa plateau to the southwestern part of the Ethiopia-Yemen plateau (shown with dashed white line labeled “2” in Figure 6a). This model crosses the entire TD, but does not encounter the Lake Turkana rift basin as in the case of the first model (Figure 6a). Similar to the first model, I find in the second model the thickest crust to be beneath the East Africa plateau reaching ~40 km (Figure 7b). Generally, the crust becomes thinner toward the northeast and it is thinnest in the southwestern side of

the TD reaching ~28 km (Figure 7b). This is in good agreement with results from the 2D gravity inversion of the Bouguer gravity anomalies EIGEN-6C4 (Figure 6b).

2.7.3 The Depth to LAB

The results from imaging the LAB using 2-D forward gravity modeling show that the TD is underlain by a relatively thin lithosphere. The 2-D forward gravity model that stretches N-S from the eastern side of the East African plateau into the TD following the trace of the Lake Turkana rift basin (shown with dashed white line labeled "1" in Figure 6a) shows thick lithosphere beneath the East Africa plateau reaching ~200 km (Figure 8a). The lithosphere becomes progressively thinner northward beneath the TD and the Lake Turkana rift basin reaching ~150 km in the central part of the depression and the northern part of the Lake Turkana rift basin (Figure 8a). I observe similar thinning of the lithosphere beneath the TD in the NE-SW trending 2-D forward gravity model that stretches from the central part of the East Africa plateau to the southwestern part of the Ethiopia-Yemen plateau (shown with dashed white line labeled "2" in Figure 6a). This model shows that the Ethiopia-Yemen plateau is underlain by a relatively thick lithosphere reaching ~200 km (Figure 8b). The lithosphere thins from ~200 km beneath the East Africa plateau to ~140 km beneath the TD (Figure 8b). Northeast of the TD on the southwestern edge of the Ethiopia-Yemen plateau, the lithosphere slightly thickens to ~160 km before gradually thins toward the Ethiopia-Yemen plateau to reach ~120 km (Figure 8b).

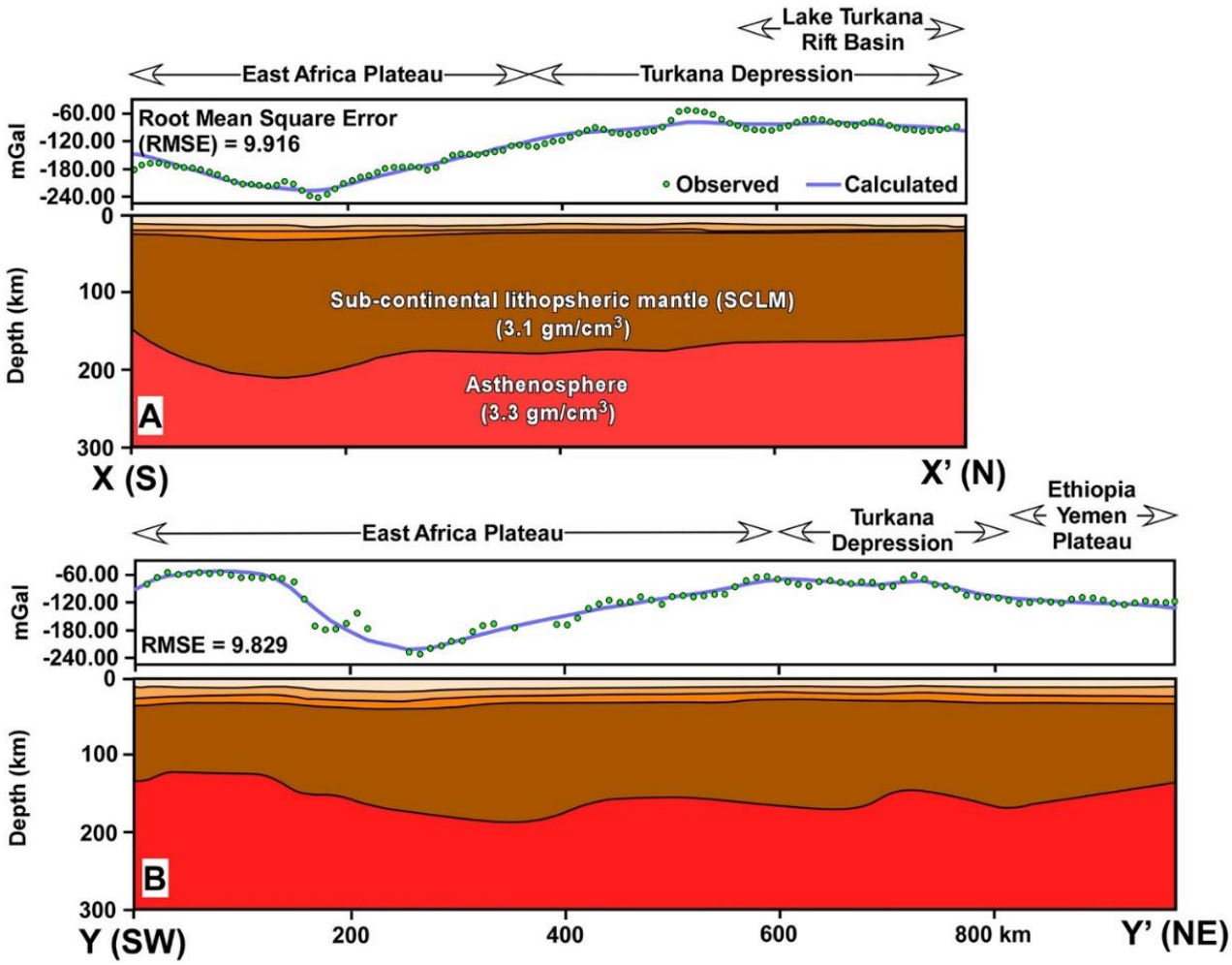

Figure 2.8: (a) N-S and (b) NE-SW two-dimensional (2-D) forward gravity models showing the lithospheric structure beneath the Turkana Depression (TD) and its surroundings. See Figure 6 for the location of the models. The N-S model in (a) shows thinner lithosphere beneath the TD and the Lake Turkana rift basin. The NE-SW model in (b) shows relatively thin lithosphere beneath the TD. The unit of the RMSE is mGal.

The estimations of the thickness of the lithosphere I obtain for the TD and its surrounding from the 2-D gravity inversion of the Bouguer gravity anomalies EIGEN-6C4 are in good agreement with regional lithospheric thickness estimates by Priestley and McKenzie (2006) that show a general thinning of the lithosphere from the East Africa plateau toward the TD. In addition, the general topography of the LAB I image from the 2-D forward gravity models is in agreement with a regional profile presented by Craig et al. (2011) that showed general shallowing of the LAB from the East

Africa plateau toward the Ethiopia-Yemen plateau to reach ~100 km beneath the Main Ethiopian Rift and the Afar Depression. The thinner lithosphere (~140 to ~150 km) I imaged for the TD is also in good agreement with results of upper mantle seismic velocity structure that found slow *Sn* wave (4.1–4.3 km/s) and *S* wave (4.0–4.2 km/s) velocities at upper mantle depth (100–150 km) beneath the TD (Benoit et al., 2006; Emry et al., 2019).

2.7.4 The 3-D Density Distribution Model

The 3D density distribution model I produce from the inversion of the residual of the Bouguer gravity anomalies of the EIGEN 6C4 covering the Kino Sogo fault belt shows different density distribution patterns at different depth. In this model, I densities ranging between 2.4 and 2.8 gm/cm^3. There are no Mesozoic sediments underlying the Kino Sogo fault zone and the grabens of the fault zone itself have no significant throw to accumulate significant amount of Cenozoic sediments (Vetel et al., 2005; Vetel & Le Gall, 2006). Hence, I consider these density differences to be related to the proportional presence of interleaving geological units such as Precambrian crystalline basement rocks, Cenozoic basaltic rocks, and possibly Mesozoic and Cenozoic mafic dikes at depth. I observe that the density distribution model at 0-km depth shows subtle N-S trending density contrast anomalies (Figure 9a). It is possible that the lack of clarity of the N-S trending anomalies is due to the weak nature of density contrasts at this shallow level. I also observe that the density distribution model at 4.8-km depth is characterized by the presence of strong N-S and E-W density contrast anomalies and that the N-S density contrast anomalies seem to be narrower than the E-W density contrast anomalies (Figure 9b). Further, I observe that the density distribution model at 9.8-km depth is dominated by broad E-W density contrast anomalies (Figure 9c). I discuss the significance of the depth variation of in the density contrast anomalies under section 5.2.

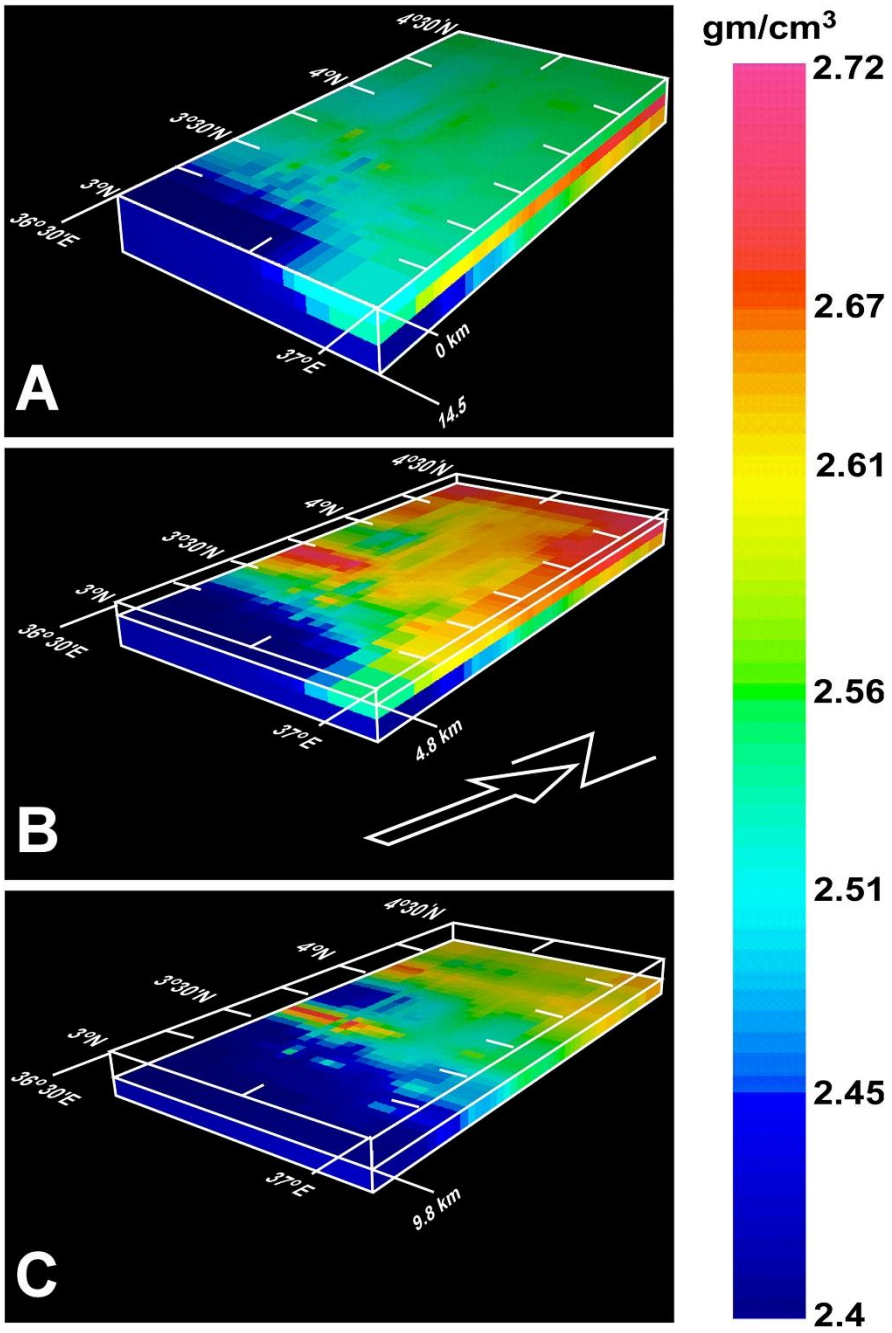

Figure 2.9: Three-dimensional (3-D) density distribution model of the Kino Sogo fault belt and the underlying structure within the Turkana Depression (TD). See Figures 4a and 4b for the location of the region within the TD covered by the model. (a) Density distribution model at 0-km depth. At this depth, the model shows subtle N-S trending density contrast anomalies. (b) Density distribution model at 4.8-km depth. At this depth, the model shows both N-S and E-W density contrast anomalies. (c) Density distribution at 9.8-km depth. At this depth, the model shows E-W density distribution anomalies.

2.8 Discussion

2.8.1 Origin of the Lithospheric Structure Beneath the TD

The fact that the Neogene-Quaternary EARS, which intersects the late Jurassic-early Paleogene KSR within the TD, is younger extensional tectonic feature is a compelling reason to assume that the lithospheric structure in the region has been largely influenced by the EARS. The expectation would be that the observed crustal and lithospheric thinning will follow the surface expression of the EARS rather than that of the KSR. However, the results show that the trend of the dominant crustal thinning is NW-SE following what has been suggested to be the trend of KSR (e.g., Bosworth, 1992; Dou et al., 2007; Fairhead, 1988). This is particularity evident from the Moho depth results obtained from the 2-D inversion of the Bouguer gravity anomalies of the EIGEN-6C4 (Figure 6b).

The Moho depth estimates from the 2-D inversion also show the presence of thicker crust northeast and southwest of the TD, especially beneath the East Africa plateau (Figure 6b). The presence of a thicker crust beneath the East Africa plateau can easily be explained as due to a combined effect of the presence of Precambrian cratons and orogenic belts and isostatic compensation due to elevated topography. It is less clear to us why there is a relatively thick crust beneath the southwestern part of the Ethiopia-Yemen plateau since this region is dominated by the broadly rifted zone of the Main Ethiopian Rift (e.g., Emishaw et al., 2017). Receiver function passive seismic studies by Dugda et al. (2005) and Keranen et al. (2009) in the broadly rifted zone immediately north of the study area calculated crustal thickness ranging between 38 and 27 km for 10 of the broadband seismic stations used in these studies. Nonetheless, thick crust ranging between 40 and 42 km has also been reported for five of the broadband seismic stations used in these studies (Dugda et al., 2005; Keranen et al., 2009). Mafic underplating has been observed from the inversion of gravity data

beneath the Northwestern plateau to the west of the Main Ethiopian Rift (Figure 1; Tiberi et al., 2005). However, based on the lack of high Bouguer gravity anomalies, Emishaw et al. (2017) suggested that the presence of thick crust beneath the broadly rifted zone cannot be due to mafic underplating that might have accompanied the formation of the EARS. Hence, it is possible that the relatively thick crust beneath the southwestern part of the Ethiopia-Yemen plateau was present since the formation of the KSR. It is possible that this thick crust was inherited from a tectonic event as old as the Neoproterozoic such as the collision between East and West Gondwana along the East African orogen (Abdelsalam & Stern, 1996; Fritz et al., 2013; Stern, 1994).

I further suggest that the initial thinning of the crust beneath the TD occurred as a result of late Jurassic-early Paleogene NE-SW tectonic extension that resulted in the formation of the KSR. It is possible that additional thinning of the crust beneath the TD occurred due to Neogene-Quaternary E-W tectonic extension that resulted in the formation of segments of the EARS including the Turkana rifted zone. This is in good agreement with Morley et al. (1992) and Morley (1994) who proposed that the Moho topography that is observed today might be due to cumulative effect of the superposition of segments of the EARS on the KSR.

2.8.2 Origin of Depth Variation of the Density Contrast Anomalies Beneath the Kino Sogo Fault Belt

As mentioned above, it is likely that the crustal thinning beneath the TD is due to the extension that resulted in the formation of the KSR in addition to superimposition of tectonic extension that produced the EARS. The 3-D density distribution model shows that the crust beneath the Kino Sogo fault belt to a depth of 4.8 km is characterized by N-S trending density contrast anomalies (Figure 9b) and these anomalies are subparallel to the N-S trend of the fault belt itself

(Figure 4b). Hence, it is tempting to consider the cause of the N-S density contrast anomalies to be the alternation of the horsts and grabens of the Kino Sogo fault belt.

However, as mentioned before the horsts and grabens of the fault belt are 1 to 2 km wide, which dissect Cenozoic lava flows and that the grabens do not contain any significant amount of Cenozoic sediments (Vetel et al., 2005; Vetel & Le Gall, 2006). Alternatively, it is possible that the cause of the N-S trending density contrast anomalies is the presence of N-S trending Precambrian structure defined by the alternation of geological units with varied densities. The Precambrian structure might have facilitated strain localization during the onset of the Kino Sogo fault belt. It is worth mentioning here that the Kino Sogo fault belt crops out between the Precambrian Tulu-Dimtu and Adola-Moyale belts; both are characterized by interleaving of N-S trending zones of gneisses and migmatities on the one hand and volcano-sedimentary rocks with ophiolite fragments on the other hand (Figures 3a and 3b).

The 3-D density distribution model also shows that the crust beneath 4.8-km depth is dominated by E-W trending density contrast anomalies (Figure 9b). The cause of these density contrast anomalies cannot be directly related to sediments-filled grabens related to the Anza rift. This is because no Mesozoic sediments are recorded beneath the Kino Sogo fault belt (Vetel et al., 2005; Vetel & Le Gall, 2006). It is true that the overall trend of the Anza rift has been established from geophysical data as being NW-SE (e.g., Bosworth, 1992; Bosworth & Morley, 1994; Dindi, 1994; Morley, Day, et al., 1999). However, it is possible that the rift geometry is further shaped by the presence of E-W trending structure. For example, from outcrop data, Williamson and Savage (1986) have shown that the Cretaceous-Paleogene Turkana Grits west of the Lake Turkana rift basin are deformed by E-W trending dextral strike-slip faults and these faults might have formed after an early rifting structure. Hence, it is possible that the source the E-W trending density contrast anomalies beneath the Kino Sogo fault belt is the presence of E-W trending zones of discontinuities in the form

of dextral strike-slip faults. However, it is also possible that the cause of the density contrast anomalies is transverse faults associated with the development of the Turkana rifted zone.

These Mesozoic and/or Cenozoic E-W trending faults might have guided the upward migration of Cenozoic magmatism that is apparent in the surface as extensive basaltic flows within the Kino Sogo fault zone (Vetel et al., 2005; Vetel & Le Gall, 2006). Portions of the magma might have crystallized within the E-W trending faults as mafic dikes, hence resulting in the strong E-W trending density contrast anomalies. Nonetheless, I do not rule out the presence of Mesozoic mafic dikes. Mafic sills were reported from controlled source seismic imaging by Bosworth and Morley (1994) from the central part of the Anza rift close to base of the Cretaceous-Paleogene sediments at depth ranging between ~5 and ~9 km (Figure 2b).

2.8.3 The Role of the Precambrian Structure

The regional Precambrian tectonic map of the TD and its surroundings proposes possible correlation of dominant structure across the depression (Figure 3b; e.g., Fritz et al., 2013). The N-S trending low-grade volcano-sedimentary belts in southern Ethiopia (Tulu-Dimtu and Adola-Moyale) have been correlated to shear zones in Kenya (Mutito and Nyangere) across the TD (Figures 3a and 3b). This suggests that these Precambrian belts have no influence on the evolution of the NW-SE trending KSR. However, here I draw attention to three observations that highlight the importance of the Precambrian structure in the evolution of the KSR. First, the TD coincides with fundamental changes in the lithospheric structure of the Precambrian blocks. In the southwest within the East Africa plateau, the Precambrian blocks are dominantly Archean to Mesoproterozoic cratons, metacraton, and orogenic belts constituting medium to high-grade metamorphic rocks (Figure 3b). To the northeast, the southwestern part of the Ethiopia-Yemen plateau is dominated by the interleaving of the Neoproterozoic low- and high-grade metamorphic belts of the Arabian-Nubian Shield. Second,

the northeastern margin of the East Africa plateau is occupied by the Neoproterozoic Sekerr fold and thrust belt, which represents the suture zone between the Saharan Metacraton in the southwest and the Arabian-Nubian Shield to the northeast (Figure 3b; Abdelsalam & Dawoud, 1991). Third, the Aswa shear zone is found in the northeastern side of the East Africa plateau separating the Saharan Metacraton in the northeast from the Northeast Congo block to the southwest. It has been suggested that the continuation of the Aswa shear zone to the northwest in South Sudan had a significant influence in strain localization during the late Jurassic-early Paleogene rifting event (Daly et al., 1989). The Aswa shear zone also marks significant difference in seismic structure across it. Faster *S* wave velocities are observed southwest of the shear zone and slower velocities are observed northeast of it (Abdelsalam et al., 2011; Katumwehe et al., 2016). Hence, it is possible that the KSR was localized at the interface of two Precambrian blocks, possibly thicker and older lithosphere in the southwest and thinner and juvenile lithosphere to the northeast.

2.8.4 Implications for the Development of the Eastern Branch of the EARS

The Turkana rifted zone within the TD is an anomalously wide (~300 km) zone of distributed extension constituting several rift basins (Figures 4a, 4b, 5a, and 5b; Dunkelman et al., 1989; Morley, Day, et al., 1999; Rosendahl et al., 1992; Vetel et al., 2005; Vetel & Le Gall, 2006). It has long been suggested that the thickness and thermal structure of the lithosphere can significantly influence the distribution of extensional strain and the width of the rifted zone (e.g., Buck, 1991). For example, Kogan et al. (2012) used Global Positioning System measurements to relate the width of the zones within which extensional strain is accommodated within the Afar Depression and the Main Ethiopian Rift to the thickness and thermal structure of the lithosphere. They attributed the wide zone (~175 km) within which extensional strain is accommodated in the Afar Depression to the virtual absence of the SCLM beneath the depression. In addition, they attributed the relatively narrow zone (~85 km) within which extensional strain is accommodated within the northern Main Ethiopian Rift to the

presence of anomalously thin and hot lithosphere. Further, Kogan et al. (2012) explained the extremely narrow zone (<10 km) within which extensional strain is accommodated within the southern Main Ethiopian Rift as due to the presence relatively thicker lithosphere.

Differently, Koptev et al. (2018) used thermo-mechanical numerical models guided by observations from the Eastern Branch of the EARS to examine the relationship between the width of rift segments and the interaction of an uprising mantle plume head with the base of a laterally homogeneous lithosphere. They explained that the Kenya rift developed as a narrow rift segment within the Eastern Branch because of an uprising mantle plume head (Kenya plume head) beneath the rift that heated the lithosphere, and hence thermally weakened it. On the other hand, Koptev et al. (2018) explained the development of the Turkana rifted zone within the TD in the north and the North Tanzania Divergence to the south (Figure 3a) as wide rift segments as due to the presence of colder lithosphere beneath these rift segments of the Eastern Branch.

The results show evidence for thinning of both the crust and the lithosphere beneath the TD. In addition, upper mantle velocity results found slow *Sn* and *S* wave velocities beneath the TD (Benoit et al., 2006; Emry et al., 2019), and these slow velocities might be suggestive of the presence of hot lithosphere beneath the depression. Hence, I attribute the development of the Turkana rifted zone as an anomalously wider rift zone within the Eastern Branch of the EARS to prior thinning of the lithosphere that took place in association with the formation of the KSR during the late Jurassic to early Paleogene. This suggestion is in good agreement with results of analog experiments and numerical models presented by Brune et al. (2017) for the Turkana rifted zone within the TD. Brune et al. (2017) attributed the wide zone within which extensional strain is accommodated across the Turkana rifted zone to the presence of thin crust that was inherited from the late Jurassic-early Paleogene tectonic extension, which resulted in the development of the KSR. In addition, they

attributed the fact the Main Ethiopian Rift and the Kenya rift did not connect directly to each other, but rather rotated away from each other, to the presence of this thin crust.

2.9 Conclusion

Results that I obtained from imaging the crustal and lithospheric thickness beneath the TD and its surroundings using 2-D inversion and 2-D forward gravity modeling of the Bouguer gravity anomalies of the EIGEN-6C4 show thinner crust (between 23 and 28 km) and lithosphere (between 140 and 150 km) beneath the TD. This crustal and lithospheric thinning was due to late Jurassic-early Paleogene tectonic extension that resulted in the formation of the KSR. Results I obtained from 3-D density distribution modeling of the EIGEN-6C4 covering the Kino Sogo fault belt show that the crustal depth between 0 and 4.8 km is dominated by N-S density contrast anomalies. These anomalies are reflective of the presence of strong N-S Precambrian fabric that facilitated localization of strain during the formation of the Kino Sogo fault belt. The crustal depth between 4.8 and 14.5 km beneath the Kino Sogo fault belt is dominated by E-W density contrast anomalies. These anomalies are associated with Mesozoic and or Cenozoic faults. These faults are E-W trending dextral strike-slip faults developed in association with the late Jurassic-early Paleogene KSR and/or transverse faults developed in association with the Neogene-Quaternary EARS. These faults were subsequently intruded by mafic dikes that represent the feeder dikes of the Cenozoic magmatism and subsurface mafic dikes of Mesozoic magmatism. The result suggests that the Anza rift is connected to the Sudan and South Sudan rift at depth although an apparent surface expression of this connection can be lacking in places within the TD.

2.10 References

Abdelsalam, M. G., & Dawoud, A. S. (1991). The Kabus ophiolitic melange, Sudan, and its bearing on the western boundary of the Nubian Shield. Journal of the Geological Society, 148(1), 83–92.

Abdelsalam, M. G., Gao, S. S., & Liégeois, J. P. (2011). Upper mantle structure of the Saharan Metacraton. Journal of African Earth Sciences, 60(5), 328–336.

Abdelsalam, M. G., Liégeois, J. P., & Stern, R. J. (2002). The Saharan Metacraton. Journal of African Earth Sciences, 34(3-4), 119–136.

Abdelsalam, M. G., & Stern, R. J. (1996). Sutures and shear zones in the Arabian-Nubian Shield. Journal of African Earth Sciences, 23(3), 289–310.

Abdelsalam, M. G., Tsige, L., Yihunie, T., & Hussien, B. (2008). Terrane rotation during the East African Orogeny: Evidence from the Bulbul Shear Zone, south Ethiopia. Gondwana Research, 14(3), 497–508.

Alemu, T., Abdelsalam, M. G., Dawit, E. L., Atnafu, B., & Mickus, K. L. (2018). The Paleozoic-Mesozoic Mekele Sedimentary Basin in Ethiopia: An example of an exhumed IntraCONtinental Sag (ICONS) basin. Journal of African Earth Sciences, 143, 40–58.

Arambourg, C. 1943. Contribution a l'etude geologique et paleontologique du Bassin du Lac Rodolphe et de la Basse Vallee de L'Omo. Museum d'Historie Naturelle, Paris 1, I(2), 157–230.

Baker, B.H., Mohr, P.A., & Williams, L.A.J. 1972. Geology of the Ethiopian Rift System. Special Papers of the Geological Society of America 136, 66 p.

Benoit, M. H., Nyblade, A. A., & Pasyanos, M. E. (2006). Crustal thinning between the Ethiopian and East Africa plateaus from modeling Rayleigh wave dispersion. Geophysical Research Letters, 33, L13301.

Binks, R. M., & Fairhead, J. D. (1992). A plate tectonic setting for Mesozoic rifts of West and Central Africa. Tectonophysics, 213(1-2), 141–151.

Bonini, M., Corti, G., Innocenti, F., Manetti, P., Mazzarini, F., Abebe, T., & Pecskay, Z. (2005). Evolution of the Main Ethiopian Rift in the frame of Afar and Kenya rifts propagation. Tectonics, 24, TC1007.

Bosworth, W. (1992). Mesozoic and early Tertiary rift tectonics in East Africa. Tectonophysics, 209(1-4), 115–137.

Bosworth, W., & Morley, C. K. (1994). Structural and stratigraphic evolution of the Anza rift, Kenya. Tectonophysics, 236(1-4), 93–115.

Braitenberg, C., Ebbing, J., & Götze, H.-J. (2002). Inverse modeling of elastic thickness by convolution method—The Eastern Alps as a case example. Earth and Planetary Science Letters, 202(2), 387–404.

Braitenberg, C., Wang, Y., Fang, J., & Hsu, H. T. (2003). Spatial variations of flexure parameters over the Tibet-Quinghai Plateau. Earth and Planetary Science Letters, 205(3-4), 211–224.

Braitenberg, C., Wienecke, S., & Wang, Y. (2006). Basement structure from satellite-derived gravity field: South China Sea ridge. Journal of Geophysical Research, 111, B05407.

Browne, S. E., & Fairhead, J. D. (1983). Gravity study of the Central African Rift System: A model of continental disruption 1. The Ngaoundere and Abu Gabra rifts. Tectonophysics, 94(1-4), 187–203.

Browne, S. E., Fairhead, J. D., & Mohamed, I. I. (1985). Gravity study of the White Nile Rift, Sudan, and its regional tectonic setting. Tectonophysics, 113(1-2), 123–137.

Bruinsma, S., Abrykosov, O., & Lemoine, J.M. 2014. The latest combined global gravity field model including GOCE data up to degree and order 2190 of GFZ Potsdam and GRGS Toulouse (EIGEN 6C4). In 5th GOCE user workshop, Paris. pp. 25–28.

Brune, S., Corti, G., & Ranalli, G. (2017). Controls of inherited lithospheric heterogeneity on rift linkage: Numerical and analog models of interaction between the Kenyan and Ethiopian rifts across the Turkana depression. Tectonics, 36, 1767–1786.

Buck, W. R. (1991). Models of continental lithospheric extension. Journal of Geophysical Research, 96(B12), 20,161–20,178.

Chorowicz, J. (2005). The East African Rift System. Journal of African Earth Sciences, 43(1-3), 379–410.

Corti, G., Cioni, R., Franceschini, Z., Sani, F., Scaillet, S., Molin, P., et al. (2019). Aborted propagation of the Ethiopian rift caused by linkage with the Kenyan rift. Nature Communication., 10(1).

Corti, G., Philippon, M., Sani, F., Keir, D., & Kidane, T. (2013). Re-orientation of the extension direction and pure extensional faulting at oblique rift margins: Comparison between the Main Ethiopian Rift and laboratory experiments. Terra Nova, 25(5), 396–404.

Craig, T. J., Jackson, J. A., Priestley, K., & McKenzie, D. M. (2011). Earthquake distribution patterns in Africa: Their relationship to variations in lithospheric and geological structure, and their rheological implications. Geophysical Journal International, 185(1), 403–434.

Daly, M. C., Chorowicz, J., & Fairhead, J. D. (1989). Rift basin evolution in Africa: The influence of reactivated steep basement shear zones. Geological Society of London Special Publications, 44(1), 309–334.

Delvaux, D. (2001). Karoo rifting in western Tanzania: Precursor of Gondwana breakup. Contributions to geology and paleontology of Gondwana in honor of Helmut Wopfner, (pp. 111–125). Cologne: Geological Institute, University of Cologne.

Dindi, E. W. (1994). Crustal structure of the Anza graben from gravity and magnetic investigation. Tectonophysics, 236(1-4), 359–371.

Dou, L., Xiao, K., Cheng, D., Shi, B., & Li, Z. (2007). Petroleum geology of the Melut Basin and the Great Palogue Field, Sudan. Marine and Petroleum Geology, 24(3), 129–144.

Dugda, M. T., Nyblade, A. A., Julia, J., Langston, C. A., Ammon, C. J., & Simiyu, S. (2005). Crustal structure in Ethiopia and Kenya from receiver function analysis: Implications for rift development in eastern Africa. Journal of Geophysical Research, 110, B01303.

Dunkelman, T. J., Rosendahl, B. P., & Karson, J. A. (1989). Structure and stratigraphy of the Turkana rift from seismic reflection data. Journal of African Earth Sciences, 8(2-4), 489–510.

Ebbing, J., Braitenberg, C., & Wienecke, S. (2007). Insights into the lithospheric structure and the tectonic setting of the Barents Sea region from isostatic considerations. Geophysical Journal International, 171(3), 1390–1403.

Ebinger, C. J., Yemane, T., Harding, D. J., Tesfaye, S., Kelley, S., & Rex, D. C. (2000). Rift deflection, migration, and propagation: Linkage of the Ethiopian and Eastern rifts, Africa. Geological Society of America Bulletin, 112(2), 163–176.

Emishaw, L., Laó-Dávila, D. A., Abdelsalam, M. G., Atekwana, E. A., & Gao, S. S. (2017). Evolution of the broadly rifted zone in southern Ethiopia through gravitational collapse and extension of dynamic topography. Tectonophysics, 699, 213–226.

Emry, E. L., Shen, Y., Nyblade, A. A., Flinders, A., & Bao, X. (2019). Upper mantle Earth structure in Africa from full-wave ambient noise tomography. Geochemistry, Geophysics, Geosystems, 20, 120–147.

Fairhead, J. D. (1988). Mesozoic plate tectonic reconstructions of the central South Atlantic Ocean: The role of the West and Central African rift system. Tectonophysics, 155(1-4), 181–191.

Fritz, H., Abdelsalam, M. G., Ali, K. A., Bingen, K. A., Collins, A. S., Fowler, A. R., et al. (2013). Orogeny style in the East African Orogen: A review of the Neoproterozoic to Cambrian tectonic evolution. Journal of African Earth Sciences, 86, 65–106.

Genik, G. J. (1992). Regional framework, structural and petroleum aspects of rift basins in Niger, Chad and the Central African Republic (CAR). Tectonophysics, 213(1-2), 169–185.

Genik, G. J. (1993). Petroleum geology of Cretaceous-Tertiary rift basins in Niger, Chad, and Central African Republic. American Association of Petroleum Geologists Bulletin, 77, 1405–1434. Greene, L. C.,

Richards, D. R., & Johnson, R. A. (1991). Crustal structure and tectonic evolution of the Anza rift, northern Kenya. Tectonophysics, 197(2-4), 203–211.

Guiraud, R., Bosworth, W., Thierry, J., & Delplanque, A. (2005). Phanerozoic geological evolution of Northern and Central Africa: An overview. Journal of African Earth Sciences, 43(1-3), 83–143.

Heilman, E., Kolawole, F., Atekwana, E. A., & Mayle, M. (2019). Control of basement fabric on the linkage of rift segments. Tectonics, 38, 1337–1366.

Hendrie, D. B., Kusznir, N. J., Morley, C. K., & Ebinger, C. J. (1994). Cenozoic extension in northern Kenya: A quantitative model of rift basin development in the Turkana region. Tectonophysics, 236(1-4), 409–438.

Katumwehe, A. B., Abdelsalam, M. G., Atekwana, E. A., & Laó-Dávila, D. A. (2016). Extent, kinematics and tectonic origin of the Precambrian Aswa Shear Zone in eastern Africa. Gondwana Research, 34, 241–253.

Keller, G. R., Mechie, J., Braile, L. W., Mooney, W. D., & Prodehl, C. (1994). Seismic structure of the uppermost mantle beneath the Kenya rift. Tectonophysics, 236(1-4), 201–216.

Keranen, K. M., Klemperer, S. L., Julia, J., Lawrence, J. F., & Nyblade, A. A. (2009). Low lower crustal velocity across Ethiopia: Is the Main Ethiopian Rift a narrow rift in a hot craton? Geochemistry, Geophysics, Geosystems, 10, Q0AB01.

Kogan, L., Fisseha, S., Bendick, R., Reilinger, R., McClusky, S., King, R., & Solomon, T. (2012). Lithospheric strength and strain localization in continental extension from observations of the East African Rift. Journal of Geophysical Research, 117, B03402.

Koptev, A., Calais, E., Burov, E., Leroy, S., & Gerya, T. (2018). Along-axis variations of rift width in a coupled lithosphere–mantle system, application to East Africa. Geophysical Research Letters, 45, 5362–5370.

KRISP Working Group (1991). The Kenyan Rift: Pure shear extension able a mantle plume. Nature, 345, 223–227.

Lemna, O. S., Stephenson, R., & Cornwell, D. G. (2019). The role of pre-existing Precambrian structures in the development of Rukwa Rift Basin, southwest Tanzania. Journal of African Earth Sciences, 15, 607–625.

Leseane, K., Atekwana, E. A., Mickus, K. L., Abdelsalam, M. G., Shemang, E. M., & Atekwana, E. A. (2015). Thermal perturbations beneath the incipient Okavango Rift Zone, northwest Botswana. Journal of Geophysical Research: Solid Earth, 120, 1210–1228.

Li, Y., & Oldenburg, D. W. (1998). 3-D inversion of gravity data. Geophysics, 63(1), 109–119.

Macgregor, D. (2018). History of the development of Permian–Cretaceous rifts in East Africa: A series of interpreted maps through time. Petroleum Geoscience, 24(1), 8–20.

Mann, D. C. (1989). Thick-skin and thin-skin detachment faults in continental Sudanese rift basins. Journal of African Earth Sciences, 8(2-4), 307–322.

Maurin, J. C., & Guiraud, R. (1993). Basement control in the development of the early Cretaceous West and Central African rift system. Tectonophysics, 228(1-2), 81–95.

McHargue, T. R., Heidrick, T. L., & Livingston, J. E. (1992). Tectonostratigraphic development of the interior Sudan rifts, central Africa. Tectonophysics, 213(1-2), 187–202.

Mechie, J., Keller, G. R., Prodehl, C., Gaciri, S., Braile, L. W., Mooney, W. D., et al. (1994). Crustal structure beneath the Kenya Rift from axial profile data. Tectonophysics, 236(1-4), 179–200.

Morley, C. K. (1994). Interaction of deep and shallow processes in the evolution of the Kenya rift. Tectonophysics, 236(1-4), 81–91.

Morley, C. K., Day, R. A., Lauck, R., Bosher, R., Stone, D. M., Wigger, S. T., et al. (1999). Geology and geophysics of the Anza Graben. American Association of Petroleum Geologists Studies in Geology, 44, 67–90.

Morley, C. K., Wescott, W. A., Stone, D. M., Harper, R. M., Wigger, S. T., Day, R. A., & Karanja, F. M. (1999). Geology and geophysics of the Western Turkana basins. American Association of Petroleum Geologists Studies in Geology, 44, 19–54.

Morley, C. K., Wescott, W. A., Stone, D. M., Harper, R. M., Wigger, S. T., & Karanja, F. M. (1992). Tectonic evolution of the northern Kenyan Rift. Journal of the Geological Society of London, 149(3), 333–348.

Murray-Hughes, R. 1933. Notes on the geological succession, tectonics and economic geology of the western half of Kenya colony. Reports of the Geological Survey of Kenya 3, 8 pp.

Nyblade, A. A., & Robinson, C. A. (1994). The African superswell. Geophysical Research Letters, 21(9), 765–768.

Oldenburg, D. W., & Li, Y. (2005). Inversion for applied geophysics: A tutorial. Investigations in Geophysics, 13, 89–150.

Plasman, M., Tiberi, C., Ebinger, C., Gautier, S., Albaric, J., Peyrat, S., et al. (2017). Lithospheric low-velocity zones associated with a magmatic segment of the Tanzanian Rift, East Africa. Geophysical Journal International, 210(1), 465–481.

Priestley, K., & McKenzie, D. (2006). The thermal structure of the lithosphere from shear wave velocities. Earth and Planetary Science Letters, 244(1-2), 285–301.

Prodehl, C., Jacob, B., Thybo, H., Dindi, E., & Stangl, R. (1994). Crustal structure on the northern flank of the Kenya rift. Tectonophysics, 236(1-4), 271–290.

Reeves, C. V., Karanja, F. M., & MacLeod, I. N. (1987). Geophysical evidence for a failed Jurassic rift and triple junction in Kenya. Earth and Planetary Science Letters, 81(2-3), 299–311.

Rosendahl, B. R., Kilembe, E., & Kaczmarick, K. (1992). Comparison of the Tanganyika, Malawi, Rukwa and Turkana rift zones from analyses of seismic reflection data. Tectonophysics, 213(1-2), 235–256.

Sarafian, E., Evans, R. L., Abdelsalam, M. G., Atekwana, E., Elsenbeck, J., Jones, A. G., & Chikambwe, E. (2018). Imaging Precambrian lithospheric structure in Zambia using electromagnetic methods. Gondwana Research, 54, 38–49.

Saria, E., Calais, E., Stamps, D. S., Delvaux, D., & Hartnady, C. J. H. (2014). Present-day kinematics of the East African Rift. Journal of Geophysical Research: Solid Earth, 119, 3584–3600.

Schull, T. J. (1988). Rift basins of interior Sudan: Petroleum exploration and discovery. American Association of Petroleum Geologists Bulletin, 72, 1128–1142.

Stamps, D. S., Calais, E., Saria, E., Hartnady, C., Nocquet, J. M., Ebinger, C. J., & Fernandes, R. M. (2008). A kinematic model for the East African Rift. Geophysical Research Letters, 35, L05304.

Stern, R. J. (1994). Arc assembly and continental collision in the Neoproterozoic East African Orogen: Implications for the consolidation of Gondwanaland. Annual Review of Earth and Planetary Sciences, 22(1), 319–351.

Talwani, M., Worzel, J. L., & Landisman, M. (1959). Rapid gravity computations for two-dimensional bodies with application to the Mendocino submarine fracture zone. Journal of Geophysical Research, 64(1), 49–59.

Thybo, H., Maguire, P. K. H., Birt, C., & Perchuc, E. (2000). Seismic reflectivity and magmatic underplating beneath the Kenya Rift. Geophysical Research Letters, 27(2745), 2748.

Tiberi, C., Ebinger, C., Ballu, V., Stuart, G., & Oluma, B. (2005). Inverse models of gravity data from the Red Sea–Aden–East African rift triple junction zone. Geophysical Journal International, 163(2), 775–787.

Tolessa, S., Bonavia, F. F., Solomon, M., Haile-Meskel, A., & Teferra, E. (1991). Structural pattern of Pan-African rocks around Moyale, southern Ethiopia. Precambrian Research, 52(1-2), 179–186.

Tsige, L., & Abdelsalam, M. G. (2005). Neoproterozoic–Early Paleozoic gravitational tectonic collapse in the southern part of the Arabian- Nubian Shield: The Bulbul Belt of southern Ethiopia. Precambrian Research, 138(3-4), 297–318

Vetel, W., & Le Gall, B. (2006). Dynamics of prolonged continental extension in magmatic rifts: The Turkana Rift case study (North Kenya). Geological Society of London Special Publications, 259(1), 209–233.

Vetel, W., Le Gall, B., & Walsh, J. J. (2005). Geometry and growth of an inner rift fault pattern: The Kino Sogo Fault Belt, Turkana Rift (North Kenya). Journal of Structural Geology, 27(12), 2204–2222. https://doi.org/10.1016/j.jsg.2005.07.003

Wienecke, S., Braitenberg, C., & Goetze, H.-J. (2007). A new analytical solution estimating the flexural rigidity in the central Andes. Geophysical Journal International, 169(3), 789–794. https://doi.org/10.1111/j.1365-246X.2007.03396.x

Williamson, P. G., & Savage, R. J. G. (1986). Early rift sedimentation in the Turkana basin, northern Kenya. Geological Society of London Special Publication, 25(1), 267–283. https://doi.org/10.1144/GSL.SP.1986.025.01.22

Winn, R. D. Jr., Steinmetz, J. C., & Kerekgyarto, W. L. (1993). Stratigraphy and rifting history of the Mesozoic-Cenozoic Anza rift, Kenya. American Association of Petroleum Geologists Bulletin, 77, 1989–2005.

Won, I. J., & Bevis, M. (1987). Computing the gravitational and magnetic anomalies due to a polygon: Algorithms and Fortran subroutines. Geophysics, 52(2), 232–238. https://doi.org/10.1190/1.1442298

Worku, H., & Schandelmeier, H. (1996). Tectonic evolution of the Neoproterozoic Adola Belt of southern Ethiopia: Evidence for a Wilson Cycle process and implications for oblique plate collision. Precambrian Research, 77(3-4), 179–210. https://doi.org/10.1016/0301-9268(95)00054-2

Worku, H., & Yifa, K. (1992). The tectonic evolution of the Precambrian metamorphic rocks of the Adola Belt (southern Ethiopia). Journal of African Earth Sciences, 14(1), 37–55. https://doi.org/10.1016/0899-5362(92)90054-G

Zanettin, B., Visentin, E. J., Bellieni, G., Piccirillo, E. M., & Rita, F. (1983). The volcanics of North Turkana Basin (Kenya): Age, succession and structural evolution. Bulletin du Centre de Recherches Elf Exploration Production, 7, 249–255.

CHAPTER III

SPECTRAL ANALYSIS WITH PIECEWISE REGRESSION APPROACH (SAPRA) OF GRAVITY DATA FOR LITHOSPHERIC STRUCTURE IMAGING: THE LAKE TURKANA RIFT BASIN OF THE EAST AFRICAN RIFT SYSTEM

Abstract II

This work introduces a new quantitative approach involving piecewise regression for the identification of unique data points defining the breaks in slope of linear segments of the two-dimensional (2D) radially-averaged spectrum curves (henceforth spectrum curves) of gravity data. This new approach is referred to as the spectral analysis with piecewise regression approach (SAPRA). Linear segments of the spectrum curves of gravity data represents deeper discontinuities in the Earth interior resulting from density contrast interfaces such as the Moho and the Precambrian crystalline basement. Previous approaches used for the identification of data points representing breaks in slope of linear segments of the spectrum curve have been subjective and this results in considerable inconsistency in the calculation of the depth to the Moho and the Precambrian crystalline basement from the gravity data. SAPRA is performed as a one-step process to identify and isolate the data points defining the linear segment of the spectrum curves that corresponds to the density contrast across the Moho and between the Precambrian crystalline basement and the overlying Neogene – Quaternary rift-fill sediment and the Quaternary volcanic rocks surrounding the rift basin. To test the effectiveness of SAPRA, this work applied this approach to the World Gravity Model 2012 (WGM 2012) to calculate the depth to the Moho and the Precambrian crystalline basement beneath the Lake Turkana rift basin, which represents a segment of the Eastern Branch of the East African Rift System (EARS).

Subsequently, results of the Moho depth from the SAPRA were compared with results from 2D forward modeling of the Bouguer gravity anomalies of the WGM 2012 and results from controlled-source seismic imaging. This work found a possibly better imaging technique of the details of the topography of the Moho beneath the Lake Turkana rift basin using the SAPRA. The SAPRA can be readily applied to the gravity data covering other regions in the World for imaging the Moho, given the global coverage of gravity data such as the WGM 2012.

3.1 Introduction

There has been considerable interest in applying the two-dimensional (2D) radially-averaged power spectral analysis (henceforth called the spectral analysis) to gravity data since the method was introduced in the 1960's (Horton et al., 1964; Bhattacharyya, 1966; Spector and Bhattacharyya, 1966) and subsequently popularized by the groundbreaking paper by Spector and Grant (1970). Although it has been used since the 1960's, the spectral analysis has been increasingly used in gravity data analysis starting the 1990's because of the development of new computer-based approaches of interpretation that are capable of processing large amounts of data in a relatively short time (Ravat et al., 2007; Mickus and Hussein, 2015). The fundamental of the spectral analysis is that it can provide first-order approximation to the depth of density interfaces. These interfaces are related to, among other boundaries, major boundaries within the deeper Earth interior such as the Moho, which represents the boundary between the crust and sub-continental lithospheric mantle (SCLM) (Russo and Speed, 1994).

The spectral analysis normally uses the Fourier integral to transform the gravity data from the space domain into the wavenumber domain. Subsequently, the wavenumber domain data are analyzed to determine their spectral characteristics (Dimitriadis et al., 1987). Commonly, a two-dimensional (2D) Fourier transform is used to convert the data into the frequency domain. However, an one-dimensional (1D) Fourier transform has also been used to determine depth to the Moho from gravity profiles (Dorman and Lewis, 1970; Russo and Speed, 1994). The most

commonly used 2D Fourier transform methods to create a 2D power spectrum of the gravity data is an azimuthally averaged spectrum of a sub-region of the data (Shuey et al., 1977; Blakely, 1988; Tanaka et al., 1999). Subsequently, these 2D radially-averaged power spectrum data are plotted on a log plot of Ln-P vs. wavenumber. This spectrum curve represents the response of gravity field to density variations as a function of depth. In most cases, the spectrum curves are caused by density ensembles represented by changes in its shape that is defined by the change of slope of different linear segments (Spector and Grant, 1970). In general, the segment of the spectrum curve corresponding to the lower wavenumbers is taken to represent deeper density interfaces while the segment of the spectrum curve corresponding to the higher wavenumbers is considered to represent shallower density interfaces. It is possible that the segment of the spectrum curve with the highest wavenumbers represents the shallowest near-surface density interfaces. However, in most cases, this segment has been commonly interpreted as white noise rather than density interface (Tanaka et al., 1999).

A major concern in determining the depths to density interfaces is how to select the linear regression fits in the spectrum curves. This is because the subjectivity in selecting the "best" linear regression fits leads to significant uncertainty in the calculated depth to the causative density interfaces. To reduce and quantify the uncertainty in the selection of the linear regression fit in the calculation of the depth to the Moho and the basment, some studies (Leseane et al., 2015; Emishaw et al., 2017; Fletcher et al., 2018) have adopted an Excel LINEST function-based protocol. The first step in this protocol is the selection of the best three first order polynomial fits for the segments of the spectrum curves that will be used for the calculation of the depth to the Moho. Subsequently, the average of these depths is calculated as well as the standard deviation from the depths to the Lithosphere – Asthenosphere Boundary (LAB) and Moho that were calculated from the three separate first order polynomial fits. Hence, in this approach, the

standard deviation is used as a means of qualifying the uncertainty in the selection of the linear regression fits in the spectrum curves.

Regardless of these efforts, all protocols established for reducing and quantifying the uncertainty in the selection of the linear regression fit of segments of the spectrum curves did not address the fundamental problem of how the breaks in the slope of the linear segments of the spectrum curves are determined in order to establish the individual linear segments. Determining where these breaks occur within the spectrum curves is essential for an unbiased selection of the linear regression fit for the data points that define individual linear segments of the spectrum curves. In some cases, the breaks in the slope of the linear segments of the spectrum curves are sharp, hence can be easily manually identified. However, in most cases, these breaks might not be sharp, hence cannot be unbiasedly manually identified. Hence, a more robust quantitative method in identifying these breaks in the slope is needed. The need for such quantitative method has been appreciated since the early 1970's, as Treital et al. (1971) pointed that the depth estimates from energy density function decay needed a robust statistical analysis.

To address the problem of identifying the breaks in slope of the linear segments of the spectrum curves, this work introduces a piecewise regression method to identify unique data points that define the breaks in slope between the linear segments of the spectrum curve. This will be referred to as the spectral analysis with piecewise regression approach (SAPRA). Subsequently, results of the depth to the Moho obtained for the Lake Turkana rift basin (which represents part of the Eastern Branch of the East African Rift System (EARS)) (Figures 1 and 2) from the SAPRA of the World Gravity Model 2012 (WGM 2012) will be presented. In addition, these results will be compared with results from 2D forward modeling of the same data (Emishaw and Abdelsalam, 2019) and results from controlled-source seismic data (Keller et al., 1994).

3.2 The Lake Turkana Rift Basin

The geology and tectonic setting of the N-trending Lake Turkana rift basin have been recently summarized in Emishaw and Abdelsalam (2019). This rift basin represents a segment of the Neogene – Quaternary Turkana rifted zone, which dominates the Turkana depression. This depression extends in a NW-SE direction between the Ethiopia – Yemen plateau in the northeast and the East Africa plateau to the southwest (Figures 1 and 2; Dunkelman, et al., 1989; Rosendahl et al., 1992; Morley, 1999a; Ebinger et al., 2000; Bonini et al., 2005; Vetel et al., 2005; Vetel and Le Gall, 2006; Brune et al., 2017; Emishaw et al., 2017; Corti et al., 2019; Emishaw and Abdelsalam, 2019). From controlled source seismic data, Dunkelman et al. (1989) described the Lake Turkana rift basin as a series of N-trending half grabens whose border faults alternate between the east and west side of the rift basin. Further, Dunkelman et al. (1989) found that these half grabens deepen northward to reach ~4 km in depth in the northern part of the Lake Turkana rift basin.

The Lake Turkana rift basin is filled with Neogene – Quaternary coarse clastic sediments that are sourced from the nearby mafic volcanic rocks; presently the Lake Turkana is dominated by sublittoral to profundal, authigenic low-Mg micrite and ostracodal sands - and silts (Cohen, 1989). The rift basin is surrounded by Quaternary volcanic rocks, dominantly basaltic in composition (Figure 3). Both the sediment filling to rift basin and the Quaternary volcanic rocks surrounding it are unconformably overlie Precambrian crystalline basement representing part of the East African Orogen (Stern, 1994).

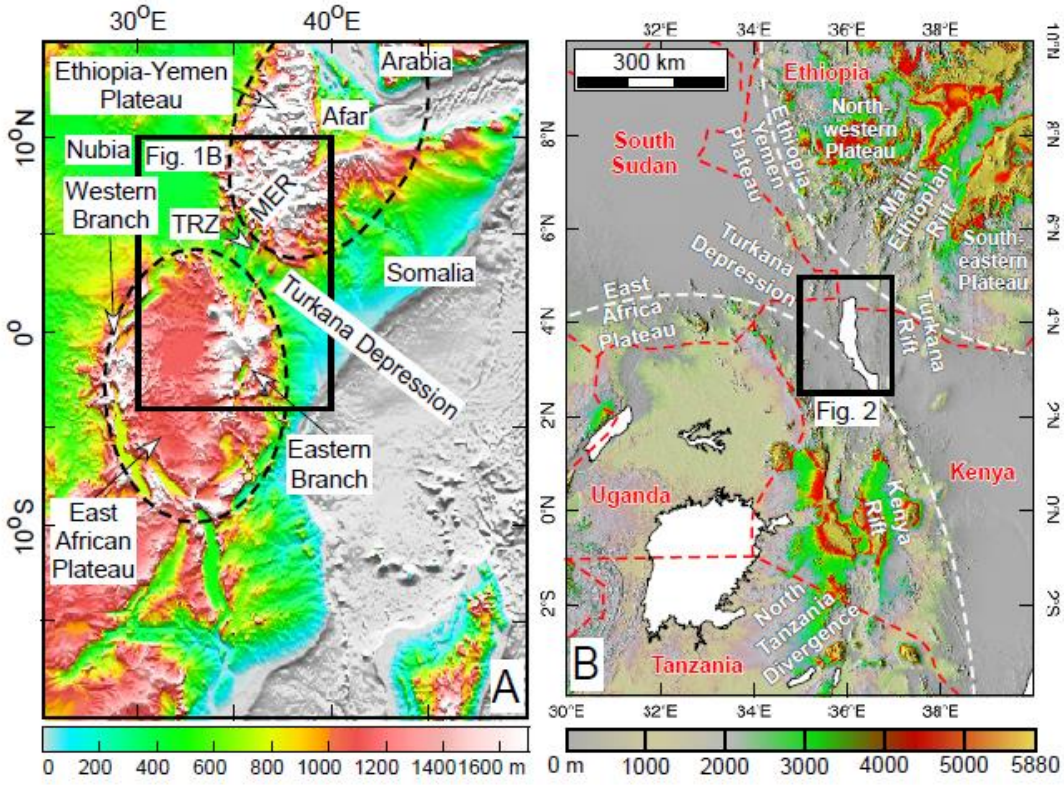

Figure 3.1: (A) Earth topography 1 arc min (ETOPO1) digital elevation model (DEM) showing the East African Rift System (EARS). TRZ = Turkana rifted zone. (B) Shuttle Radar Topography Mission (SRTM) DEM showing the Lake Turkana rift basin within the Turkana depression between the Ethiopia – Yemen plateau in the northeast and the East Africa plateau to the southwest.

The development of the low relief of the Turkana depression is attributed to the intersection between the N- to NE-trending Eastern Brach of the EARS and the NW-trending Jurassic – early Paleogene rifts of South Sudan and Kenya. It has been proposed that this intersection resulted in significant thinning of the crust beneath the depression and this has led to the lowering of the elevation through isostatic adjustment (Benoit et al., 2006). Crustal and lithospheric thinning beneath the Turkana depression is documented from various geophysical studies. The Kenya Rift International Seismic Project (KRISP) Working Group (1991) collected a controlled source seismic data along a N-S profile extending along the strike of the Lake Turkana rift basin, on the western side of the lake itself.

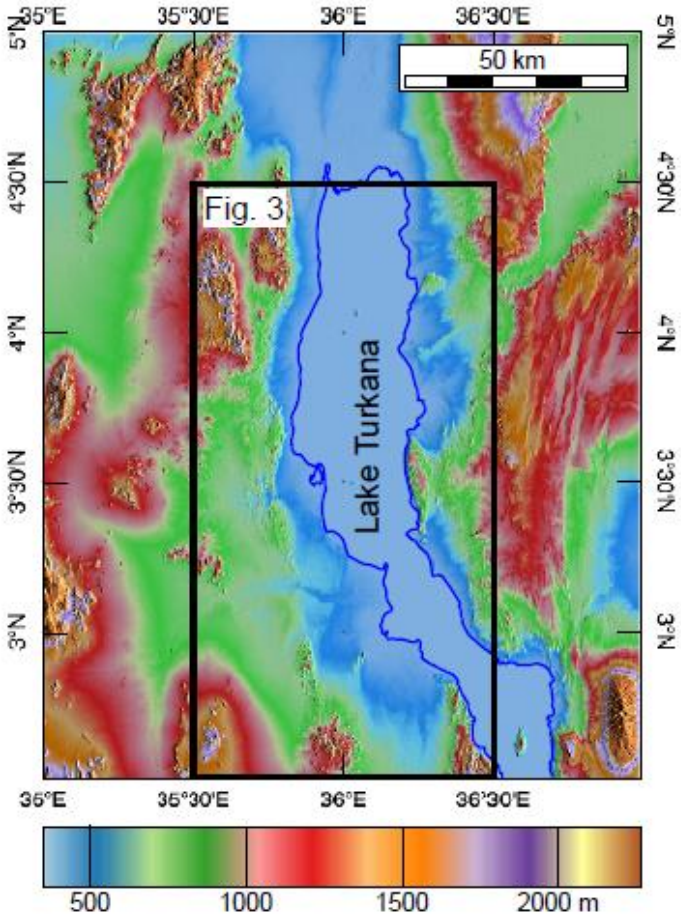

Figure 3.2: Shuttle Radar Topography Mission (SRTM) Digital Elevation Model (DEM) of the Lake Turkana rift basin.

Keller et al. (1994), Mechie et al. (1994) and Prodehl et al. (1994) analyzed these data to show that the crust thins from ~35 km thickness beneath the northern part of the East Africa plateau to ~20 km beneath the central part of the Lake Turkana rift basin. Benoit et al. (2006) used Rayleigh wave dispersion analysis to obtain crustal thickness ranging between ~26 km and ~30 km beneath the Turkana depression. Using the Lithoflex inversion algorithm (Braitenberg et al., 2002) of the WGM 2012, Emishaw and Abdelsalam (2019) showed the presence of NW-SE trending zone of crustal thinning beneath the Turkana depression where the crust thickness is between 23 and 28 km. Emishaw and Abdelsalam (2019) also documented thinning of the crust beneath the Turkana depression using 2D forward gravity modeling. Additionally, Emishaw and Abdelsalam (2019)

used 2D forward gravity modeling suggesting the presence of thinner lithosphere beneath the Turkana depression.

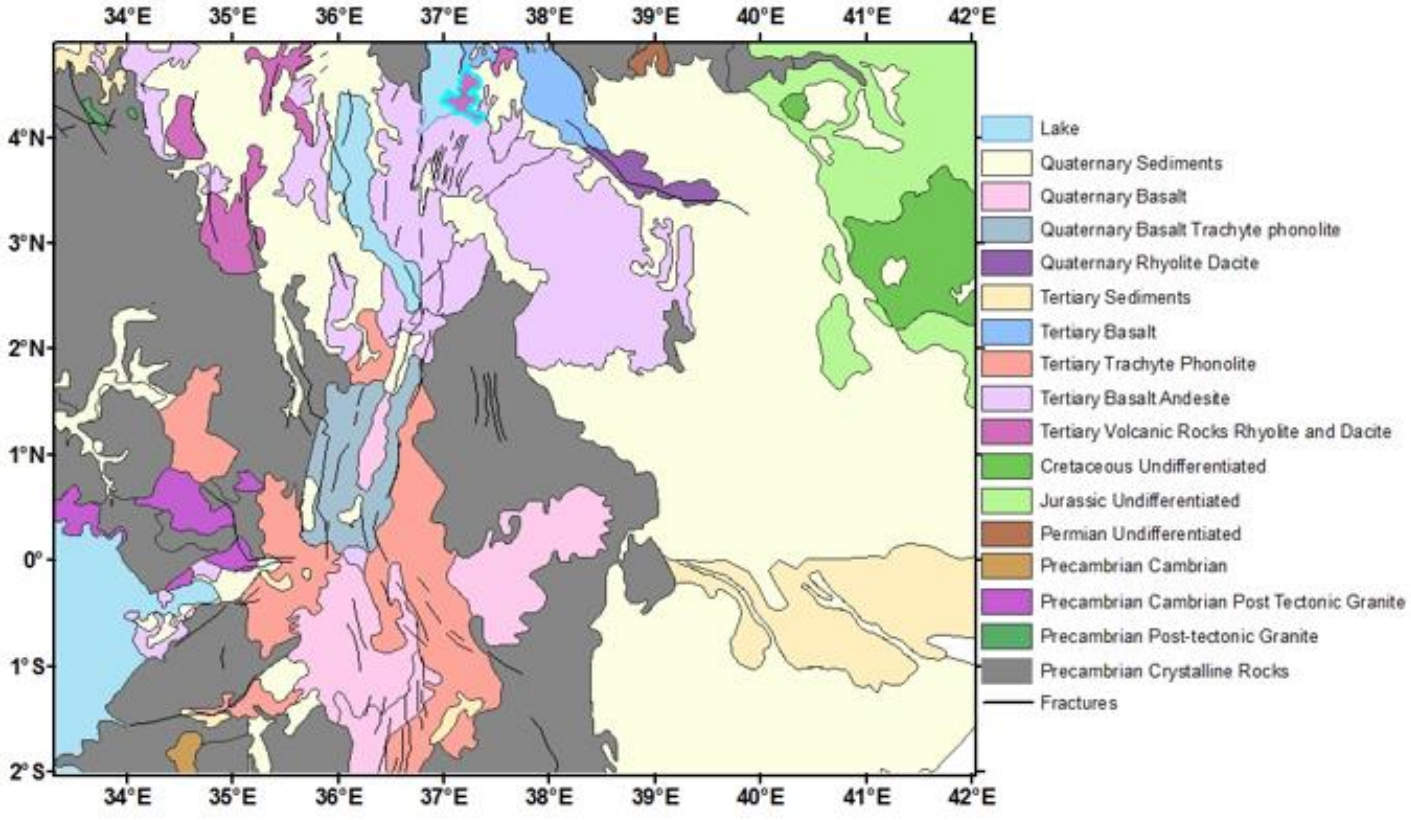

Figure 3.3: Geological map of the Turkana Depression. Choubert and Faure-Muret (1990).

3.3 Fourier Spectral Analysis of Gravity Data

Using Fourier integrals to analyze gravity data is possible because the Earth acts as a low-pass filter with respect to density anomalies, allowing these integral to be analyzed as waveforms although they do not inherently exhibit any wave characteristics (Odegard and Berg, 1975). Initial attempts to apply Fourier spectral analysis to gravity data were made in the late 1950's (Serson and Hannaford 1957) and later in the early 1960's, where updated statistical methods were developed for the analysis of aeromagnetic data (Alldregde et al., 1963; Horton et al., 1964). Subsequent work gave rise to the expression of simple 2D and 3D geometries that

cause gravity anomalies in the frequency domain (Bhattacharyya, 1966; Spector and Bhattacharyya, 1966; Cassano and Rocca, 1975; Regan and Hinze, 1977; Chowadary, 1978). These frequency domain expressions provide the basis for determining the depth to density interfaces.

The Fourier integral transform of the gravity field has been summarized by Sadek et al. (1984) and has the following general expression for a function that varies continuously along a profile of observations:

$$\Delta\bar{T}(\mathrm{f_y}) = \int_{-\infty}^{\infty} \Delta T(y) \cdot e^{-i2\pi(\mathrm{fy})y}\, dy \qquad (1)$$

where $\Delta\bar{T}(\mathrm{fy})$ is the Fourier transform of $\Delta T(y)$, fy is the spatial frequency in the direction of the y-axis (cycles/unit length), $\Delta T(y)$ is the gravity field along the y-axis, and y is the linear distance along the profile.

Equation 1 assumes that the function is periodic outside the given range of y. If Ly is considered as the length of the profile of the function in the interval –Ly/2 with the defined endpoints and if the gravity field is multiplied by a weighting function (e.g., "Cosine bell" function) to eliminate the endpoint discontinuities, the new expression for the Fourier transform becomes:

$$\Delta\bar{T}(\mathrm{fy}) = \int_{-\frac{Ly}{2}}^{\frac{Ly}{2}} \Delta T(y) \cdot G(y) \cdot e^{-i2\pi(\mathrm{fy})y}\, dy \qquad (2)$$

where Ly is the length of the profile in the interval –Ly/2, and G(y) = ½ (1 + cos (2πy/Ly)).

Defining the wavenumber V as V = 2πfy and integrating it using Euler's theorem, Equation 2 can be simplified to:

$$\Delta\bar{T}(v) = \int_{-\frac{Ly}{2}}^{\frac{Ly}{2}} \Delta T(y) \cdot G(y) \cdot \cos(vy)\, dy - i \int_{-\frac{Ly}{2}}^{\frac{Ly}{2}} \Delta T(y) \cdot G(y) \cdot \sin(vy) dy \quad (3)$$

By using the Filon's solutions for the integration of the trigonometric function (3), the natural Napierian logarithmic values of the energy density function E(fy) can be obtained by multiplying $\Delta\bar{T}(fy)$ by its complex conjugate, $\Delta\bar{T} * (fy)$:

$$E(fy) = \Delta\bar{T}(\text{fy}) \cdot \Delta\bar{T} * (\text{fy}) \quad (4)$$

The general expression of this energy density function (4) in terms of radial wavenumbers and the azimuth of the radial wavenumber is given by:

$$\text{E(r, } \theta) = \text{Gdensity} \cdot \text{H(h,r)} \cdot \text{S(ai,r, } \theta) \cdot \text{C(bi,r)} \quad (5)$$

where H is the depth factor, S is the horizontal size (width) factor, C is the vertical size (thickness of the depth extent) factor, r is the radial wavenumber, θ is the azimuth of radial wavenumber, h is the depth to the top of the ideal model source, ai are the parameters related to the horizontal dimensions of the source, and bi are the parameters related to the vertical depth extent of the source.

From Equation 5, only the factors H, S, and C affect the geometry of the radial spectrum. In addition, with increasing the wavenumbers, the decay of the spectral energy is invariably dominated by the depth factor (Sadek et al., 1984). These factors simplify the above expression for the depth factor for all simple source geometries to be:

$$\text{H(h, r)} = e^{-2hr} \quad (6)$$

where H(h, r) is the depth to the top of the density interface and r is the wavenumber.

The representation of Equation 6 as a linear equation can be expressed as:

$$\text{Ln } H(h, r) = -2hr \quad (7)$$

Where h is the slope that is used to estimate the depth to a given density interface.

3.4 Spectral Analysis with Piecewise Regression Approach (SAPRA) For Determining the Depth to the Moho And Precambrian Crystalline Basement

Piecewise regression is useful for the identification of the breaks in slope of the linear segments of the spectrum curves because it has the ability to optimize the data point at which the slope breaks (McZgee et al., 1970). Piecewise regression, which is also known as segmented regression or broken-stick regression, is a typical regression analysis that is used to partition independent variable into intervals and each of these intervals are represented by separate best fit regression line (McZgee et al., 1970; Tome and Mirande, 2004). This makes piecewise regression an ideal technique to identify the optimized breaks in slope of the linear segments of the spectrum curves as functions of a natural logarithm.

The WGM 2012, which has a spatial resolution of 9 km (Balmino et al., 2012), are used to demonstrate the effectiveness of the SAPRA in the identification of unique data points that define breaks in slope of linear segments of the spectrum curves. Hence, these results give more accurate estimations of the depth to the Moho and the Precambrian crystalline basement. The Bouguer gravity anomalies of the WGM 2012 (Figure 4) were obtained for the Lake Turkana rift basin from the International Center for Global Earth Model (ICGEM). The spectrum curve derived for one of the fifteen 1°X1° (~110 km X ~110 km) subset of this dataset that is centered around longitude 36°E and latitude 3°30′S (Figure 5) will be used to demonstrate the detailed steps that are needed to be followed to perform the SAPRA for the calculation of the depth to the Moho and Precambrian crystalline basement. Subsequently, the Bouguer gravity anomalies of the

WGM 2012 will be analyzed using the SAPRA to generate the depth to the Moho and the Precambrian crystalline basement maps for the Lake Turkana rift basin.

The SAPRA requires determining the value "x" at which the slope of the linear segments of the spectrum curve changes. If there is only one data point defining the break in slope of the linear segments of the spectrum curve, say at x = c, then the model equation can be represented by:

$y = a_1 + b_1x$ for $x <= c$ (8)

$y = a_2 + b_2x$ for $x > c$ (9)

Given that both equations are continuous at "c", then they can be rewritten as:

$a_1 + b_1c = a_2 + b_2c$ (10)

From Equation 10, parameter a_2 can be expressed as:

$a_2 = a_1 + c*(b_1 – b_2)$ (11)

By combining Equations 8, 9 and 10, the results of the SAPRA model become:

$y = a1 + b1x$ for $x <= c$ (12)

$y = \{a1 + c*(b1 – b2)\} + b2x$ for $x > c$ (13)

Equation 13 represents a slope break point between two slopes. However, SAPRA needs at least three slope break points to isolate at least four segmented slopes that represent deeper and shallower density ensembles. Therefore, SEGMENTED, an R software package, is implemented to best identify the break points in one run (Muggeo, 2015.); SEGMENTED significantly improves the step-wise manual implementation of multiple piecewise regression slopes by solving all the slope equations simultaneously.

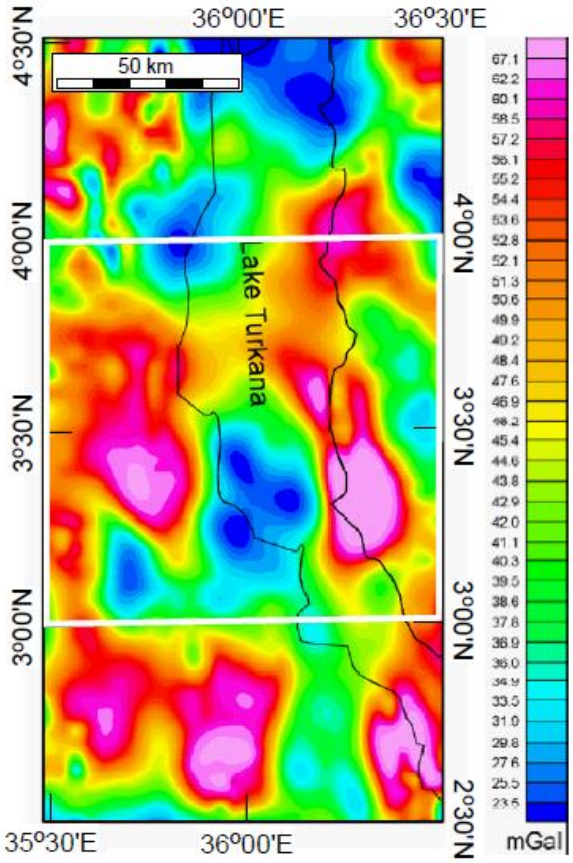

Figure 3.4: Bouguer gravity anomaly map of the World Gravity Model 2012 (WGM 2012) of the Lake Turkana rift basin. The white box represents the 1°x1° sub-window used to compute the two-dimensional (2D) radially-averaged power spectrum curve shown in Figure 5.

This feature of the SEGMENTED makes the package powerful to segment the spectrum curves into multiple density ensembles.

The use of Fourier integrals to analyze gravity data has been possible due to the low-pass filter characteristic of Earth with respect to density anomalies (Figure 5; Odegard and Berg, 1975). However, Figure 5 shows that the logarithmic energy spectrum defined by Ln[P] does not decay out smoothly as it has some undulatory nature. In general, in the frequency domain, the energy spectrum exhibits high frequency components when the anomaly is continued to the proximity of the source. Therefore, the near-surface source gives shallower power spectrum while the deep-surface source gives steeper power spectrum (Pal, 1978).

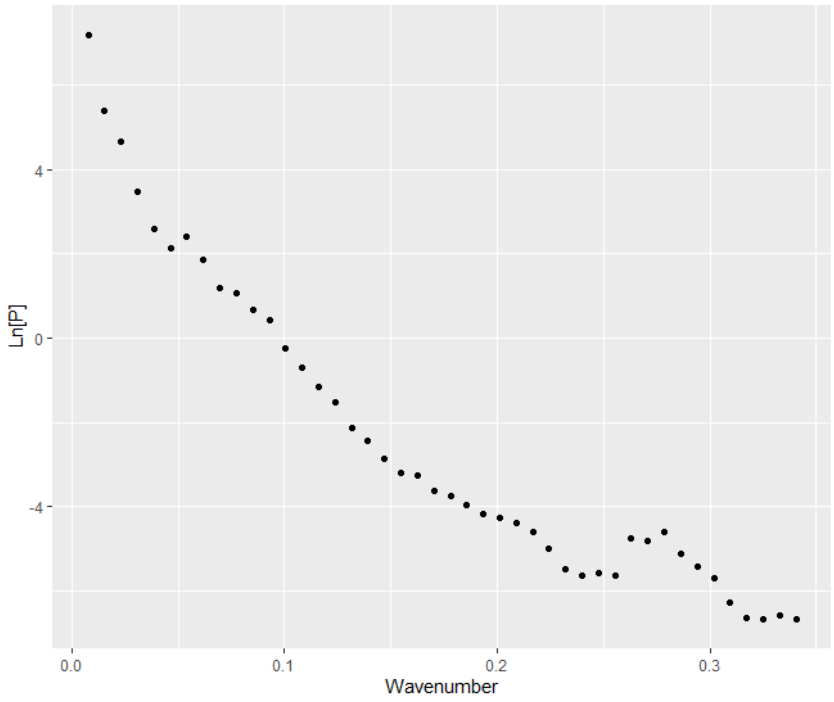

Figure 3.5: A typical two-dimensional (2D) radially-averaged power spectrum curve. The spectrum curve is computed from the 1°x1° sub-widow of the Bouguer gravity anomalies of the World Gravity Model 2012 (WGM 2012) covering portion of the Lake Turkana rift basin and centered around 36°E and 3°30′S. See Figure 4 for the location of the sub-window.

This general principle, however, is not always encountered in real gravity data, and there are multiple occasions in which anomalously steeper and/or positive slopes could be observed, which represents the near surface sources in the spectrum curves. Hence, in order to maintain

consistency in the implementation of SAPRA, 2nd degree polynomial fit is applied to the energy spectrum curve such that the logarithmic energy spectrum, plotted against wavenumber, decays out smoothly. This change to the logarithmic energy spectrum (Figures 5A and B), no doubt, modifies the original anomalies. With this trade-off, however, SAPRA becomes more consistent, and the pattern of the energy spectrum curves becomes predictable.

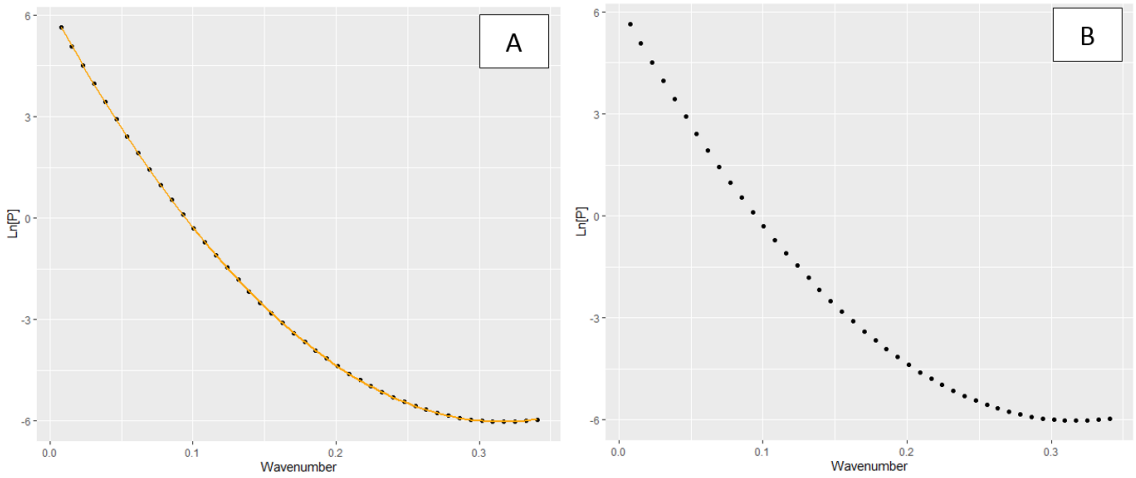

Figure 3.6: The smoothed two-dimensional (2D) radially-averaged power spectrum curve shown in Figure 5. The curve is smoothed by 2nd degree polynomial regression. Figure 6A is a subset of Figure 1 and shows the 2nd degree polynomial regression fit that is calculated from the data points in Figure 5. Figure 6B shows the extracted values from the 2nd degree polynomial regression fit of the power spectrum calculated from the 2nd degree polynomial regression fit equation.

This allows a successful implantation of SAPRA to the smoothed power spectrum to estimate the depth to the Moho and the Precambrian crystalline basement (Figure 7). This implementation generally considers three break points in the slope of the spectrum curve that separate four segments corresponding with four frequency components. Fletcher et al. (2018) showed that the steepest segment of the spectrum curve that corresponds to the lowest wavenumber values can be taken to represent the LAB. On the other hand, Spector and Grant (1970) considered the shallowest segment of the curve with high frequency components to be depth to the near-surface sources. Thus, the frequency component between the lowest and highest wavenumber values

constitutes a frequency component coming from the top of the sub-crustal mantle or the Moho (Pal, 1978; Tselentis et al., 1988; Emishaw et al., 2017).

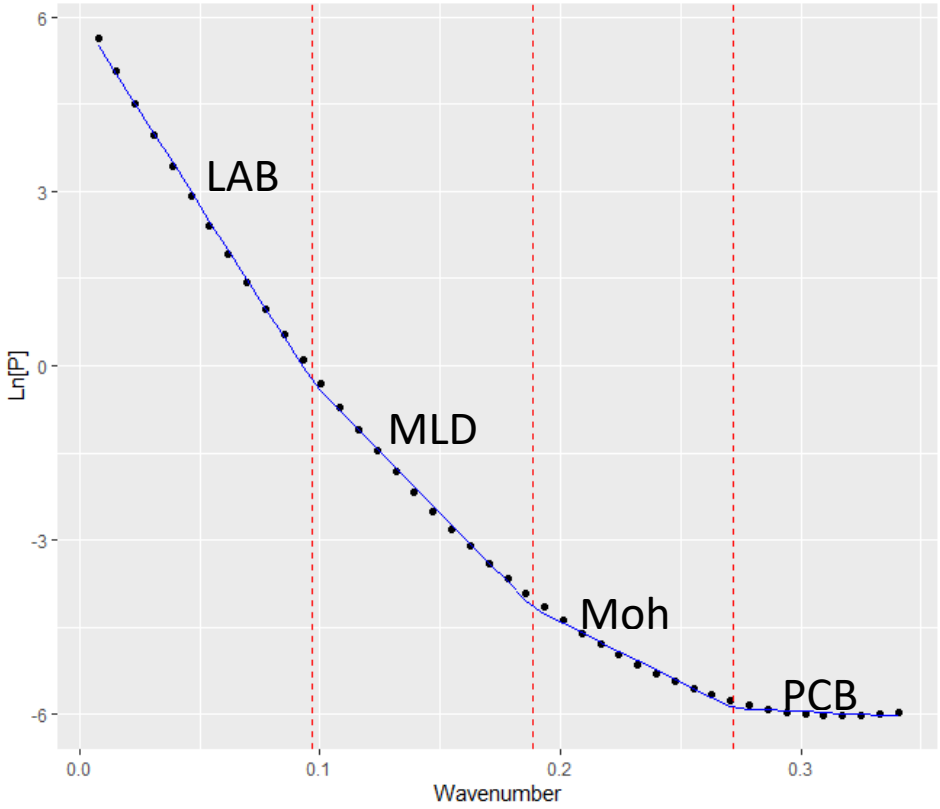

Figure 3.7: Identification of linear segments in the two-dimensional radially-averaged power spectrum curve shown in Figure 6 using the Spectral Analysis with Piecewise Regression Approach (SAPRA). The analysis results in the identification of four linear segment. The segment corresponding to the lowest wavenumber values represents density contrast across the lithosphere – asthenosphere boundary. The segment corresponding to the second lowest wavenumber values represents density contrast across the mid-lithospheric discontinuity (MLD). The segment corresponding to the second highest wavenumber value represents density contrast across the Moho. The segment corresponding to the highest wavenumber values represents density contrast between the Precambrian crystalline basement and the overlying Neogene – Quaternary sediment that fill the Lake Turkana rift basin and Quaternary volcanic rocks that surrounds the rift basin.

However, the segment of the spectral curve between the steepest and the shallowest might not be entirely sourced from the density contrast across the Moho. It is possible that this middle segment of the spectrum curve is due to combined density contrast across the Moho as well as the as well as mid-lithospheric discontinuity (MLD). In this case, the estimation of the

depth to the Moho using the three segments that have been traditionally identified in the spectrum curve, will give an unrealistic depth to the Moho, which is usually deeper compared to those obtained by other geophysical method such as controlled source and passive seismic studies. Thus, another advantage of SAPRA over the traditional spectral analysis method is its ability to deconvolute the central part of the spectrum curve into two segments (Figure 7). This will allow separating the segment of the curve that is related to the MLD from that is related to the Moho, hence allowing more reliable estimate of the Moho. In so doing, the power spectrum curve tends to have four, instead of three slopes (Figure 7).

3.5 Depth to the Moho and Precambrian Crystalline Basement beneath the Lake Turkana Rift Basin

To calculate the depth to the Moho and the Precambrian crystalline basement, the SAPRA was applied to fifteen 1^{o}x1^{o} sub-windows of the Bouguer gravity anomalies of WGM-2012, covering the Lake Turkana rift basin (Figure 2). These 1^{o}x1^{o} sub-windows were overlapping by 50% in the north-south and east-west directions.

The SAPRA of the Bouguer gravity anomalies of the WGM 2020 shows that the Moho depth beneath the Lake Turkana rift basin ranges between 20 and 32 km. The shallowest Moho depth of 20 km is found immediately on the central part of the rift basin (Figure 8A). This shallow Moho becomes progressively thicker towards the north, reaching 32 km in the northern edge of the Lake Turkana rift basin (Figure 8A).

The SAPRA basement map (Figure 8B) shows that the depth to Precambrian crystalline basement progressively increases in the north direction. Based on the SAPRA result, the depth to the Precambrian crystalline basement beneath the Lake Turkana rift basin and the surrounding Quaternary volcanic rocks range between 0.2 km to 1.7 km. The depth to the Precambrian crystalline basement obtained through the SAPRA is consistent with sediment thickness estimates

obtained for the sediment filling the Lake Turkana rift basin (Dunkelman et al., 1989). However, (Dunkelman et al., 1989) reported that the sediment thickness deepens northward to reach ~ 4 km in the northern part of the Lake Turkana rift basin. This estimate is greater than the sediment thickness estimate of 1.7 km obtained by the SAPRA. The inconsistency might have originated from the presence of greater density contrast within the stratigraphic column itself, which is reported to have clastic sediments sourced from mafic volcanic rocks (Cohen, 1989) that display lower density contrast when compared with the Precambrian crystalline basement, which is made-up of dominantly granitic gneiss.

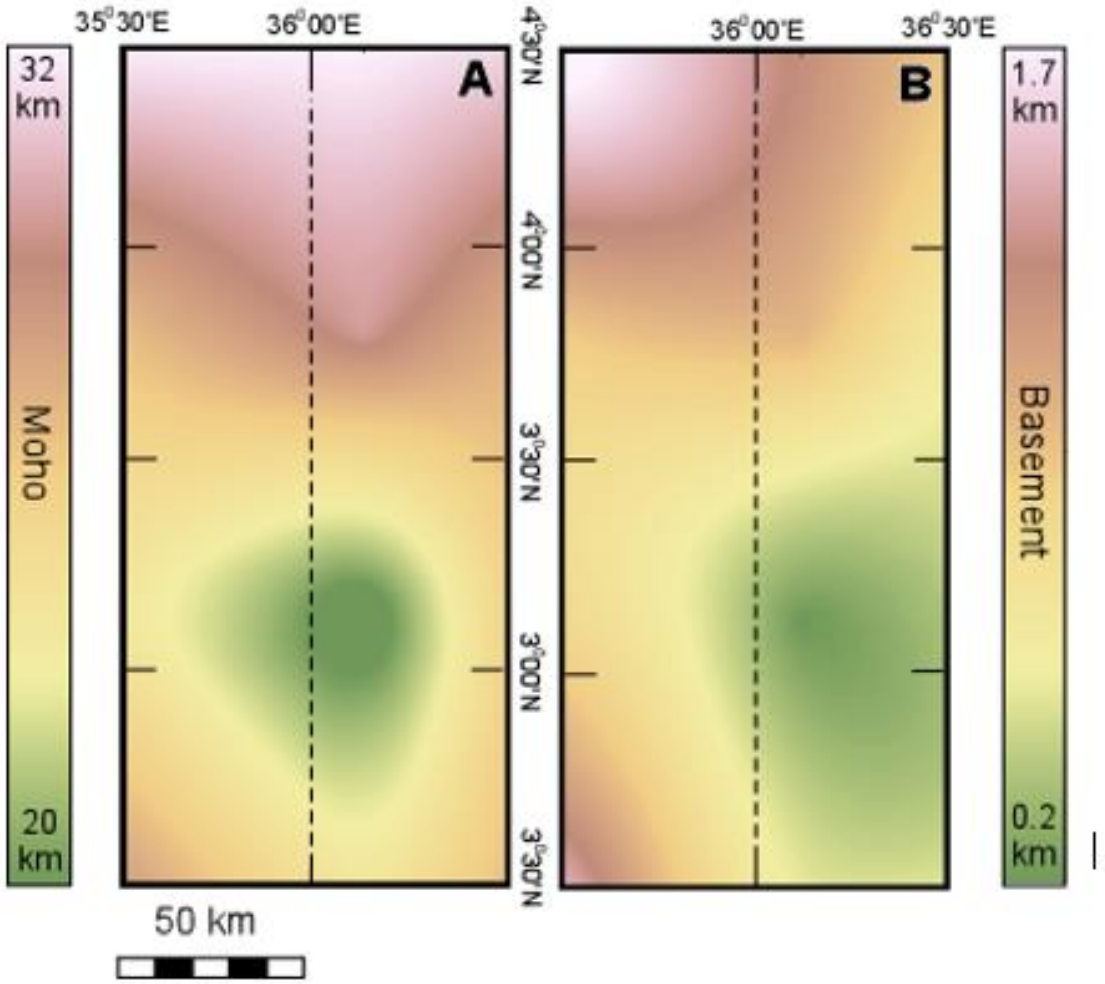

Figure 3.8: Depth to the Moho (A) and the Precambrian crystalline basement (B) beneath the Lake Turkana rift basin obtained from the Spectral Analysis with Piecewise Regression Approach (SAPRA) of the Bouguer gravity anomalies of the World Gravity Model 2012 (WGM 2012).

3.6 Discussion

Figure 9 shows comparison between the depth to the Moho beneath the Lake Turkana rift basin obtained by applying the SAPRA to the Bouguer gravity anomalies of the WGM 2012, the depth to the Moho obtained from controlled source seismic imaging (Keller et al., 1994), and Moho depth results obtained from 2D forward modeling of the same gravity data (Emishaw and Abdelsalam, 2019). Emishaw and Abdelsalam (2019) used the Bouguer gravity anomalies of the

WGM 2012 to construct 2D forward models showing the depth to the Moho beneath the rift basin extending along longitude 36°E from 2°S to 5° N. Keller et al. (1994) controlled-source seismic imaging section stretched in a north-south direction close to longitude 36°E from around 1°S to 3°N with the northern part of this profile extending within the southern half of the Lake Turkana rift basin. The seismic section shows that the Moho depth beneath the southern part of the Lake Turkana rift basin to be ~ 20 km. Additionally, the 2D forward modeling of Bouguer gravity anomalies of the WGM 2012 of Emishaw and Abdelsalam (2019) shows that the depth to the Moho beneath the entire Lake Turkana basin to be relatively flat and slightly fluctuating around ~ 23 km (Figure 9). However, the SAPRA results show the Moho depth beneath the rift basin to have more topography in which the Moho beneath the central part of the rift basin have an elevated Moho of ~ 20 km and that this elevated Moho is flanked in the north by relatively deeper Moho reaching ~ 32 km. The slanting down of the Moho topography beneath the northern limit of the Lake Turkana rift basin is also observed in the Moho map obtained from the 2D gravity inversion of the Bouguer gravity anomalies by Lihoflex (Emishaw and Abdelsalam, 2019).

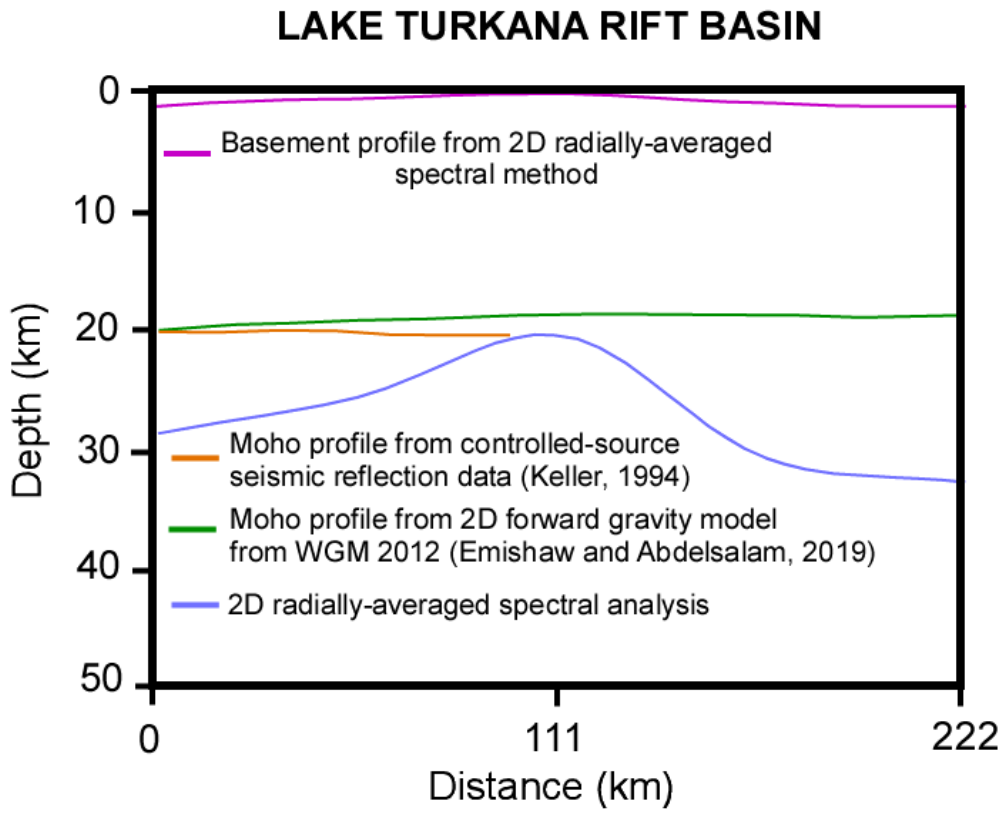

Figure 3.9: Comparison of results of the depth to the Moho obtained from the Spectral Analysis with Piecewise Regression Approach (SAPRA) of the Bouguer gravity anomalies of the World Gravity Model 2012 (WGM 2012), and results obtained from two-dimensional (2D) forward modelling of the same gravity data (Emishaw and Abdelsalam, 2019). The Moho depths results from the SAPRA are also compared with those obtained from control-source seismic imaging (Keller et al., 1994). The profile extends along longitude 36°E and between latitudes 2°30'N and 4°30'N. See Figure 8A and B for location of the profile. The green profile represents results obtained from 2D forward gravity model; the orange profile represents results obtained from the controlled source seismic reflection data; and the blue profile represents results obtained from the SAPRA.

3.7 CONCLUSION

The SAPRA was introduced in this work as a new quantitative approach for the spectral analysis of the gravity data to obtain estimates on the depth to the Moho and shallower layering in the crust. The Bouguer gravity anomalies of the WGM 2012 was used in the study and the Lake Turkana rift basin was used as a test site. The SAPRA was implanted to identify unique data points defining the breaks in the slope of the linear segments of the spectrum curves extracted from the Bouguer gravity anomalies of the WGM 2012. Additionally, the SAPRA was used to deconvolute the central segment of the spectral curves, which was traditionally considered as a single segment representing the density contrast across the Moho. The analysis allowed the identification of linear segments in the spectrum curves that are associated with density contrast across the Moho and between the Precambrian crystalline basement and the overlying Neogene – Quaternary rift-fill sediment and Quaternary volcanic rocks.. The SAPRA is an improvement over previous approaches in identifying the data points representing breaks in slope of linear segments of the spectrum curves. The SAPRA was applied to calculate the depth to the Moho and the Precambrian crystalline basement beneath the Lake Turkana rift basin using the WGM 2012 Bouguer gravity anomalies. Discrepancies are found between the Moho depth estimates from the SAPRA and Moho depth results obtained from previous 2D forward modeling of the same gravity data as well as results from controlled-source seismic imaging. The previous studies imaged the Moho beneath the Lake Turkana rift basin and relatively flat, whereas the SAPRA imaging showed more topography in the Moho beneath the rift basin. This can be attributed to better imaging of the details of the topography of the Moho using the SAPRA because of accurate identification of data points defining breaks in slope of the linear segment of the spectrum curves.

3.8 References

Alldredge, L. R., Van Voorhis, G. D., & Davis, T. M. (1963). A magnetic profile around the world. *Journal of Geophysical Research, 68*(12), 3679-3692.

Balmino, G., Vales, N., Bonvalot, S., & Briais, A. (2012). Spherical harmonic modelling to ultra-high degree of Bouguer and isostatic anomalies. *Journal of Geodesy, 86*(7), 499-520.

Bhattacharyya, B. K. (1966). Continuous spectrum of the total-magnetic-field anomaly due to a rectangular prismatic body. *Geophysics 31(1)*, 97-121.

Blakely, R. J. (1988). Curie temperature isotherm analysis and tectonic implications of aeromagnetic data from Nevada. Journal of Geophysical Research: Solid Earth, 93(B10), 11817-11832.

Bonini, M., Corti, G., Innocenti, F., Manetti, P., Mazzarini, F., Abebe, T., & Pecskay, Z. (2005). Evolution of the Main Ethiopian Rift in the frame of Afar and Kenya rifts propagation. *Tectonics, 24*(1).

Brune, S., Corti, G., & Ranalli, G. (2017). Controls of inherited lithospheric heterogeneity on rift linkage: Numerical and analog models of interaction between the Kenyan and Ethiopian rifts across the Turkana depression. *Tectonics, 36*(9), 1767-1786.

Cassano, E., & Rocca, F. (1975). Interpretation of magnetic anomalies using spectral estimation techniques. *Geophysical prospecting*, *23*(4), 663-681.

Chowdary, M. R. (1978). Spectral analysis of total magnetic anomalies of step model. *Geophysics*, *43*(3), 634-636.

Choubert, A., & Faure-Muret, A. (1990). International geological map of Africa: Commission of the Geological Map of the World.

Cohen, A. S. (1989). Facies relationships and sedimentation in large rift lakes and implications for hydrocarbon exploration: examples from Lakes Turkana and Tanganyika. *Palaeogeography, Palaeoclimatology, Palaeoecology*, *70*(1-3), 65-80.

Corti, G., Cioni, R., Franceschini, Z., Sani, F., Scaillet, S., Molin, P., Isola, I., Mazzarini, F., Brune, S., Keir, D., Erbello, A., Muluneh, A., Illsley-Kemp, F., & Glerum, A. (2019). Aborted propagation of the Ethiopian rift caused by linkage with the Kenyan rift. *Nature Communication*. https://doi.org/10.1038/s41467-019-09335-2.

Dimitriadis, K., Tselentis, G.A., & Thanassoulas, K. (1987). A BASIC program for 2-D spectral analysis of gravity data and source-depth estimation. *Computers & Geosciences, 13(5)*, 549-560.

Dorman, L.M., Lewis, B.T., 1970. Experimental isostasy: 1. Theory of the determination of the Earth's isostatic response to a concentrated load. *Journal of Geophysical Research 75*, 3357-3365.

Dunkelman, T. J., Rosendahl, B. R., & Karson, J. A. (1989). Structure and stratigraphy of the Turkana rift from seismic reflection data. *Journal of African Earth Sciences (and the Middle East)*, *8*(2-4), 489-510.

Ebinger, C. J., Yemane, T., Harding, D. J., Tesfaye, S., Kelley, S., & Rex, D. C. (2000). Rift deflection, migration, and propagation: Linkage of the Ethiopian and Eastern rifts, Africa. *Geological Society of America Bulletin*, *112*(2), 163-176.

Emishaw, L., & Abdelsalam, M. G. (2019). Development of late Jurassic–early Paleogene and Neogene-Quaternary rifts within the Turkana Depression, East Africa from Satellite Gravity Data. *Tectonics*. https://doi.org/10.1029/2018TC005389.

Emishaw, L., Laó-Dávila, D.A., Abdelsalam, M.G., Atekwana, E.A., & Gao, S.S., 2017. Evolution of the broadly rifted zone in southern Ethiopia through gravitational collapse and extension of dynamic topography. *Tectonophysics 699*, 213-226.

Fletcher, A.W., Abdelsalam, M.G., Emishaw, L., Atekwana, E.A., Laó-Dávila, D.A., & Ismail, A., 2018. Lithospheric controls on the rifting of the Tanzanian craton at the Eyasi Basin, eastern branch of the East African Rift System. *Tectonics 37*(9), 2818-2832.

Horton, C.W., Hempkins, W.B., Hoffman, A.A. J. (1964). A statistical analysis of some aeromagnetic maps from the northwestern Canadian Shield. *Geophysics 29*, 582-601.

Keller, G. R., Mechie, J., Braile, L. W., Mooney, W. D., & Prodehl, C. (1994). Seismic structure of the uppermost mantle beneath the Kenya rift. *Tectonophysics*, *236*(1-4), 201-216.

Leseane, K., Atekwana, E.A., Mickus, K.L., Abdelsalam, M.G., Shemang, E.M., & Atekwana, E.A. (2015). Thermal perturbations beneath the incipient Okavango Rift Zone, northwest Botswana. *Journal of Geophysical Research* 120, 1210-1228.

Mackenzie, G., Thybo, H., Maguire, P., 2005. Crustal velocity structure across the Main Ethiopian Rift: results from two-dimensional wide-angle seismic modelling. Geophysical Journal International 162, 994-1006.

McZgee, V. E., & Carleton, W. T. (1970). Piecewise regression. *Journal of the American Statistical Association*, *65*(331), 1109-1124.

Mechie, J., Keller, G. R., Prodehl, C., Gaciri, S., Braile, L. W., Mooney, W. D., & Sandmeier, K. J. (1994). Crustal structure beneath the Kenya Rift from axial profile data. *Tectonophysics*, *236*(1-4), 179-200.

Mickus, K., & Hussein, M. (2016). Curie depth analysis of the Salton Sea region, southern California. *Pure and Applied Geophysics*, *173*(2), 537-554.

Morley, C.K., Wescott, W.A., Stone, D.M., Harper, R.M., Wigger, S.T., Day, R.A., & Karanja, F.M. (1999). Geology and geophysics of the Western Turkana basins. *American Association of Petroleum Geologists Studies in Geology 44*, 19-54.

Muggeo, V. M. R. (2015). Regression models with breakpoints/changepoints estimation. *R package version 0.5-1.4*.

Odegard, M. E., & Berg Jr, J. W. (1965). Gravity interpretation using the Fourier integral. *Geophysics*, *30*(3), 424-438.

Pal, P. C., Khurana, K. K., & Unnikrishnan, P. (1978). Two examples of spectral approach to source depth estimation in gravity and magnetics. *pure and applied geophysics*, *117*(4), 772-783.

Party, K. W. (1991). Large-scale variation in lithospheric structure along and across the Kenya rift. *Nature*, *354*(6350), 223.

Prodehl, C., Jacob, A. W. B., Thybo, H., Dindi, E., & Stangl, R. (1994). Crustal structure on the northeastern flank of the Kenya rift. *Tectonophysics*, *236*(1-4), 271-290.

Ravat, D., Pignatelli, A., Nicolosi, I., & Chiappini, M. (2007). A study of spectral methods of estimating the depth to the bottom of magnetic sources from near-surface magnetic anomaly data. *Geophysical Journal International 169(2)*, 421-434.

Regan, R. D., & Hinze, W. J. (1977). Fourier transforms of finite length theoretical gravity anomalies. *Geophysics*, *42*(7), 1450-1457.

Regan, R.D., Hinze, W.J., 1978. Theoretical transforms of the gravity anomalies of two idealized bodies. *Geophysics 43*, 631-633.

Rosendahl, B. R., Kilembe, E., & Kaczmarick, K. (1992). Comparison of the Tanganyika, Malawi, Rukwa and Turkana rift zones from analyses of seismic reflection data. *Tectonophysics*, *213*(1-2), 235-256.

Russo, R. M., & Speed, E.R. (1994). Spectral analysis of gravity anomalies and the architecture of tectonic wedging, NE Venezuela and Trinidad. *Tectonics 13*(3), 613-622.

Ryan, S. E., & Porth, L. S. (2007). A tutorial on the piecewise regression approach applied to bedload transport data. *Gen. Tech. Rep. RMRS-GTR-189. Fort Collins, CO: US Department of Agriculture, Forest Service, Rocky Mountain Research Station. 41 p., 189*.

Sadek, H. S., Rashad, S. M., & Blank, H. R. (1984). *Spectral analysis of aeromagnetic profiles for depth estimation principles, software, and practical application* (No. 84-849). US Geological Survey.

Serson, P. H., & Hannaford, W. L. W. (1957). A statistical analysis of magnetic profiles. *Journal of Geophysical Research, 62*(1), 1-18.

Shuey, R.T., Schellinger, D.K., Tripp, A.C., & Alley, L.B. (1977). Curie depth determination from aeromagnetic spectra. *Geophysical Journal International, 50*(1), 75-101.

Spector, A., Bhattacharyya, B.K. (1966). Energy density spectrum and autocorrelation function of anomalies due to simple magnetic models. *Geophysical Prospecting, 14*(3), 242-272.

Spector, A., & Grant, F.S. (1970). Statistical models for interpreting aeromagnetic data. *Geophysics 35*(2), 293-302.

Tanaka, A., Okubo, Y., & Matsubayashi, O. (1999). Curie point depth based on spectrum analysis of the magnetic anomaly data in East and Southeast Asia. *Tectonophysics 306*(3-4), 461-470.

Tomé, A. R., & Miranda, P. M. A. (2004). Piecewise linear fitting and trend changing points of climate parameters. *Geophysical Research Letters, 31*(2).

Tselentis, G. A., Drakopoulos, J. & Dimitriadis, K. (1988). A spectral approach to Moho depths estimation from gravity measurements in Epirus (NW Greece). *Journal of Physics of the Earth*, *36*(6), 255-266.

Treitel, S., Clement, W.G., & Kaul, R.K. (1971). The spectral determination of depths to buried magnetic basement rocks. *Geophysical Journal International. 24*(4), 415-428.

Vétel, W., Le Gall, B., & Walsh, J. J. (2005). Geometry and growth of an inner rift fault pattern: the Kino Sogo Fault Belt, Turkana Rift (North Kenya). *Journal of Structural Geology*, *27*(12), 2204-2222.

Vetel, W., & Le Gall, B. (2006). Dynamics of prolonged continental extension in magmatic rifts: the Turkana Rift case study (North Kenya). *Geological Society, London, Special Publications*, *259*(1), 209-233.

CHAPTER IV

LITHOSPHERIC STRUCTURE OF THE CONGO-TANZANIA-BANGWEULU CRATON, THE ZIMBABWE-KAAPVAAL-NIASSA CRATON, AND THE TRANS-SOUTHERN AFRICAN OROGEN

Abstract III

This study attempts to model the lithospheric structure beneath the Congo – Tanzania – Bangweulu craton, the Zimbabwe – Kappvaal – Niassa craton, and the Trans-Southern African orogen by using two-dimensional (2D) radially averaged spectral analysis, 2D-gravity forward modeling, and three-dimensional (3D) density inversion. The findings show that the thickness of the lithosphere beneath the cratonic blocks reaches up to ~256 km. Differently, the thickness of the lithosphere beneath the Trans-Southern African orogen reaches up to ~200 km. The lithosphere-asthenosphere boundary map and the 2D forward models show that the spatial extent of the Congo craton is much wider than what is exposed on the surface and is covered in the southeast by the Luffilian arc. The geographic extent of the Bangweulu craton is also wider than what was previously identified as its cratonic boundary and extends beneath the southwestern limit which is now covered by the remnants of the Neoproterozoic metasedimentary rocks of the Luffilian arc. The LAB map further suggest that the geographic extent of the Niassa craton maybe needs to be redefined to include the entire geographic extent of the Southern Irumide, which is different from the Irumide Metacraton that rests on relatively thinner lithosphere (~ 200 km). The LAB map is also consistent with the general trend of the Trans-Southern Orogen. For example, both the Mesoproterozoic – Neoproterozoic Ghanzi – Chobe orogenic belt and the Neoproterozoic Damara orogenic belt rest on thin lithosphere, about ~ 146 km. Thus, the lithospheric-scale geometry preserved within the Congo – Tanzania – Bangweulu craton, the Zimbabwe – Kappvaal – Niassa craton, and the Trans-Southern African orogeny show that the SWB of the EARS as a whole are regionally controlled by the Trans-Southern Africa orogen -

while the development of individual basins is potentially controlled by the preexisting localized zones of deformation.

4.1 Introduction

The African continent occupies the central part of Greater Gondwana (Fig. 1; Kusky et al., 2003; Stern, 1994). This supercontinent was assembled from a number of cratonic blocks at ~600 Ma that were fragmented following the break-up of Rodinia at ~830 Ma (Stern, 1994; Pisarevsky et al., 2003; Cordani et al., 2003). This tectonic evolution made Africa to emerge as a continent that consists of Archean-Paleoproterozoic cratons, which are amalgamated by Paleoproterozoic - Neoproterozoic orogenic belts (Abdelsalam et al., 2002; Fig. 1). The spatial extents of these Archean-Paleoproterozoic cratons and Paleoproterozoic - Neoproterozoic orogenic belts have been determined by combined geologic information obtained from surface mapping, geochemical and geochronological studies, and seismic tomography of various resolution (Poujol et al., 2003; Eglington and Armstrong, 2004; Hanson et al., 2011; Abdelsalam et al., 2011; Sarafian et al., 2018). These studies resulted in establishing major cratons in Africa including the West African craton, the Congo craton, and the Kalahari craton (Fig. 1; Unrug, 1983; Miller1993; Abdelsalam et al., 2011;). The northern part of the continent is occupied by the Saharan Metacraton (Fig. 1), which is thought of as an Archean – Paleoproterozoic craton that was remobilized during the Neoproterozoic (Abdelsalam et al., 2011; Emishaw and Abdelsalam, 2019).

The West African craton and the Saharan Metacraton are separated by the Neoproterozoic Trans-Sahara orogen (Abdelsalam et al., 2002); the Saharan Metacraton is separated from the Congo craton by the Oubanguides orogen (Black and Liegeois, 1983; Abdelsalam et al., 2002; Abdelsalam et al., 2011); whereas the Congo craton is separated from the Kalahari craton by the Paleoproterozoic – Neoproterozoic Trans-Southern Africa orogenic belt (Evans et al., 2019). The Saharan Metacraton, Congo craton and Kalahari craton are limited in the east by the East African orogen (Figure 1).

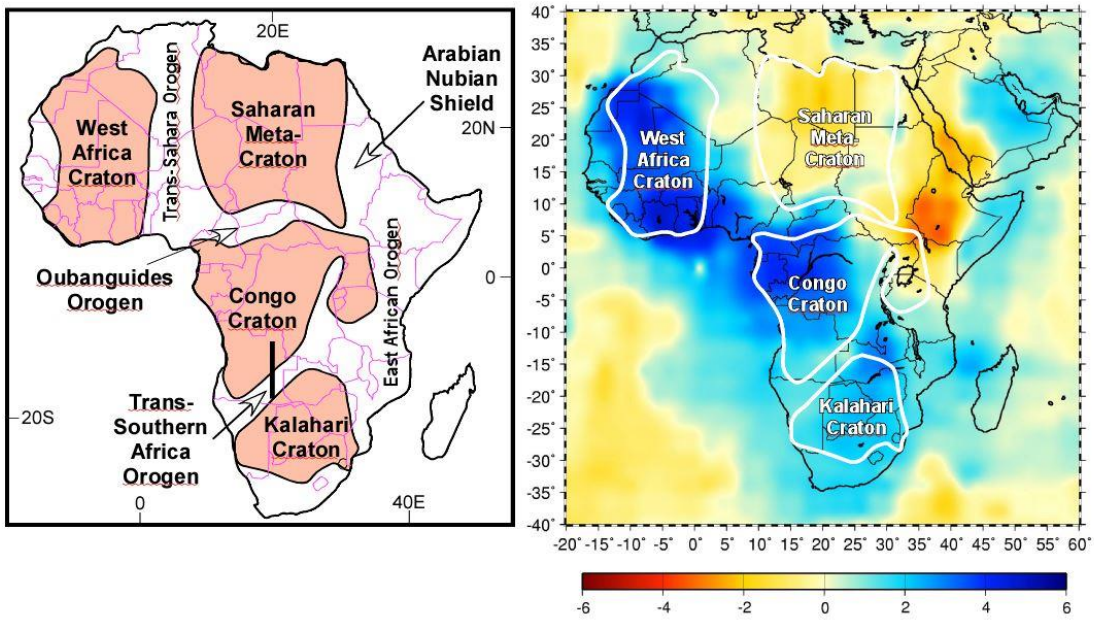

Figure 4.1: (Left) Tectonic map of Africa constituting four major cratons (the West Africa craton, the Saharan meta-craton, the Congo craton, and the Kalahari craton) that have given Africa its present shape along with major orogens along which the cratons are assembled (the Trans-Southern orogen, the Trans-Southern Africa orogeny, the Oubanguides orogen, and the East African orogeny). (Right) Grand 2002 shear tomography model with faster velocity beneath the stable and meta-cratonized cratons.

The spatial distribution of Paleoproterozoic – Neoproterozoic cratons and Paleoproterozoic – Neoproterozoic orogenic belts has largely controlled the evolution of continental rifts in the African continent, especially the Paleozoic – Mesozoic Karoo rift system and the Cenozoic East African Rift System (EARS) (Emishaw and Abdelsalam, 2019). For

example, the EARS, which constitutes the Afar Depression and the Main Ethiopian Rift in the north and the Eastern and Western Branch further south, largely extends within the East African orogen (Emishaw et al., 2017; Demissie et al., 2018; Emishaw and Abdelsalam, 2019). The Southwestern Branch of the EARS, which was initiated in the Palozoic – Mesozoic Karoo rift system that was reactivated in the Cenozoic during the onset of the EARS, largely extend within the Trans-Southern Africa orogenic belt (Fairhead and Girdler, 1969; Reeves, 1972; Scholz et al., 1976; Modisi et al., 2000)

In this work, I examine the spatial correlation between the Archean – Paleoproterozoic cratons (Congo craton and Kalahari craton), Paleoproterozoic – Neoproterozoic Trans-Southern Africa orogenic belt, and the Paleozoic – Mesozoic to Cenozoic Southwestern Branch of the EARS. Here, I consider the Congo craton as constituting the Congo-Tanzania –Bangweulu craton, and the Kalahari craton as constituting the Zimbabwe-Kaapvaal-Niassa craton (Fig. 3).

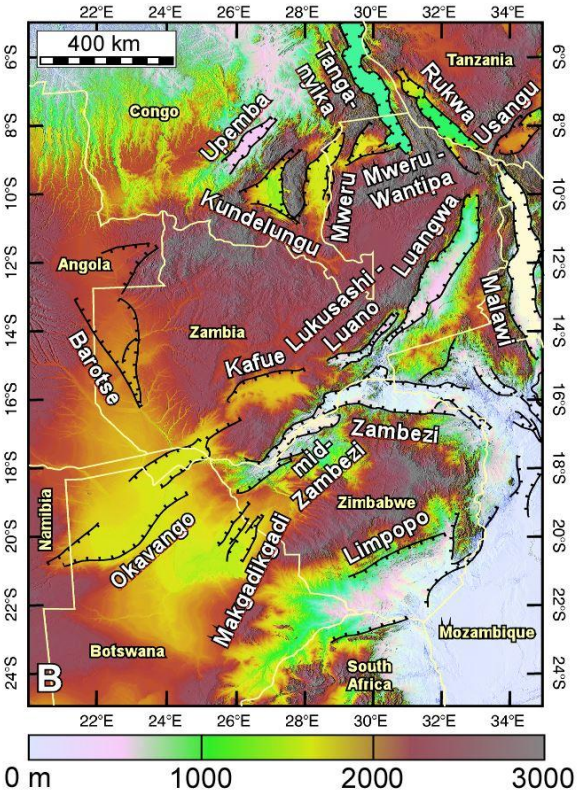

Figure 4.2: Shuttle Radar Topography Mission (SRTM) DEM of the Southwestern Branch (SWB) of the EARS.

I consider the Trans-Southern Africa orogenic belt as constituting the Paleoproterozoic Magondi and Limpopo orogenic belt, the Paleoproterozoic – Mesoproterozoic Kibaran orogeic belt, the Mesoproterozoic – Neoproterozoic Irumide, Southern Irumide, and Ghanzi – Chobe orogenic belt, and Neoproterozoic Lufillian arc, and Zambezi and Damara orogenic belts (Fig. 2). I used two-dimensional (2-D) radially-averaged power spectral analysis, 3D Moho inversion, and 2D forward gravity modelling of the World Gravity Model 2012 (WGM 2012). The findings of these methods will enablable us to: 1) determine the spatial extent of cratons, including the ones covered by Phanerozoic sedimentary rocks; 2) estimate thickness variation of the Sub-continental lithospheric mantle of each tectonic entity; 3) determine the spatial and tectonic relationship between the Southwestern Branch of the of the East African Rift System and the Trans-Southern Africa orogen; and 4) image discrete suture zones. These findings would allow to isolate factors that determine the preferential nucleation of continental rifts. They will also give insight on the role of preexisting structure in determining the geometry of the individual basins of the SWB of the EARS.

4.2 Precambrian Geology

4.2.1 The Congo-Tanzania-Bangweulu craton

Within the study area, the eastern part of the Congo craton, the southwestern part of the Tanzania craton and the entire Bangweulu cratonic block are exposed. The Congo craton is separated from the Bangweulu cratonic block by the Paleoproterozoic-Mesoproterozoic Kibaran orogenic belt. The southern limit of the Bangweulu block is covered by post-tectonic granite. The Tanzania craton is separated from the Bangweulu cratonic block by the Paleoproterozoic Ubendian orogenic belt (Fletcher et al., 2018). The formation of the composite Congo-Tanzania-Bangweulu craton resulted from two orogenic events. The first event is Paleoproterozoic in age and is marked by the collision between the Tanzania craton in the northeast with the Bangweulu

cratonic block to the southwest. This collision resulted in the formation of the Paleoproterozoic NW-trending Ubendian orogenic belt (Lenoir et al., 1994; Fig. 3). The second event is Paleoproterozoic – Mesoproterozoic in age and is marked by the Congo craton in the northwest with the Tanzania craton – Bangweulu cratonic block to the southeast. This event resulted in the formation of the Paleoproterozoic – Mesoproterozoic Kibaran orogenic belt (Begg et al., 2009; Fig. 3).

Few studies have focused on imaging the lithospheric structure of the Congo – Tanzania – Bangweulu craton. For example, using seismic tomography, Priestley and McKenzie (2006) estimated that the Congo craton is underlain by ~250 km thick lithosphere. The lithospheric depth estimate of the Congo craton beneath the Congo basin that overlies Neoproterozoic - Mesozoic clastic sedimentary rocks was estimated to be ~ 250 km based on the inversion of surface waveforms, subsidence history and gravity data (Crosby et al., 2010). A recent study by Yu et al. (2017) shows a high P-wave velocity beneath a portion of the Congo craton, located to the northwest of the Okavango Rift Zone (Fig. 2), which extends to the depth of 250- 350 km. The lithospheric thickness of the archean Tanzanian craton is estimated to be 250 km (Ritsema et al., 1998, Weeratne et al., 2003; Fig. 3). This estimate considers that the craton is intact and has its thickest cratonic root beneath its center. However, recent geochronological, isotopic, and geophysical studies suggest that the lithosphere of the Tanzania craton might have been modified during subsequent geologic events or the craton itself might have been made up of smaller cratonic blocks stitched together along ancient Precambrian Suture Zones. Thomas et al. (2016), for instance, suggested the possibility that the southwestern margins of the Tanzania craton might have been metacratonized during the Paleoproterozoic orogenic event now preserved as the Ubendian orogenic belt to the southwest of the craton. After mapping the lithosphere-asthenosphere boundary (LAB) of the Tanzania craton, Fletcher et al. (2018) suggested that some

of the segments of the North Tanzania Divergence of the EARS within the eastern side of the Tanzania craton might have developed through the strain localization within these suture zones. Similarly, Corti et al. 2007; Katumwehe et al., 2015, using analogue models and aeromagnetic data integrated with shuttle radar topographic mission data concluded that the upper crustal lithospheric pre-existing fabric to a large extent have played a role in strain localization during rift evolution and propagation.

Using a regional magnetotelluric (MT) transect, Sarafian et al. (2018) showed that the Neoarchean Bangweulu cratonic block which lies to the SW part of the Tanzanian craton is underlain by a thick sub continental lithospheric mantle (SCLM) that reaches up 250 km in the central part of the block.

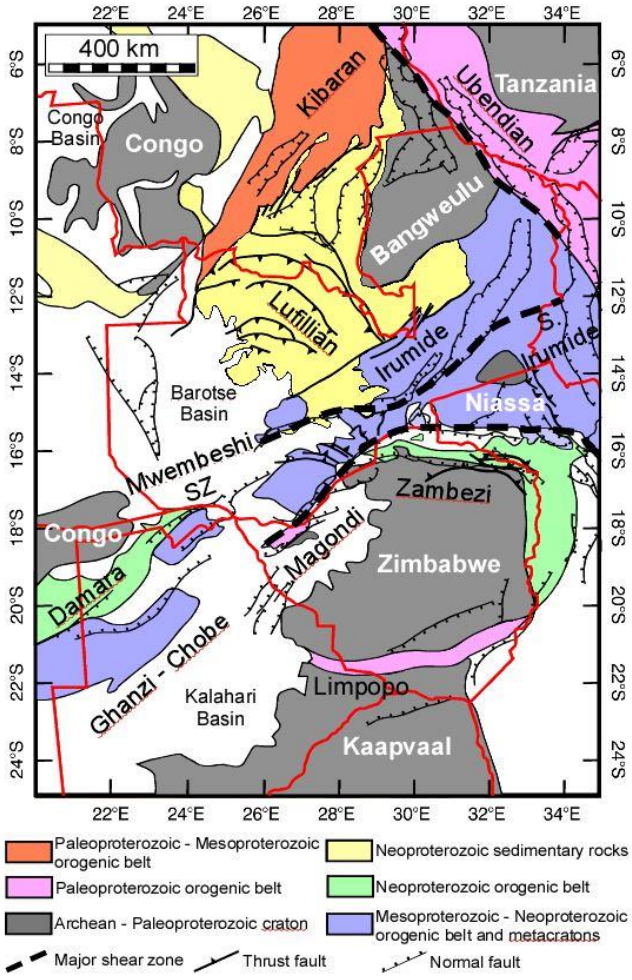

Figure 4.3: Precambrian tectonic map of the SWB of the EARS. Modified after Key and Ayres (2000) and Westerhof et al. (2008)

4.2.2 The Zimbabwe-Kaapvval-Niassa craton

The Zimbabwe craton is separated from the Kaapvaal craton by the east-northeast trending 250 km wide zone of granulite facies called the Limpopo belt (Fig. 3). The exposed parts of the Kaapvaal craton and the Zimbabwe craton are mainly granitic gneisses. Patches of greenstone belts of varying shape and size are also exposed within the near proximity of both the Zimbabwe and Kaapvaal cratons (Begg et al., 2009; Van Reenen, 2011). The lithospheric thickness of these cratons is in the range of (180 – 250) km (Muller et al., 2009; Miensopust et al., 2011; Khoza et al., 2013).

The Precambrian terranes southeast of the Bangweulu cratonic block have been traditionally referred to as the Irumide and Southern Irumide orogenic belts (Johnson et al., 2006). Recent MT study by Sarafian et al. (2018) has been able to recall the Niassa craton, the term that was initially used by Andreoli (1984), as their MT study was able to resolve relatively thinner lithosphere (~ 100 km thick) beneath the Irumide orogenic belt, and thicker lithosphere (~ 250 km) beneath Niassa craton within the Southern Irumide.

4.2.3 The Trans-Southern Africa Orogen

The Trans-Southern Africa Orogen constitutes, from older to younger, the Paleoproterozoic Magondi orogenic belt, the Paleoproterozoic – Mesoproterozoic Kibaran orogenic belt, the Mesoproterozoic – Neoproterozoic Irumide metacraton, and Southern Irumide and Ghanzi – Chobe orogenic belts, and the Neoproterozoic Zambezi and Damara orogenic belts and the Lufillian arc (Fig.0 2 and Fig. 3).

4.2.4 The Magondi orogenic belt

The Magondi orogenic belt has resulted from the Mangodian orogeny that metamorphosed and deformed sediments and volcanics of early-mid Proterozoic Magondi Super-group (Treloar, 1988). The Magondi orogenic belt was formed in the Northwestern margin of the Archean Zimbabwe – Kaapvaal craton and borders Mesoproterozoic – Neoproterozoic Southern Irumide belt in the northwest (Fig.3; Hanson et al., 1988). Previous studies (Treloar, 1988) have suggested that the Magondi super group is largely composed of the volcanic and metsedimentary that have gone through stages of metamorphism. To the south, these super group rocks are thin and thrust over the SE to the Zimbabwean Archean craton while to the north they thin with increasing metamorphic grade. The Magondi orogenic belt is covered by the Paleozoic – Mesozoic Karoo sedimentary rocks of the Kalahari basin, but isolated exposures are found in the northwestern part of Zimbabwe (Fig. 3; Majaule et al., 2001). Majaule et al. (2001) obtained a U-Pb zircon age of ~2039 Ma from an isolated granitic outcrop within the Magondi orogenic belt and interpreted this as the crystallization age. In addition, Majaule et al. (2001) obtained an age of ~2673 Ma from zircon xenocrysts and interpreted this to indicate the presence of an Archean crustal component.

4.2.5 The Kibaran orogenic belt

The NE-trending Mesoproterozoic Kibaran orogenic belt is exposed on the western margin of the Congo craton (Fig. 3). It is dominated by granitic gneisses and granitic intrusions that were emplaced and deformed during the Paleoproterozoic – Mesoproterozoic (e.g. Thomas et al., 1994; Tack et al., 1994). These rocks were reworked during the Neoproterozoic (e.g. Thomas et al., 1994), possibly due to final collision between the Congo craton and the Tanzania – Bangweulu craton (e.g. Begg et al., 2009) which resulted into the regional horizontal foliation and a decollement of the sedimentary cover over its basement

Just like the Mesproterozoic Kibaran fold belt, the Irumide metacraton and Southern Irumide orogenic belt lies south of the Bangweulu cratonic block (Fig. 3) and are believed to have similar tectonic origin due to uncertainties in discriminating their boundaries and degree of metamorphism (De Waele et al., 2006A). However, based on the U-pb Zircon studies, the Kibaran and the Irumide belts have different ages and their spatial tectonic origin have no correlation (De Waele et al., 2006A). These Precambrian tectonic blocks have been described as a crustal-scale thick-skinned fold and thrust belt that constitutes Paleoproterozoic gneissic basement, Paleoproterozoic metasedimentary rocks, and Mesoproterozoic – Neoproterozoic granitoids (Johnson et al., 2005, 2006; De Waele et al., 2006A). As mentioned earlier, Sarafian et al. (2018) used MT survey to show that the lithosphere beneath the core of the Southern Irumide orogenic belt has a thickness that is comparable to other cratons in Africa, hence reintroduced the term "Niassa craton" for this Precambrian tectonic block. Also, as mentioned earlier, Sarafian et al. (2018) reintroduced the term "Irumide metacraton" to identify the Irumide orogenic belt as the metacatonized southern margin of the Bangweulu cratonic block because of the presence of a relatively thinner lithosphere beneath this Precambrian tectonic block and also the presence of Archean – Paleoproterozoic basement rocks. The metacratonization occurred during collision of the Bangweulu cratonic block with the Zimbabwe – Kaapvaal craton during the Mesoproterozoic – Neoproterozoic (DeWaele et al., 2006B). The MT study of Sarafian et al. (2018) indicated that the Mwembeshi Shear Zone is the suture zone between the Niassa craton and the Irumide metacraton.

4.2.6 The Ghanzi – Chobe – Damara orogenic belt

The Northeastern trending Mesoproterozoic - Neoproterozoic Ghanzi – Chobe orogenic belt is made-up of metamorphosed rhyolites and volcaniclastic metasedimentary rocks, as well as metamorphosed sandstones, siltstones and mudstones (Key and Ayres, 2000). Differently, the

Neoproterozoic Damara orogenic belt is made-up of migmatites, granitic gneisses and granites (Key and Ayres, 2000). The Chanzi – Chobe and the Damara orogenic belts and the Paleoproterozoic Magondi orogenic belt are located in between the Congo craton in the northwest and the Zimbabwe – Kaapvaal craton to the southeast (Fig. 3). Little is known about the tectonic evolution of the Ghanzi – Chobe and the Damara orogenic belts in Botswana because these are buried beneath the Paleozoic – Mesozoic Karoo sedimentary rocks of the Kalahari basin and most of the geological information about these Precambrian tectonic blocks came from geophysical surveys and borehole data (Key and Ayres, 2000). However, the Damara orogenic belt in the neighboring Namibia is considered to have been formed through a series of Neoproterozoic suturing events between the Congo craton and the Zimbabwe – Kaapvaal craton (e.g. Gray et al., 2008).

4.2.7 Zambezi orogenic belt

The Neoproterozoic Zambezi orogenic belt is exposed in the northern and eastern margins of the Zimbabwe – Kaapvaal craton (Fig. 3; Hanson et al., 1994; Hargrove et al., 2003). It records Neoproterozoic "interaction" between the Congo craton in the north and the Zimbabwe – Kaapvaal craton to the south (Fig. 3; Hanson et al., 1994; Hargrove et al., 2003). The belt is dominated by granitic gneisses where thin-skinned tectonics resulted in southward emplacement of these rock onto the northern edge of the Zimbabwe – Kaapvaal craton (e.g. Goscombe et al., 2000).

4.2.8 The Lufilian arc

The Lufilian arc (Fig. 3), which is dominated by Neoproterozoic clastic and carbonate sedimentary rocks, is thought to represent an orogenic belt that was formed as a result of collision between the Congo-Tanzania-Bangweulu craton and the Zimbabwe – Kaapvaal craton at ~550 Ma (Porada and Berhorst, 2000). This collisional event followed the formation of a rift basin

around the margin of the Congo craton during the fragmentation of Rodinia. The structural style within the arc varies considerably with a top-to-the-northeast fold and thrust belt dominating its southwestern part and a foreland sedimentary basin lying flat above the southwestern margin of the Bangweulu cratonic block in the northeast (Fig. 3; Zientek et al., 2014).

4.3 Southwestern Branch of the East African Rift System

The amagmatic SWB of the EARS is a NE-SW trending, ~1000 km wide corridor of rift basins extending for ~1700 km from the west sides of the Tanganyika and the Malawi rifts (Fig. 2; e.g., Fairhead and Girdler, 1969; Reeves, 1972; Scholz et al., 1976; Modisi et al., 2000; Sebagenzi and Kaputo, 2002). The rift basins extending from the southwestern side of the Tanganyika rift include Upemba, Kundelungu, Mweru – Wantipa, Mweu, and possibly Barotse (Fig. 2). These are concentrated in the southeastern border of Congo with Zambia and the southeastern border of Angola with Zambia (Fig. 1B). The evolution of the SWB of the EARS is controlled by pre-existing lithospheric fabric. For example, the Upemba extends within the Kibaran orogenic belt, the Kundelungu and Mweru extends within the Lufllian arc, but the Mweru – Wantipa extends on the northeastern margin of the Bangweulu cratonic block (Figures 1B and 2). The rift basins that extend from western side of the Malawi rift stretches along the southern border of Zambia with Malawi, Mozambique, and Zimbabwe and include Luangwa, Lukusashi-Luano, Kafue, and mid-Zambezi (Figure 1B). These basins are along-strike with the Okavango Rift Zone, which is found in the northwestern part of Botswana and southwestern Zambia (Figure 1B). In addition, the Makgadikgadi is found to the southeast of the Okavango Rift Zone along the border between Botswana and Zimbabwe (Fig. 2). The Okavango Rift Zone is considered to be the youngest rift basin of the SWB and it is suggested that it can be as young as 200,000 years (Modisi et al., 2000; Huntsman-Mapila et al., 2006; Kinabo et al., 2008). Little

is known about the structural and tectonic development of different rift basins of the SWB except for the Okavango Rift Zone, and to a lesser extent the Luangwa Rift Valley.

The Okavango Rift Zone is defined by poorly-developed NE-trending border faults (Kinabo et al., 2007; 2008; Mosley-Bufford et al., 2012) and it is characterized by the presence of high heat flow anomaly (Leseane et al., 2015). The Mesoproterozoic – Neoproterozoic Ghanzi-Chobe and Damara orgenic belts are situated in between the Congo craton in the northwest and the Magondi orogenic belt to the southeast underlies the Okavango Rift Zone (Fig. 2; Leseane et al., 2015). The presence of these orogenic belts played a major role in strain localization during the onset of the Okavango Rift Zone (e.g. Leseane et al., 2015). Yu et al. (2015A) found that the Moho beneath the rift zone is elevated by 4 and 5 km ~36 km in depth. In addition, Yu et al. (2015B) found faster NE-SW shear wave splitting direction beneath the Okavango Rift Zone. However, no thermal anomalies in the transition zone is found beneath the rift (Yu et al., 2015C). Yu et al. (2017) found low P-wave velocity anomaly in the upper asthenosphere beneath the rift zone and interpreted this as due to the presence of decompression melt caused by asthenospheric ascendance due to lithospheric thinning.

The geological and geophysical observations summarized above can be taking as an indication that the Okavango Rift Zone is currently tectonically active and can be considered as part of the active extensional tectonic regime of the EARS. In addition, it has been observed that sites of hot springs in Zambia coincide with the border faults of the Luangwa rift (Sakungo, 1985). This rift became well developed by the end of the Karoo rifting event, which marks the early stages of the fragmentation of Gondwana during the Permian – Triassic (Daly et al., 1989; Banks et al., 1995). The presence of potentially high heat flow anomalies associated with the Luangwa rift (as suggested by the presence of hot springs) can be considered to indicate that the rift has been reactivated by the extensional tectonic activities of the EARS. Recently, from a

regional MT profile, Sarafian et al. (2018) have shown that the Luangwa rift is underlain by a high conductivity anomaly extending to a depth of ~300 km. Sarafian et al. (2018) explained this as due to the presence of a Precambrian suture zone represented by the Mwembeshi Shear Zone that allowed for thermal softening of the lithosphere beneath the Luangwa rift facilitating strain localization.

4.4 Data and Methods

4.4.1 DATA

The World Gravity Map (WGM) 2012 is a high-resolution gravity map and digital grid computed at global scale from Earth's gravity and elevation models. The WGM2012 includes three anomaly maps: surface free-air, complete Bouguer, and isostatic anomalies. These anomalies are derived from the EGM2008 Geopotential model and Topography 1 arc min (ETOPO1) Global Relief Model. The EGM2008 is made up of the global set of area-mean free-air gravity anomalies defined on a 5 arc-minute equiangular grid and the least squares combination of the Spain's Instituto Tecnológico de Galicia Gravity Recovery and Climate Experiment (ITG-GRACE03S) gravitational field model. WGM2012 accounts for the heterogeneity of most surface masses such as atmosphere, land, oceans, inland seas, lakes, ice caps, and ice shelves. (Figure 4).

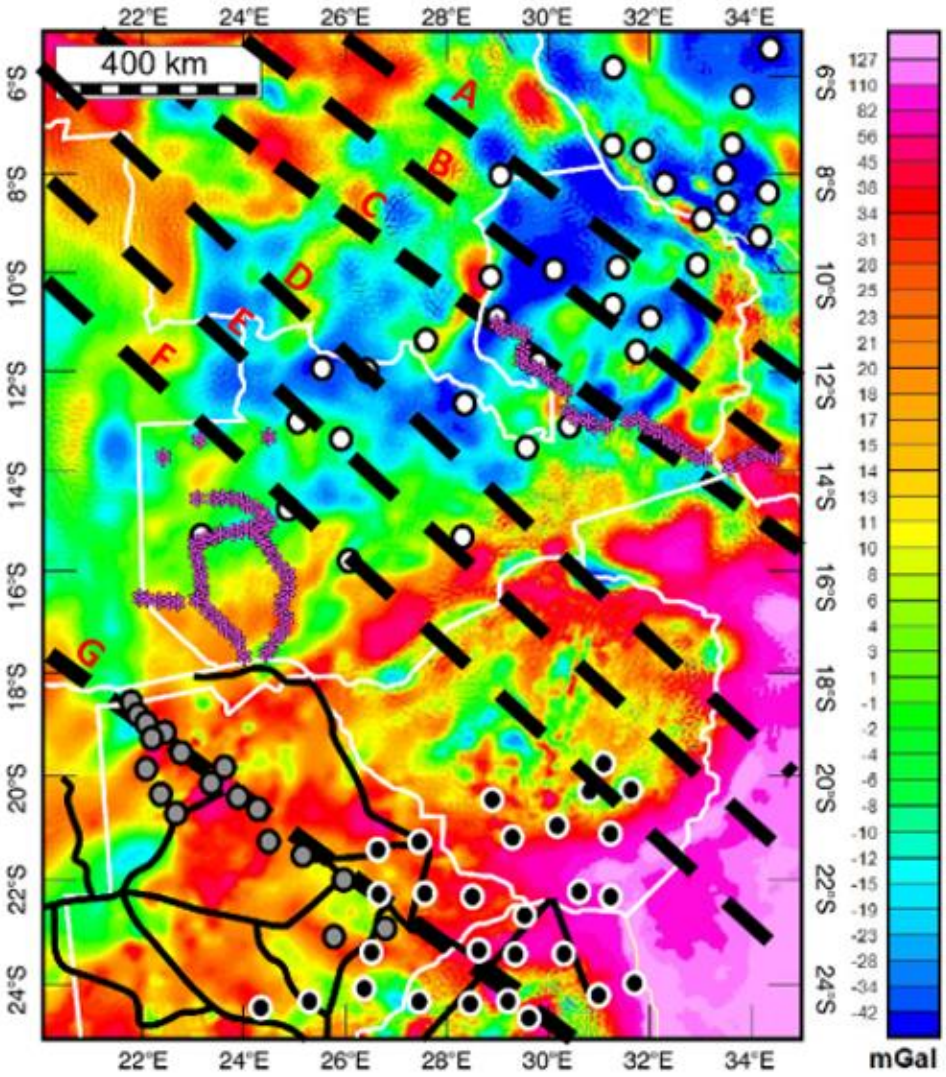

Figure 4.4: Bouguer gravity anomaly map from the World Gravity Model 2012 (WGM 2012) showing major passive seismic and Magneto Telluric (MT) experiments covering parts of the Southwestern Branch (SWB) of the East African Rift System (EARS). The passive seismic experiments include: Black circles = South Africa Seismic Experiment (SASE). White circles = Africa Array. Grey circles = Processes of Rift Initiation, Development and Evolution (PRIDE). MT experiments include: Black thick lines = Southern Africa MT Experiment (SAMTEX). Pink stars = PRIDE. 8 2D forward gravity models are constructed along the thick dashed black lines.

4.4.2 Methods

4.4.2.1 Two-dimensional (2D) radially averaged power spectrum analysis

It has long been recognized that the Fourier spectral analysis can be applied to potential field anomalies to estimate the depth to the interior structure of the Earth such as the Moho interface, the basement, and the lithosphere-asthenosphere boundaries (Tselentis et al., 1989; Emishaw et al., 2017; Fletcher et al., 2018). Fourier integrals of geopotential fields are possible because the Earth surface acts like a low-pass filter to geopotential field anomalies, granting them

wave like characteristics even though they do not inherently exhibit them (Mark Erie Odegard, 1975). The fundamental of this transformation is that any function in time or space domain can be represented by an equal number of sinusoidal function in the frequency domain. The power spectrum of a frequency domain is represented by the equation:

$$Ph(r) = e^{-2hrP0(r)}$$

Where "Ph(r)" is the power spectrum of the top gravity surface "P0(r)" and "r" is the wave number. The presentation of this formula in the linear equation is expressed as:

$$\text{Ln } Ph(r) = -2hr + c$$

Where "h" is the slope of the spectral curve and "C" is a constant coefficient. The log plots of

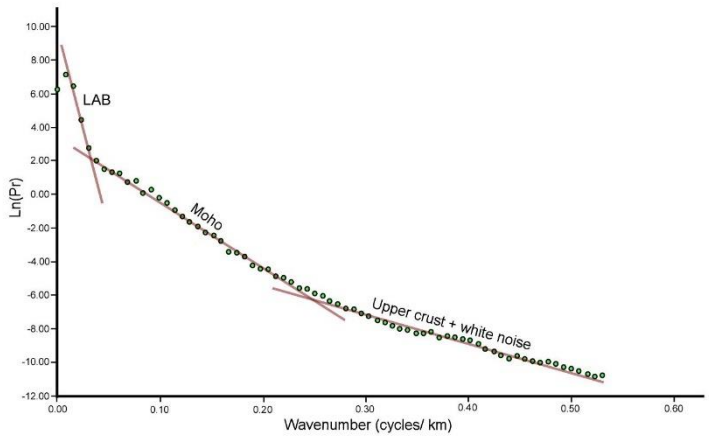

Figure 4.5: Example of two-dimensional radially-averaged spectrum. The lower wavenumber values that corresponds to higher logarithmic energy spectrum estimates depth to the lithosphere-asthenosphere boundary. As the wavenumber values progressively decreases in relation to the logarithmic power spectrum, shallower interfaces, such as depth to the Moho and depth to crystalline basement can be estimated.

"Ln_P" versus the wavenumber results in the power spectrum graph from which the depth to the source can be estimated (Tselentis et al., 1988; Emishaw et al., 2017). The depth to the lithosphere-asthenosphere boundary is estimated from the upper slope, which has a distinctive slope that is different from the middle and shallow slopes of the spectral curve (Fig. 5).

4.4.2.2 Two-dimensional (2D) forward gravity modelling

To capture the 2D regional heterogeneity across Precambrian tectonic blocks and the overlying rift segments of the SWB of the EARS, I developed a number of 2D forward gravity models from the Bouguer gravity anomalies of the WGM 2012. I developed these models to estimate the depth to the LAB. These models are developed using the 2D GYMSYS Oasis Montaj software. The software bases the algorithms published by Talwani et al. (1959) and Won and Bevis (1987). I mainly defined four layers to each model including the upper crust, with the density value of 2.6 g/cm^3; the lower crust, with the density value of 2.8 g/cm^3; the sub-continental lithospheric mantle (SCLM), with the density value of 3.1 g/cm^3; and the asthenosphere, with the density value of 3.3 g/cm^3.

4.4.2.3 Three-dimensional (3D) density inversion

Gravity data can be modeled in two ways. The first one is forward gravity modeling. This allows creating a synthetic dataset from a geologic model that matches the observed dataset. This suffers from non-uniqueness as many models could produce the same exact synthetic dataset that matches the observed dataset. To overcome this limitation, sensitivity analysis and good understanding of the geologic setting are required. The second approach is gravity inversion. This method, unlike forward gravity modeling, produces the geologic model from the original data. The similarity between these two methods is that both would require an initial model from which the final model could be derived.

The Parker and Oldenburg algorithm rests on the idea that Earth serves as a low pass filter for gravity data. In other words, high frequency gravity data are attenuated at depth. This makes gravity data, which mainly measure density variations, geopotential fields. This allows the application of Fourier transform to gravity data. The mathematical relationship of gravity data for inversion was first defined by Parker (1973). His mathematical relationship, however, only decomposes gravity fields and does not converge the inverted depth through iterations. To overcome this limitation, the equation was rearranged by Oldenburg (1974) as follows:

For the inverted depth to converge, however, additional factors were necessary. Oldenburg (1974) expressed the equation with two important parameters WH, which is the lower bound of the wavenumber (k), and SH, which is the upper bound of the wavenumber (k).

Gomez-Ortiz and Agarwal (2005) have implanted the Parker and Oldenburg algorithm to image the Moho interface. To estimate depths to the Moho, two constant values have been introduced: 1) the density contrast, and 2) average depth. If these two values are biased, the final Moho map comes out biased too. To obtain a less biased Moho model, constraints from previous seismic studies are usually applied. This, however, is not always the case; especially when investigating tectonic settings that are not well explored. To overcome this limitation, a new approach is designed to simulate and invert gravity data. For this study, 1012 simulated Moho models were used to compute the statistical average of the Moho depths through bootstrapping. This constitutes sampling from the corresponding cells of all models such that the weighted and subsequently bootstrapped average values would result in the final solution to the Moho model.

4.5 RESULTS

4.5.1 The Bouguer gravity anomalies

The Bouguer gravity anomalies map (figure 4) captures the density variations that emanates from the Congo-Tanzania-Bangweulu craton, the Zimbabwe-Kaapvaal-Niassa craton, and the Trans-Southern African orogen. The Congo craton has the high gravity anomalies values on the outer edges and low gravity anomalies values at its center. The presence of a mass deficit at the center of the Congo craton seem to suggest the presence of a pronounced cratonic root. The Zimbabwe craton also has a similar Bouguer gravity anomalies, but contains higher Bouguer gravity anomalies in the east, which is most likely influenced by the gravity signatures of the Indian Ocean continental shelf and the presence of volcanic rocks within Mozambique. The other distinct Bouguer gravity anomalies pattern in figure 4 is the N-E trending low gravity anomalies that extends from the Lufillian arc to the Ubendian orogenic belt. The pattern of these low gravity anomalies are likely registered by the presence of the SWB of the EARS and the Mesozoic old Karroo rift systems that are formed within the Trans-Southern African orogeny, including the foreland basin developed within the Luffillian. (Figures 2 and 4).

4.5.2 LAB results

The Lithosphere Asthenosphere Boundary (LAB) thickness map (Fig. 6 and Fig. 7) shows the presence of significant lithospheric thickness variation between the tectonic entities. In general, the broad overview of the LAB map shows thinner lithosphere beneath the Trans-Southern Africa orogen and thicker lithosphere beneath the Zimbabwe-Kaapvaal craton and the Congo-Tanzania-Bangweulu craton (Fig. 6 and Fig. 7). From the whole Trans-Southern Africa orogen, The Paleoproterozoic Ubendian orogenic belt, the Paleoproterozoic Limpopo orogenic belt, the Neoproterozoic Damara orogenic belt, and the Neoproterozoic – Mesoproterozoic Ghanzi – Chobe orogenic belt (Fig. 7B) have relatively thinner lithosphere with a mean thickness

of ~146 km. The lithosphere of the Mwembeshi localized zone of deformation that separates the Irumide Metacraton from the Niassan craton is also relatively thinner with a mean depth to the LAB of 150 km (Fig. 7A).

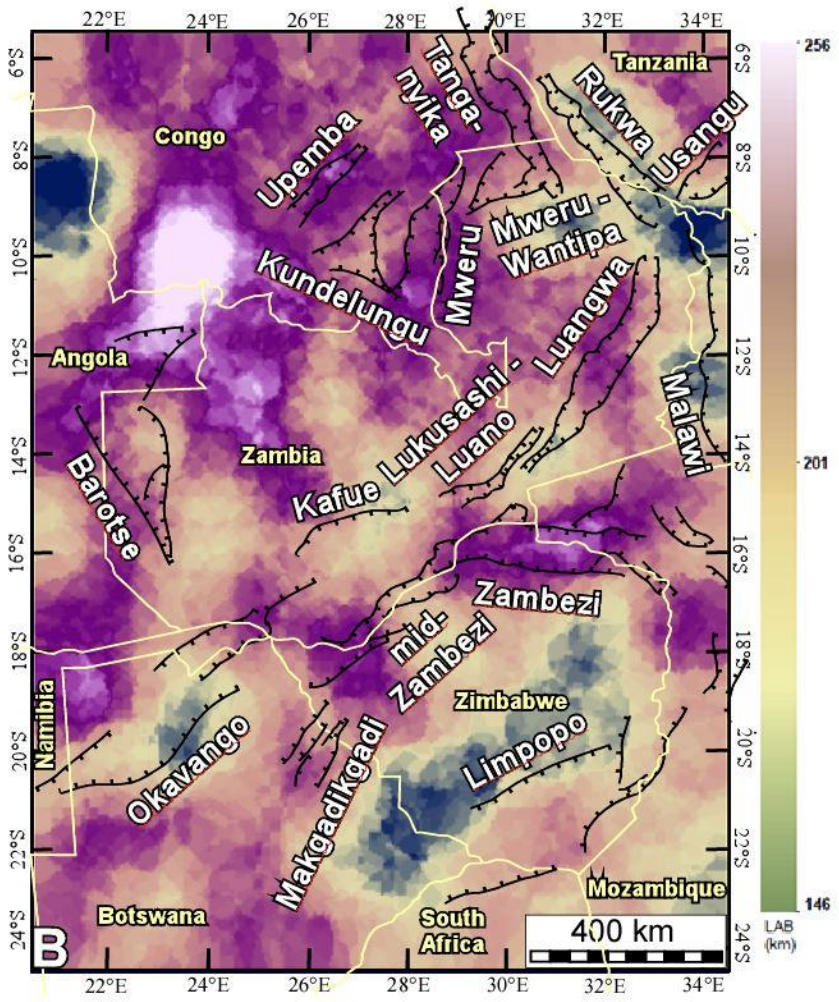

Figure 4.6: The SWB of the EARS extensional structures superimposed on the LAB map. Both the surface and lithospheric structure show the presence of thinner lithosphere beneath the Trans-Southern African orogeny over which the SWB of the EARS have developed.

From the cratons, the anomalously thick lithosphere is observed beneath the Congo craton with a mean depth to the lithosphere asthenosphere boundary of 250 km. The Bangweulu and the Niassan cratons also show anomalously thick lithosphere that reaches up to 250 km. The Zimbabwe craton is the most heterogeneous craton in the region with a mean lithospheric depth that ranges between ~ (160 – 210) km (Fig. 7A). The northeastern portion of the Bangweulu block, which is on the margin of the Ubendian orogenic belt, also has a relatively thinner lithosphere (~ 150 km).

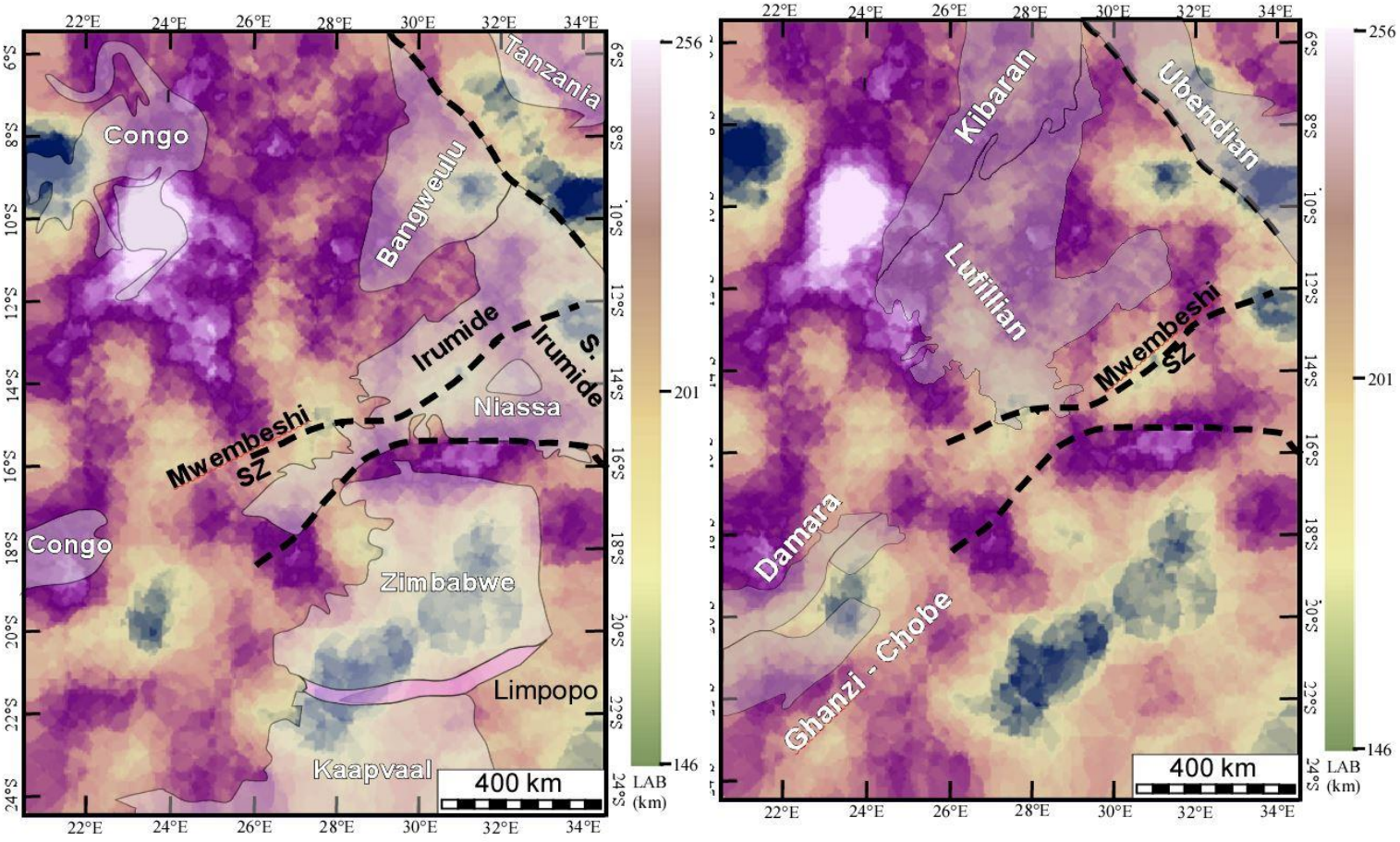

Figure 4.7: Spatial maps showing the extent of (A) the Congo-Bangweulu-Tanzania craton and the Kaapvall-Zimbabwe-Niassa craton, and (B) the Paleoproterozoic-Mesoproterozoic and Mesoproterozoic-Neoproterozoic orogens superimposed on the LAB map. The maps in general show the lithosphere is thicker beneath the cratons.

The LAB map shows that SWB rifts such as the Okavango, the Kafue, the Lukusashi-Luano, the Luangwa, the Bartose, the Kundelungu, the Mweru – Wantipa, and the

Eastern Branch rifts such as the Rukwa, the Usangu, and the Tanganyika are localized within relatively thinner lithosphere of orogenic belts (Fig. 6 and Fig. 7). Also, the Tanganyika rift and the Mweru – Wantipa rift are developed within the thermally and mechanically weakened lithosphere of the northeastern block of the Bangweulu block.

The thinner lithosphere beneath the Mwembeshi Shear Zone where the Luangwa depression is present also seem to suggest the influence of preexisting structures in strain localization (Fig. 6 and Fig. 7).

4.5.3 2-D forward gravity modeling results

The depths estimates to the Lithosphere-Asthenosphere Boundary (LAB) were also obtained by 2D gravity forward models that are constrained by the spectral LAB map and seismic lithospheric depth point estimates beneath the cratons and orogenic belts.

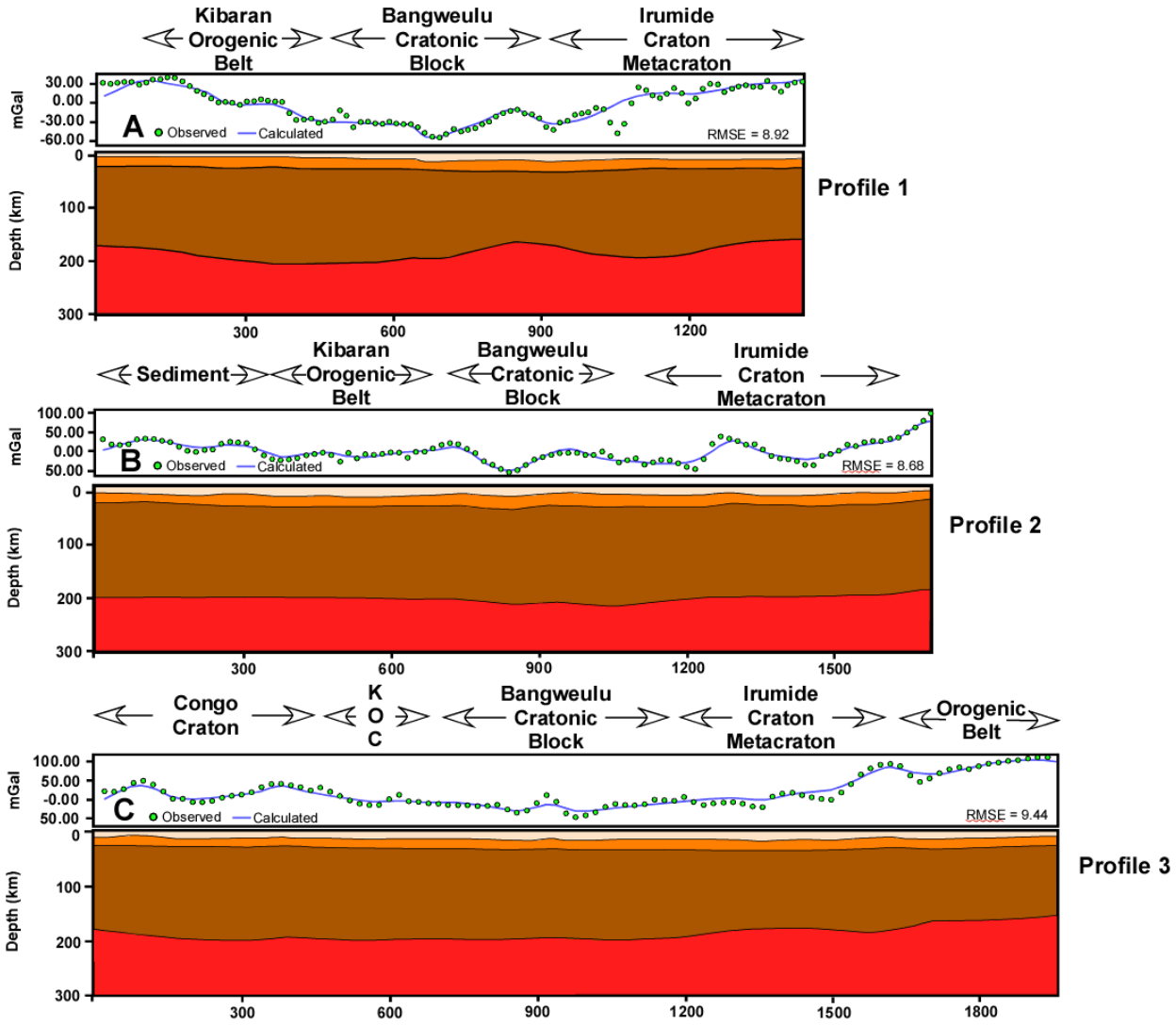

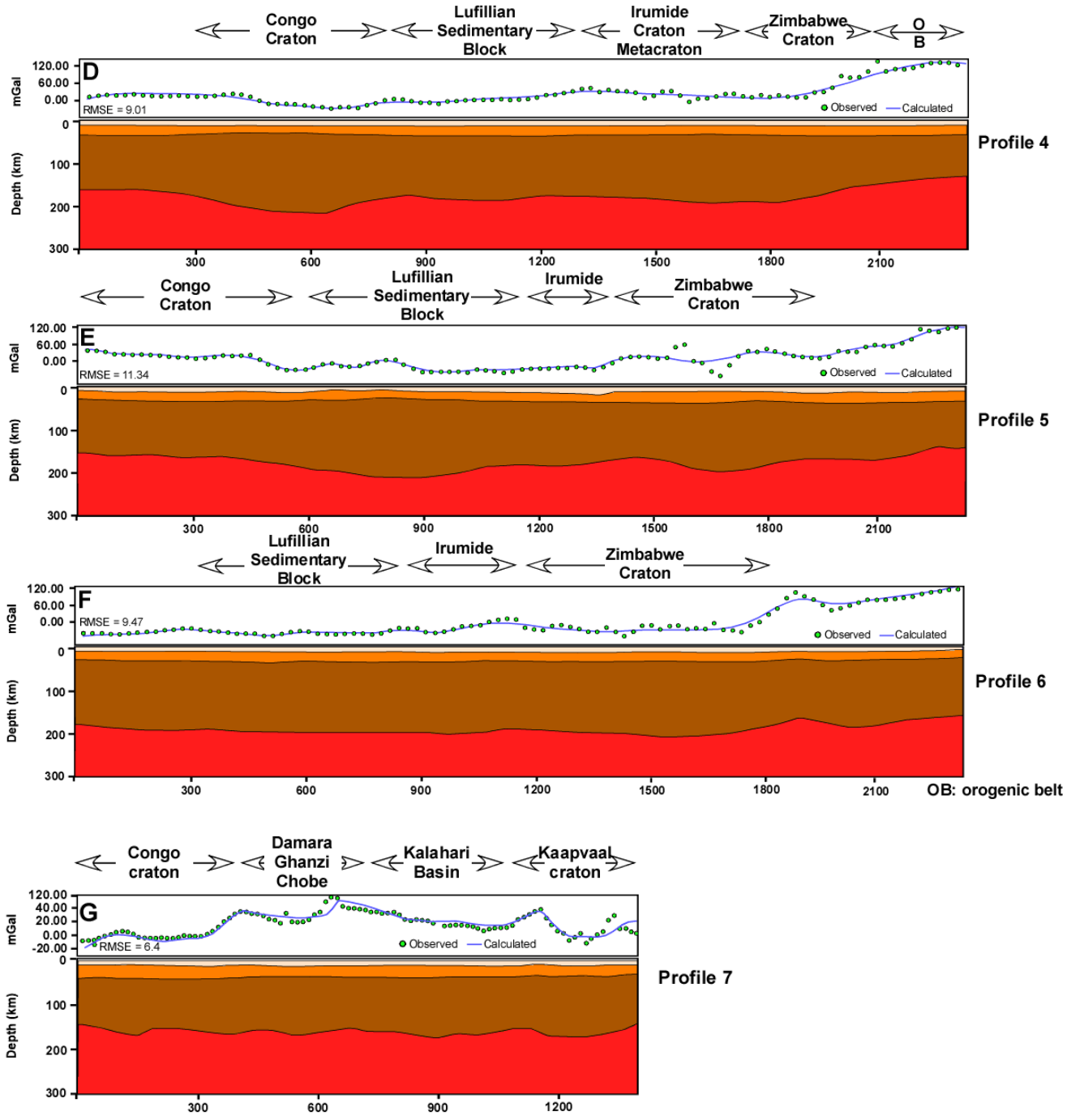

Figure 4.8: 2D forward gravity models constructed from the Bouguer anomaly of the WGM-2012. The profiles mapped changes in lithospheric structure across cratons and orogens. The models are constructed from Figure 4.4 along the back dashed lines. The unit of the RMSE is mGal. The crustal thickness of the 7th profile is constrained by the seismic receiver function study conducted by Yu et al. (2015).

Profile 1 (Fig. 8 A) shows the lithospheric cross section across the Kibaran orogenic belt, the Bangweulu block, and the Irumide metacraton. In this cross section, the depths to the LAB beneath the north eastern portion of the Bangweulu block and the Irumide are anomalously shallow (~ 150 km), whereas the thickness of the lithosphere beneath the Kibaran orogenic belt reaches up to ~ 200 km. The anomalously thin lithosphere beneath the northeastern Bangweulu block is spatially associated with the intra-cratonic Mweru-Wantipa and the Mweru rift which is developed on the margin of the Bangweulu block. Profile 2 (Fig. 8B) shows lithospheric cross section across the northeastward extension of the Congo craton, the Kibaran orogenic belt, the Luffillian arc, the Bangweulu block, the Irumide metacraon, and the Niassa craton. The model shows that the mean lithospheric thickness of these tectonic entities is about 200 km. The only exception is the southern tip of the Bangweulu block whose lithospheric thickness reaches up to ~ 225 km. Like profile 2, profile 3 (Fig. 8C) models the lithospheric cross section across the northeastern edge of the Congo craton, the Kibaran orogenic belt, the Lufillian arc, the Irumide metacraton, the Niassa craton, and a Neoproterozoic orogenic belt that was formed during the closure of the composite Zimbabwe-Kaapvaal-Niassa craton. In this cross section, anomalously thin lithosphere is observed beneath the Irumide Metacraton and the Neoproterozoic orogenic belt with mean lithospheric thickness of 180 km and 150 km, respectively.

Profile 4 (Fig. 8D) transects along the Congo craton, the Lufillian arc, the South Irumide, and the Neoproterozoic orogenic belt. Along this profile, the lithosphere is thicker beneath the Congo craton (with the depth of about 250 km) and the Niassa craton (with the depth of about 230 km), and it is anomalously thin on the southern margin of the Irumide Metacraton. This anomalously thin region is coincidental with the Mwembeshi Shear Zone. Profile 5 (Fig. 8E) and profile 6 (Fig. 8F) imaged lithospheric undulations beneath the Congo craton, Luffilian arc, and the Zimbabwe craton. Results of these 2D gravity forward models showed the presence of thick

lithosphere beneath the southeastern portion of the Congo craton (the highest falling in the range of 230-260 km). Also, along these transects, relatively thinner lithosphere (~ 160 km) is observed beneath the Zimbabwe craton. The depth to asthenosphere beneath the Zimbabwe craton is found to be anomalous shallower than the adjacent neighboring cratons. And finally, the 2D forward gravity model constructed along profile 7 (Fig. 8G), imaged the extreme southeastern portion of the Congo craton, the Damara Neoproterozoic orogenic belt up on which the Okavango rift is developed, and the southwestward extension of the Irumide. The depth to the lithosphere along this transect shows anomalously thin lithosphere beneath the Damara Neoproterozoic orogenic belt (~ 146 km) up on which the Okavango rift rest.

4.5.4 Density inversion results

The Moho topography modeled by the improved 3DINVER.M shows thinner crust (~26 km) beneath the Ubendian Paleoprotorozoic orogenic belt and thicker crust (~35) beneath the Zimbabwe-Kaapvaal-Niassa craton. The thickness of the crust beneath Congo – Tanzania – Bangweulu craton is ~ 30 km. (Figure 9). Overall, the central and southern limit of the study area rests on thicker crust, including the Mesoproterozoic-Neoproterozoic Ghanzi-Chobe and Damara orogens. In the central and northeastern portion of the study area, the topography high of the Moho seem to strike in the NW-SE direction wrapping around the Bangweulu craton outlining, in part, its boundary. Unlike the Bangweulu craton, the NW-SE trending high of the Moho surface does not seem to delineate the spatial extent of the Zimbabwe-Kaapvaal-Niassa craton. However, they represent the deepest Moho interface in the study area.

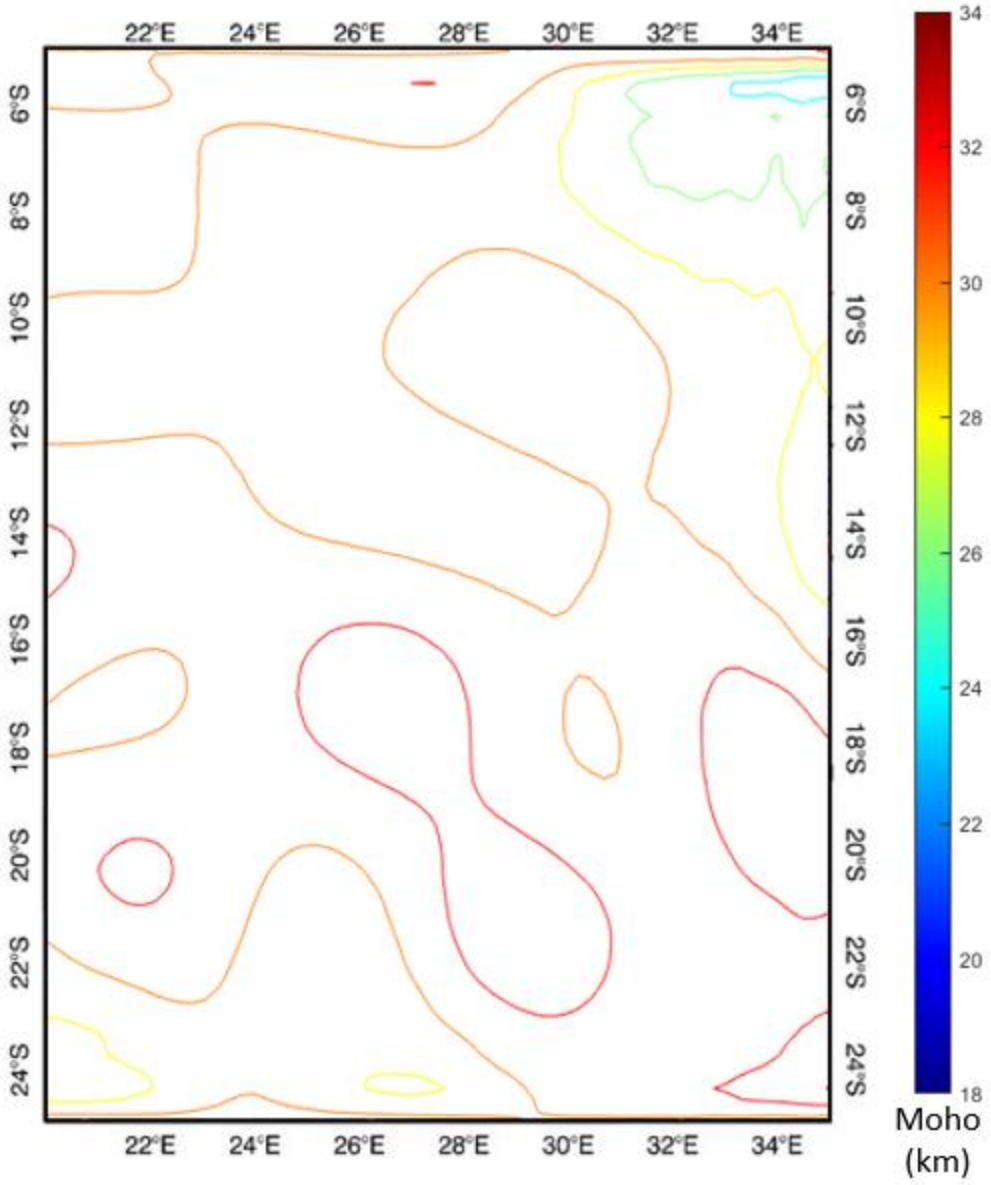

Figure 4.9: Moho map showing crustal thickness variation beneath the Zimbabwe-Kaapvaal-Niassa craton, the Congo – Tanzania – Bangweulu craton, and the Trans-Southern African orogen. The Moho map shows the presence of thicker crust beneath the Zimbabwe-Kaapvaal-Niassa craton (in the central and southeastern limit of the map) and shallower Moho beneath the Ubendian orogenic belt. Seismic Moho results from South African Seismic Experiment (SASE) show an average thickness of 36.2 km beneath the Zimbabwe craton (Kgaswane et al., 2009). The gravity Moho from the same locality is found to be in the range of 34-36 km. Similarly, the seismic Moho results from SASE beneath the Kaapvaal craton is reported to be in the range of 36-39 km. Differently, the gravity Moho map of the figure above estimates the crustal thickness beneath Kaapvaal to be 34 km. The 3D Moho depth inversion results are different from Yu et al. (2015) results across the Okavango Rift. The reason for this could be the initial reference depths assigned for realizations. Further modeling would be performed to identify the cause of inconsistency.

4.6 Discussion

4.6.1 Archean-Paleoproterozoic cratons and Neoproterozoic orogenic belts

With detailed lithospheric imaging, the geographic extents of Archean-Paleoproterozoic cratons and the Mesoproterozoic-Neoproterozoic orogenic belts that are covered by the Karroo sediment are redefined. The findings suggest that the Congo craton whose lithospheric thickness at its cratonic root center reaches up to ~ 256 km, is covered by the Luffilian arc in the southeast. The Bangweulu cratonic block, though fairly thin in the eastern margin (~ 156 km) along the Ubendian orogenic belt, it becomes progressively thick in the southwest of its limit, which partly is covered by the Lufillian. The lithospheric thickness estimation of the Bangweulu cratonic block is consistent with Safarian et al. (2018). The geographic extent of the Niassa craton, which is defined as a craton within the South Irumide (e.g. Safarian et al., 2018), is also redefined in this study. The thick lithosphere (Fig. 7A) bordering the presently defined Niassa craton appears to be contiguous with the Niassa craton, and hence the Niassa craton has a bigger extent than what it is presently defined to be and possibly assumes the geographic extent of the entire South Irumide. Similar to the Archean-Paleoproterozoic cratons, the geographic extents and lithospheric thickness of the Mesoproterozoic-Neoproterozoic orogenic belts are determined. The results show relatively thinner lithosphere beneath the Neoproterozoic Damara and the Mesoproterozoic-Neoproterozoic orogenic belts. The Okavango rift is nucleated on these orogenic belts. The NW-trending systematic thinning of these orogenic belts is interrupted by a thick lithosphere (~ 240 km), which is possibly the northwestward extension of the Zimbabwe craton. The presence of this thick lithosphere could possibly limit the northeastward propagation of the Okavango rift.

The Ubendian orogenic belt, which disappears toward the north below a Mesoproterozoic sedimentary cover (Boniface et al., 2014) also exhibit a thin lithosphere (~ 146 km), sandwiched by the Bangweulu block in the southwest and the Tanzania craton in the northeast.

4.6.2 The Trans-Southern African Orogen and the SWB of the EARS

The LAB map as well as the 2D gravity forward models alongside with previous geophysical lithospheric studies enabled us to establish the regional lithospheric structural relationships between Archean – Paleoproterozoic cratons (the Congo – Tanzania – Bangweulu craton, and the Zimbabwe – Kaapvaal – Niassa craton), Paleoproterozoic – Neoproterozoic orogenic belts and metacratons (Magondi, Kibaran – Irumide – South Irumide, Ghanzi-Chobe, Damara, Zambezi, and Lufilian: here collectively referred to as the Trans-Southern Africa Orogen), and the rift basins of the SWB (Upemba, Mweru – Wantipa, Mweru, Kundelundu, Barotse, Luangwa, Lukusashi-Luano, Kafue, mid Zambezi, Okavango, and Makgadikgadi).

As the results show, except for the Mweru-Wantipa, which is formed on the margin of the mechanically weakened Bangweulu craton with a lithospheric thickness of ~ 150 km, the rest of the SWB are developed within the Paleoproterozoic – Neoproterozoic Trans-Southern Africa Orogen whose lithospheric thickness is mostly in the range of 150 – 200 km. The development of Mweru-Wantipa rift on the margin of the Bangweulu craton is most likely controlled by the presence of mechanically weakened and anomalously thin lithosphere beneath the northeastern limit of the Bangweulu block. With the exception of the northeastern limit of the Bangweulu block and the southern interior of the Zimbabwe craton, which is immediately to the north of the Paleoproterozoic Limpopo belt, the rest of the cratons (Congo – Tanzania – Bangweulu craton in the north and the Zimbabwe – Kaapvaal – Niassa craton) in general have thicker lithosphere (~220 – 258) km and bound the Trans-Southern Africa orogen.

The Bangweulu block is bordered in the northeast by the Paleoproterozoic Ubendian orogenic belt (Fig. 7A and B). The Ubendian orogenic belt hosts the NW-trending Rukwa rift, the NE-trending Usangu rift, and the northern limit of the N-S –trending Malawi rift. The lithospheric thickness of the Ubendian orogenic belt upon which these rifts (Rukwa, Usangu, and part of Malawi) rest is ~ 146 km. Hence, the formations of these basins are regionally influenced by the presence of relatively thin lithosphere beneath the Ubendian orogenic belt.

This regional influence of an orogenic belt on rift formation is not the unique occurrence within the Ubendian orogenic belt; a similar along strike coincidence between SWB basins and the Trans-Southern Africa Orogen is clearly shown in the LAB map; for example : 1) the LAB map seems to suggest that the formations of Luangwa rift, the Lukusashi-Luano rift, and the Kafue rift within the Irumide are influenced by the metacratonization of the Irumide that resulted in a lithospheric thickness of about ~ 160 km; 2) the formation of the Okavango rift (one of the youngest rifts in the world) is formed upon the Neoproterozoic Damara orogenic belt, which has anomalously thin lithosphere of about ~146 km; 3) the Barotse basin north the Okavango rift rests upon anomalously thin lithosphere with a relative thickness of ~ 170 km. These results lead to conclude that the first regional tectonic control, the extent of the SWB as a whole, is influenced by the presence of thinner lithosphere beneath the Paleoproterozoic—Neoproterozoic Trans-Southern Africa Orogen. In addition, the lithosphere beneath cratonic blocks that host some rift basins of the SWB (e.g. Bangweulu cratonic block) is thinner compared to the rest of the craton.

4.6.3 Neoproterozoic – Paleoproterozoic suture zones and the extent of individual SWB basins

Most basins of the SWB of the EARS have not only nucleated upon the Trans-Southern African Orogen, but also preferentially nucleated within preexisting narrow zones of deformations. The LAB maps and the 2D forward gravity models show that the extent of individual rift basins of the SWB is influenced by the presence of discrete lithospheric-scale

Neoproterozoic – Mesoproterozoic suture zones. Examples of basins influenced by Neoproterozoic – Paleoproterozoic suture zones include: 1) the Rukwa and Tanganyika basins, which are influenced by Paleoproterozoic Ubendian shear belt; 2) the Luangwa, Lukusashi-Luano, and Kafue rifts, which are influenced by Neoproterozoic Mwembeshi Shear Zone; 3) the Okavango rift, which is influenced by a Neoproterozoic – Mesoproterozoic deformation zone developed in between the Neoproterozoic Damara orogenic belt and the Mesoproterozoic – Neoproterozoic South Irumide craton.

4.7 Conclusion

Most of the rift basins of the SWB were developed during the Permian – Triassic Karoo rifting event during the early stages of the dispersal of Gondwana, but these were reactivated during the Paleogene – Quaternary rifting event of the EARS. Results showed that the Archean – Paleoproterozoic Congo craton, the Bangweulu cratonic block and the Niassa craton, and the Mesoproterozoic – Neoproterozoic Southern Irumide orogenic belt surrounding the Niassa craton have thick sub-continental lithospheric mantle (SCLM) with lithospheric thickness reaching ~250 km . This suggests that the Niassa craton underlies the entire surface extent of what has been referred to as the "Southern Irumide orogenic belt". No rift basins of the SWB have been observed extending within these cratonic blocks with the exception of the Mweru – Wantipa rift found on the northeastern edge of the Bangweulu cratonic block. Our results also found a relatively thinner (~160 km) and uniform lithosphere beneath the Paleoproterozoic – Mesoproterozoic Kibaran orogenic belt and the Neoproterozoic Lufilian foreland basin, which underlie the Upemba, Kundelungu, and Mweru rift basins of the SWB. This suggests that the Lufilian foreland basin was built on a "Kibaran lithosphere" rather than on a "Bangweulu lithosphere". Further, our results showed that thinner lithosphere (~100 km thick) is present beneath the Mesoproterozoic – Neoproterozoic Irumide metacraton and the Mwembashi shear

zone, which represents the suture zone between the metacraton and the Niassa craton. The presence of thinner lithosphere beneath the Irumide metacraton and the Mwembashi shear zone seems to have significantly controlled the development of the Luangwa rift basin of the SWB.

4.8 References

Abdelsalam, M. G., Liégeois, J. P., & Stern, R. J. (2002). The saharan metacraton. Journal of African Earth Sciences, 34(3-4), 119-136.

Abdelsalam, M. G., Gao, S. S., & Liégeois, J. P. (2011). Upper mantle structure of the Saharan Metacraton. Journal of African Earth Sciences, 60(5), 328-336.

BANKS, H. P., GRIERSON, J. D. & BONAMO, P. M. 1985. The flora of the Catskill clastic wedge. In: WooI)ROW, D. L. & SEVON, W. D. (eds) The Catskill Delta, Geological Society of America, Special Paper, 201, 125-141.

Begg, G. C., Griffin, W. L., Natapov, L. M., O'Reilly, S. Y., Grand, S. P., O'Neill, C. J., ... & Bowden, P. (2009). The lithospheric architecture of Africa: Seismic tomography, mantle petrology, and tectonic evolution. Geosphere, 5(1), 23-50.

Bufford, K. M., Atekwana, E. A., Abdelsalam, M. G., Shemang, E., Atekwana, E. A., Mickus, K., & Molwalefhe, L. (2012). Geometry and faults tectonic activity of the Okavango Rift Zone, Botswana: Evidence from magnetotelluric and electrical resistivity tomography imaging. Journal of African Earth Sciences, 65, 61-71.

Cordani, U. G., Brito-Neves, B. B., & D'Agrella-Filho, M. S. (2003). From Rodinia to Gondwana: a review of the available evidence from South America. *Gondwana Research*, *6*(2), 275-283. Corti, G., J. van Wijk, S. Cloetingh, and C. K. Morley (2007), Tectonic inheritance and continental rift architecture: Numerical and analogue models of the East African Rift system, Tectonics, 26(6), doi:10.1029/2006tc002086.

Crosby, A. G., Fishwick, S., & White, N. (2010). Structure and evolution of the intracratonic Congo Basin. Geochemistry, Geophysics, Geosystems, 11(6).

Daly, M. C., Chorowicz, J., & Fairhead, J. D. (1989). Rift basin evolution in Africa: the influence of reactivated steep basement shear zones. Geological Society, London, Special Publications, 44(1), 309-334.

De Waele, B., Kampunzu, A. B., Mapani, B. S. E., & Tembo, F. (2006). The Mesoproterozoic Irumide belt of Zambia. Journal of African Earth Sciences, 46(1-2), 36-70.

Dewaele, S., Muchez, P., Heijlen, W., Boutwood, A., Lemmon, T., & Tyler, R. (2006). Reconstruction of the hydrothermal history of the Cu–Ag vein-type mineralisation at Dikulushi, Kundelungu foreland, Katanga, DR Congo. Journal of Geochemical Exploration, 89(1-3), 376-379.

Dewaele, S., Muchez, P., Vets, J., Fernandez-Alonzo, M., & Tack, L. (2006). Multiphase origin of the Cu–Co ore deposits in the western part of the Lufilian fold-and-thrust belt, Katanga (Democratic Republic of Congo). Journal of African Earth Sciences, 46(5), 455-469.

Eglington, B. M., & Armstrong, R. A. (2004). The Kaapvaal Craton and adjacent orogens, southern Africa: a geochronological database and overview of the geological development of the craton. *South African Journal of Geology*, *107*(1-2), 13-32.

Emishaw, L., Laó-Dávila, D. A., Abdelsalam, M. G., Atekwana, E. A., & Gao, S. S. (2017). Evolution of the broadly rifted zone in southern Ethiopia through gravitational collapse and extension of dynamic topography. Tectonophysics, 699, 213-226.

Fairhead, J. D., & Girdler, R. W. (1969). How far does the rift system extend through Africa. Nature, 221(5185), 1018.

Fletcher, A. W., Abdelsalam, M. G., Emishaw, L., Atekwana, E. A., Laó-Dávila, D. A., & Ismail, A. (2018). Lithospheric Controls on the Rifting of the Tanzanian Craton at the Eyasi Basin, Eastern Branch of the East African Rift System. Tectonics, 37(9), 2818-2832.

Giacomo, A. M. A. (1984). Petrochemistry, tectonic evolution and metasomatic mineralisations of Mozambique belt granulites from S Malawi and Tete (Mozambique). Precambrian Research, 25(1-3), 161-186.

Goscombe, B., Armstrong, R., & Barton, J. M. (2000). Geology of the Chewore Inliers, Zimbabwe: constraining the Mesoproterozoic to Palaeozoic evolution of the Zambezi Belt. Journal of African Earth Sciences, 30(3), 589-627.

Hanson, R. E., Rioux, M., Bowring, S. A., Gose, G. A., Bartholomew, L. T., Kilian, T. M., ... & Reid, D. L. (2011, October). Constraints on Neoproterozoic intraplate magmatism in the Kalahari craton: geochronology and paleomagnetism of~ 890–795 Ma extension-related igneous rocks in SW Namibia and adjacent parts of South Africa. In *Geological Society of America Abstracts with Programs* (Vol. 5).

Hanson, R. E., Wilson, T. J., & Munyanyiwa, H. (1994). Geologic evolution of the Neoproterozoic Zambezi orogenic belt in Zambia. Journal of African Earth Sciences, 18(2), 135-150.

Hanson, R. E., Wilson, T. J., Brueckner, H. K., Onstott, T. C., Wardlaw, M. S., Johns, C. C., & Hardcastle, K. C. (1988). Reconnaissance geochronology, tectonothermal evolution, and regional significance of the Middle Proterozoic Choma-Kalomo block, southern Zambia. Precambrian Research, 42(1-2), 39-61.

Hargrove, U. S., Hanson, R. E., Martin, M. W., Blenkinsop, T. G., Bowring, S. A., Walker, N., & Munyanyiwa, H. (2003). Tectonic evolution of the Zambezi orogenic belt: geochronological, structural, and petrological constraints from northern Zimbabwe. Precambrian Research, 123(2-4), 159-186.

Huntsman-Mapila, P., Ringrose, S., Mackay, A. W., Downey, W. S., Modisi, M., Coetzee, S. H., & Vanderpost, C. (2006). Use of the geochemical and biological sedimentary record in establishing palaeo-environments and climate change in the Lake Ngami basin, NW Botswana. Quaternary International, 148(1), 51-64.

Johnson, S. P., De Waele, B., & Liyungu, K. A. (2006). U-Pb sensitive high-resolution ion microprobe (SHRIMP) zircon geochronology of granitoid rocks in eastern Zambia: Terrane subdivision of the Mesoproterozoic Southern Irumide Belt. Tectonics, 25(6).

Katumwehe, A. B., M. G. Abdelsalam, and E. A. Atekwana (2015), The role of pre-existing Precambrian structures in rift evolution: The Albertine and Rhino grabens, Uganda, Tectonophysics, 646, 117-129, doi:https://doi.org/10.1016/j.tecto.2015.01.022.

Key, R. M., & Ayres, N. (2000). The 1998 edition of the national geological map of Botswana. Journal of African Earth Sciences, 30(3), 427-451.

Khoza, D., Jones, A. G., Muller, M. R., Evans, R. L., Webb, S. J., & Miensopust, M. (2013). Tectonic model of the Limpopo belt: constraints from magnetotelluric data. Precambrian

Research, 226, 143-156.Kinabo, B. D., Hogan, J. P., Atekwana, E. A., Abdelsalam, M. G., & Modisi, M. P. (2008). Fault growth and propagation during incipient continental rifting: Insights from a combined aeromagnetic and Shuttle Radar Topography Mission digital elevation model investigation of the Okavango Rift Zone, northwest Botswana. Tectonics, 27(3).

Klerkx J., Liegeois .J, Lavreau .J, Clasessens, W (1987). Crustal Evolution of the Northern Kibaran Belt, Eastern and Central Africa, in Proterozic Lithospheric Evolution, edited, pp. 217-233, doi:10.1029/GD017p0217.

Kusky, T. M., Abdel Salam, M. G., Stern, R. J., & Tucker, R. D. (2003). Evolution of the East African and related orogens, and the assembly of Gondwana.

Lenoir, J. L., Liégeois, J. P., Theunissen, K., & Klerkx, J. (1994). The Palaeoproterozoic Ubendian shear belt in Tanzania: geochronology and structure. Journal of African Earth Sciences, 19(3), 169-184.

Leseane, K., Atekwana, E. A., Mickus, K. L., Abdelsalam, M. G., Shemang, E. M., & Atekwana, E. A. (2015). Thermal perturbations beneath the incipient Okavango Rift Zone, northwest Botswana. Journal of Geophysical Research: Solid Earth, 120(2), 1210-1228.

Majaule, T., Hanson, R. E., Key, R. M., Singletary, S. J., Martin, M. W., & Bowring, S. A. (2001). The Magondi Belt in northeast Botswana: regional relations and new geochronological data from the Sua Pan area. Journal of African Earth Sciences, 32(2), 257-267.

Miensopust, M. P., Jones, A. G., Muller, M. R., Garcia, X., & Evans, R. L. (2011). Lithospheric structures and Precambrian terrane boundaries in northeastern Botswana revealed through

magnetotelluric profiling as part of the Southern African Magnetotelluric Experiment. Journal of Geophysical Research: Solid Earth, 116(B2).

Miller, R. M. (1983). The Pan-African Damara Orogen of South West Africa/Namibia. In *Evolution of the Damara Orogen of South West Africa/Namibia*.

Modisi, M. P., Atekwana, E. A., Kampunzu, A. B., & Ngwisanyi, T. H. (2000). Rift kinematics during the incipient stages of continental extension: Evidence from the nascent Okavango rift basin, northwest Botswana. Geology, 28(10), 939-942.

Muller, M. R., Jones, A. G., Evans, R. L., Grütter, H. S., Hatton, C., Garcia, X., ... & Hutchins, D. (2009). Lithospheric structure, evolution and diamond prospectivity of the Rehoboth Terrane and western Kaapvaal Craton, southern Africa: Constraints from broadband magnetotellurics. Lithos, 112, 93-105.

Pisarevsky, S. A., Wingate, M. T., Powell, C. M., Johnson, S., & Evans, D. A. (2003). Models of Rodinia assembly and fragmentation. *Geological Society, London, Special Publications*, *206*(1), 35-55.

Poujol, M., Robb, L. J., Anhaeusser, C. R., & Gericke, B. (2003). A review of the geochronological constraints on the evolution of the Kaapvaal Craton, South Africa. *Precambrian Research*, *127*(1-3), 181-213.

Reeves, C. V. (1972). Rifting in the Kalahari?. *Nature*, *237*(5350), 95.

Ritsema, J., Nyblade, A. A., Owens, T. J., Langston, C. A., & VanDecar, J. C. (1998). Upper mantle seismic velocity structure beneath Tanzania, east Africa: Implications for the stability of

cratonic lithosphere. Journal of Geophysical Research: Solid Earth, 103(B9), 21201-21213.

Sakungo, F. K. (1988). Geothermal resources of Zambia. Geothermics, 17(2), 503-514.

Sarafian, E., Evans, R. L., Abdelsalam, M. G., Atekwana, E., Elsenbeck, J., Jones, A. G., & Chikambwe, E. (2018). Imaging Precambrian lithospheric structure in Zambia using electromagnetic methods. Gondwana Research, 54, 38-49.

Scholz, C.H., Koczynski, T.A. and Hutchins, D.G., 1976. Evidence for incipient rifting in southern Africa. Geophysical Journal International, 44(1), pp.135-144.

Sebagenzi, M. N., & Kaputo, K. (2002). Geophysical evidences of continental break up in the southeast of the Democratic Republic of Congo and Zambia (Central Africa). Stephan Mueller Special Publication Series, 2, 193-206.

Stern, R. J. (1994). Arc assembly and continental collision in the Neoproterozoic East African Orogen: implications for the consolidation of Gondwanaland. *Annual Review of Earth and Planetary Sciences*, *22*(1), 319-351.

Tack, L., Liégeois, J. P., Deblond, A., & Duchesne, J. C. (1994). Kibaran A-type granitoids and mafic rocks generated by two mantle sources in a late orogenic setting (Burundi). Precambrian research, 68(3-4), 323-356.

Talwani, M., Worzel, J. L., & Landisman, M. (1959). Rapid gravity computations for two-dimensional bodies with application to the Mendocino submarine fracture zone. Journal of geophysical research, 64(1), 49-59.

Thomas, R. J., Agenbacht, A. L. D., Cornell, D. H., & Moore, J. M. (1994). The Kibaran of southern Africa: tectonic evolution and metallogeny. Ore Geology Reviews, 9(2), 131-160.

Treloar, P. J. (1988), The geological evolution of the Magondi Mobile Belt, Zimbabwe, Precambrian Research, 38(1), 55-73, doi:https://doi.org/10.1016/0301-9268(88)90093-9.

TSELENTIS, G. A., DRAKOPOULOS, J., & DIMITRIADIS, K. (1988). A spectral approach to Moho depths estimation from gravity measurements in Epirus (NW Greece). Journal of Physics of the Earth, 36(6), 255-266.

Unrug, R. (1983). The Lufilian Arc: a microplate in the Pan-African collision zone of the Congo and the Kalahari cratons. *Precambrian Research*, *21*(3-4), 181-196.

Van Reenen, D. D. (Ed.). (2011). *Origin and evolution of Precambrian high-grade Gneiss terranes, with special emphasis on the Limpopo Complex of Southern Africa* (Vol. 207). Geological Society of America.

Weeraratne, D. S., D. W. Forsyth, K. M. Fischer, and A. A. Nyblade (2003), Evidence for an upper mantle plume beneath the Tanzanian craton from Rayleigh wave tomography, Journal of Geophysical Research: Solid Earth, 108(B9), doi:10.1029/2002jb002273.

Won, I. J., & Bevis, M. (1987). Computing the gravitational and magnetic anomalies due to a polygon: Algorithms and Fortran subroutines. Geophysics, 52(2), 232-238.

Yu, Y., Liu, K. H., Huang, Z., Zhao, D., Reed, C. A., Moidaki, M., & Gao, S. S. (2017). Mantle structure beneath the incipient Okavango rift zone in southern Africa. Geosphere, 13(1), 102-111.

Yu, Y., Liu, K. H., Reed, C. A., Moidaki, M., Mickus, K., Atekwana, E. A., & Gao, S. S. (2015). A joint receiver function and gravity study of crustal structure beneath the incipient Okavango Rift, Botswana. Geophysical Research Letters, 42(20), 8398-8405.

Yu, Y., Liu, K. H., Moidaki, M., Reed, C. A., & Gao, S. S. (2015). No thermal anomalies in the mantle transition zone beneath an incipient continental rift: Evidence from the first receiver function study across the Okavango Rift Zone, Botswana. Geophysical Journal International, 202(2), 1407-1418.

Zientek, M. L., Bliss, J. D., Broughton, D. W., Christie, M., Denning, P. D., Hayes, T. S., ... & Master, S. (2014). Sediment-hosted stratabound copper assessment of the Neoproterozoic Roan Group, central African copper belt, Katanga Basin, Democratic Republic of the Congo and Zambia: Chapter T in Global mineral resource assessment (No. 2010-5090-T). US Geological Survey.

CHAPTER V

CONCLUSION

V.I The Turkana Depression

The Turkana depression is a NW-trending narrow topographic corridor between the Ethiopia – Yemen plateau in the northeast and the East Africa plateau to the southwest and it appears to suppress the surface expression of the East African Rift System (EARS). It extends in northern Kenya, southern Ethiopia and eastern South Sudan between the southern Main Ethiopian Rift in the northeast and the Kenya rift to the southwest. The depression is dominated by outcrops of Precambrian crystalline basement rocks, Mesozoic and Cenozoic rift-related sediment, and Cenozoic volcanic rocks of the EARS. The Mesozoic Anza rift extends within the Turkana depression and it representes a NW-trending failed arm of the Lamu paleo triple junction. The other two rifts of the triple junction resulted in the separation of Madagascar from the African continent. Geophysical studies suggest that the Anza rift is connected to the Mesozoic Sudan – South Sudan rifts, especially the Muglad – Jonglei – Mongala rift. The Anza rift is intersected at high angle by the N- and NE-trending rift segments of the EARS represented by the Turkana rift and the Kino - Sogo rift. In this work, I imaged the crustal thickness beneath the Turkana depression using two-dimensional (2D) inversion of the Bouguer gravity anomalies of the European Improved Gravity Model of the Earth by New Techniques (EIGEN – 6C4) as well as 2D forward gravity modeling of these Bouguer gravity anomalies. In addition, I modeled in three-dimension (3D) the upper crustal density distribution of the Kino - Sogo rift through the inversion of the residual

gravity data obtained from the EIGEN – 6C4. Our results show thinner crust ranging between 24 and 28 km beneath the Turkana depression along the Anza rift and the Sudan – South Sudan rifts as well as localized crustal thinning beneath the Turkana rift. This observation is consistent with results from the 3D upper crustal density model which shows broad NW-trending density anomalies between 5 and 10 km depth beneath the Anza rift and narrow NE-trending density anomalies associated with the Kino Sogo rift between 0 m and 5 km depth. The findings suggest that the dominant crustal structure of the Turkana depression is associated with the Mesozoic Anza rift and the Sudan - South Sudan rifts whereas the Cenozoic EARS is expressed only at shallower upper crustal level.

V.II The Trans-Southern African Orogen

Using two-dimensional (2D) radially-averaged power spectral analysis and 2D forward gravity modeling of satellite gravity data, I imaged the lithospheric structure (the depth to the upper crust, the depth to Moho, and the depth to the asthenosphere – lithosphere boundary) beneath the Congo – Tanzania – Bangweulu craton, the Zimbabwe – Kappvaal – Niassa craton, and the Trans-Southern African orogen. The latter underlies most of the basins of the Southwestern Branch (SWB) of the East African Rift System (EARS). I find the cratons, in general, to be underlain by thicker lithosphere reaching ~250 km compared to the Trans-Southern African orogen, which is underlain by lithosphere that is 150 – 200 km thick. Our findings suggest that the spatial extent of the Congo craton is much wider than what is exposed on the surface and is covered in the southeast by the Luffilian arc. Similarly, the geographic extent of the Bangweulu craton is wider than what is exposed on the surface with its southwestern limit covered by the Luffilian arc. The geographic extent of the Niassa craton is also redefined, and which is shown to have relatively thinner lithosphere (~ 200 km). In addition, the depths to LAB of Mesoproterozoic – Neoproterozoic orogenic belts, which are covered by the Karoo sediment are determined. The notable examples may be the lithospheric thickness of the Mesoproterozoic – Neoproterozoic Ghanzi – Chobe orogenic belt (~ 146 km) and the Neoproterozoic Damara orogenic belt (~ 146 km). The LAB estimates of these tectonic entities suggest that the SWB of the EARS as a whole are regionally controlled by the

Trans-Southern Africa orogeny, while the development of individual basins is controlled by localized preexisting weaknesses. One notable example is the development of the Luangwa rift along the Mwembeshi shear zone, which is developed within a relatively thinner lithosphere that is in the range of (~ 150 – 200) km

VITA

Luelseged Mengesha Emishaw

Candidate for the Degree of

Doctor of Philosophy

Dissertation: ON CRUSTAL AND LITHOSPHERIC STRUCTURES OF RIFT BASINS FORMED WITHIN THE TURKANA DEPRESSION IN THE EAST AFRICA AND THE TRANS-SOUTHERN AFRICAN OROGEN IN THE SOUTHWEST AFRICA

Major Field: Geology

Biographical:

Education:

Completed the requirements for the Doctor of Philosophy in Geology at Oklahoma State University, Stillwater, Oklahoma in December, 2020.

Completed the requirements for the Master of Science in Geology at Oklahoma State University, Stillwater, Oklahoma in 2015.

Completed the requirements for the Bachelor of Science in Geology at Addis Ababa University, Ethiopia in 2012.

Professional Memberships:
Geological Society of America; Society of Exploration Geophysics